KENS REPORT XIX

2012

High Energy Accelerator Research Organization
KENS

KEK Progress Report 2013-7 M

© High Energy Accelerator Research Organization (KEK), 2014

KEK Reports are available from:

High Energy Accelerator Research Organization (KEK)
1-1 Oho, Tsukuba-shi
Ibaraki-ken, 305-0801
JAPAN

Phone: +81-29-864-5137
Fax: +81-29-864-4604
E-mail: irdpub@mail.kek.jp
Internet: http://www.kek.jp

KENS REPORT XIX

2012

PREFACE

At the KEK Neutron Science Laboratory (KENS), the world's first user-oriented pulsed spallation neutron source was constructed in 1980. It was dedicated to inter-university programs and the power of the proton accelerator was 3 kW. The pulsed neutron facility at KENS was shut down in March 2006 for the construction of a 1 MW pulsed neutron source at the Materials and Life Science Experimental Facility (MLF) of Japan Proton Accelerator Research Complex (J-PARC) cooperated with Japan Atomic Energy Agency (JAEA). The neutron source of MLF has started its user-program since 2008 and KENS operates beam lines for the inter-university programs.

In FY2012, 10 special (S-type) proposals were approved as part of the Inter-University Research Program on pulsed neutron science. Three of S-type proposal were in the status of beam line construction: (1) the construction of a resonance-type neutron spin-echo instrument (BL06 VIN-ROSE) has advanced, (2) the commissioning of a powder diffractometer for the development of the next generation batteries (SPICA, BL09), which was funded as part of the NEDO project, has been steadily progressing, (3) a supplemental budget for the polarization chopper spectrometer (POLANO, BL23) was approved by Tohoku University and KEK at the end of FY2012 and a full scale construction has started. Besides the S-type proposal, 80 general proposals were approved with 5 instruments (BL05 NOP, BL08 SuperHRPD, BL12 HRC and BL21 NOVA).

This report was made to show activities of S-type proposals. We are pleased to hear any of comments about the activities.

Head of KENS and Editor of KENS-Report XIX

Toshiya Otomo

CONTENTS

FACILTY REPORT

S-TYPE PROJECT REPORT

KENS REPORT XIX 2012

FACILITY REPORT

Neutron Science Laboratory

T.Otomo

Head of Neutron Science Division (KENS), Institute of Materials Structure Science
High Energy Accelerator Research Organization

1. From KENS Facility

Inter-University Research Program

In FY2012, 10 special (S-type) proposals, listed in table 1, and 80 general proposals were approved as part of the Inter-University Research Program on pulsed neutron science.

Table 1: S-type projects at KENS.

Proposal ID	Principal Investigator	BL No.
Title of proposal		
2012S01	S. Itoh (KEK) & Masuda (Tokyo Univ.)	BL12
Studies on Dynamics in Condensed Matters by using the High Resolution Chopper Spectrometer		
2009S03	H. Shimizu (Nagoya Univ.)	BL05
Fundamental Physics with Pulsed Cold Neutrons		
2009S04	M. Furusaka (Hokkaido Univ.)	
Technical feasibility study of mini-focusing small-angle neutron scattering instrument		
2009S05	Y. Noda (Tohoku Univ.)	BL08
Structural study of functional materials and development of advanced methodology using SuperHRPD		
2009S06	T. Otomo (KEK)	BL21
Fundamental research of hydrogen storage mechanism with high-intensity total diffractometer		
2009S07	M. Hino (Kyoto Univ.)	BL06
Construction of advance neutron beam line for VIllage of Neutron Spin Echo spectrometers (VIN ROSE)		
2009S08	J. Takahara (Kyushu Univ.)	BL16
Analysis of Dynamics at Nano Interface of Functional Soft Matter Principal		
2009S09	K. Ohoyama (Tohoku Univ.)	BL23
Dynamic and Static Structural Analysis by 3D polarimetry spectroscopy on Neutron Analysis System for Functional Material		
2009S10	T. Fukunaga (Kyoto Univ.)	BL09
Structural study of batteries by using the special environment neutron powder diffractometer		
2009S11	Y. Kiyanagi (Hokkaido Univ.)	
Neutron Transmission Imaging		

General proposals to use the KENS beam lines were discussed by the J-PARC/MLF Neutron Science Program Advisory Committee, and the scientific merits of these proposals were assessed. They were then approved by the Neutron Science Program Advisory Committee (KENS-PAC) of IMSS.

The S-type proposals, aimed at scientific investigations as well as at the construction, development, and maintenance of neutron related instruments, were evaluated by the KENS-PAC at IMSS, following which they approved the beam time and funding. The 6 approved S-type research projects were based on existing neutron science instruments: the Super High Resolution Powder Diffractometer (SuperHRPD, BL08), the High Intensity Total Scattering Diffractometer (NOVA, BL21), the High Resolution Chopper Spectrometer (HRC, BL12), the High Performance Neutron Reflectometer with a Horizontal Sample Geometry (SOFIA, BL16), the Neutron Optics and Physics (NOP, BL05), and the powder diffractometer for the development of next generation batteries (SPICA, BL09) funded as the part of the NEDO project. The commissioning of SPICA has been steadily progressing. For two other S-type projects, the construction of the resonance-type neutron spin echo spectrometers (VIN-ROSE, BL06) and the construction of the polarization chopper spec-

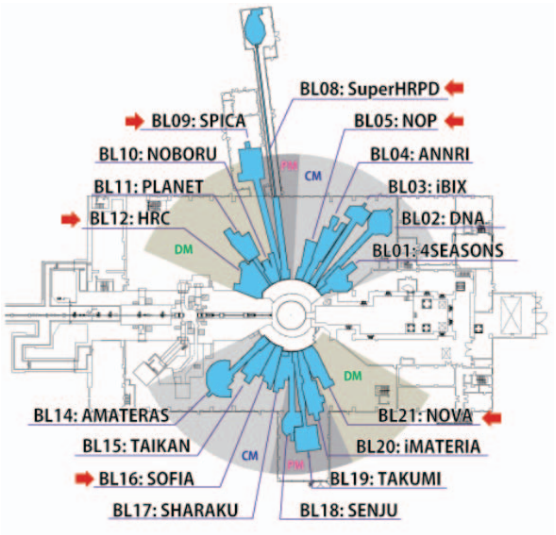

Fig. 1: Neutron beam lines of Materials and Life Science Experimental Facility (MLF). Red arrows indicate the operating/commissioning beam line of KEK.

trometer (POLANO, BL23) have steadily progressed. A supplemental budget was approved by Tohoku University and KEK at the end of FY2012.

2. Schools for beginners in 2012

KEK summer challenge 2012 was held for the first time at J-PARC. The main part of this event was held in August at the KEK Tsukuba campus. Five undergraduate students were given the opportunity to explore the high-resolution powder diffraction measurements at SuperHRPD.

Fig. 2: KEK summer challenge 2012 at SuperHRPD.

The MLF school of neutron and muon was held by the J-PARC center, CROSS-Tokai and Ibaraki Prefecture, from Dec 18–21 at MLF. Twenty four university students and researchers from universities as well as industries attended this event. The attendees participated in neutron experiments and the analyzed "results" were reported during the presentation session. As a KEK beam line facility, SuperHRPD (BL08) welcomed the students.

3. J-PARC Operation

Intense Pulsed Neutron Source

In FY2012, the MLF neutron source was operated for about 187 days with very high reliability, 93.8%. In January 2012, the proton power reached 300 kW. Shock wave mitigation using a He-gas bubbling system worked well under the high proton power and it was confirmed that the micro-bubble system efficiently reduced shock waves in the mercury target bombered with proton beams. Eighteen beam lines are operational and 3 beam lines are under construction (BL06, BL22 and BL23).

Super High Resolution Powder Diffractometer (SuperHRPD)

The Great East Japan earthquake caused damage to the SuperHRPD, and temporary restoration was completed by the end of March 2012; voids discovered under the buildings were filled with concrete, and the 83 m supermirror guide tubes, supporting rails, and pedestals were all removed, repaired, and re-installed. Intensity spectra at the exit of the guide tube measured after the quake almost agreed completely with those measured before the earthquake. The commissioning was successful and the diffraction data of the standard samples were successfully analyzed using Z-Rietveld. The disc chopper material Gd_2O_3 was replaced with $^{10}B_4C$, resulting in the reduction of background for the 5 Hz mode. The general user program restarted in 2012.

Special Environment Powder Diffractometer (SPICA)

The construction of SPICA (BL09), a special environment powder diffractometer, has been promoted for the basic research on batteries, and the commissioning of SPICA started in Oct., 2012. The completion ceremony for SPICA was held on Sep. 4 with over 150 attendees (Fig. 3). Deputy Director-Generals from both MEXT (Ministry of Education, Culture, Sports, Science and Technology) and METI (Ministry of Economy, Trade and Industry) attended the ceremony.

The powder diffraction patterns at backward bank were time-focused, and the obtained resolution in d spacing reached a value as low as $\Delta d/d = 0.08\%$. The diffraction patterns at backward, high angle, 90 degree, and low angle banks of several standard samples were successfully analyzed through the Rietveld method.

Fig. 3: The completion ceremony for SPICA: press release, ribbon cutting ceremony, lectures, and party.

High Resolution Chopper Spectrometer (HRC)

The High Resolution Chopper Spectrometer (HRC) is being operated at BL12 in MLF, J-PARC, to study condensed matter dynamics with high-resolutions using

relatively high-energy neutrons.

A collimator system is installed just upstream of the sample in order to reduce background noise. The divergence of the incident neutron beams is controlled by the collimator, which composed of slits of vertical cadmium sheets. The collimators having collimations of 0.3° and 1.5° are mounted on the collimator system. One of the two can be selected using an elevation mechanism with a motor control. On the HRC, position sensitive detectors (PSD) are mounted at scattering angles (ϕ) ranging from 3° to 42° for conventional inelastic neutron scattering experiments. The background noise for these experiments is successfully reduced by using the 1.5° collimator, as reported previously. Furthermore, on the HRC, PSDs are mounted at low angles down to $\phi = 0.5°$; the 0.3° collimator can reduce the background in this low angle part.

Using the HRC, neutron Brillouin scattering (NBS) experiments have become feasible by reducing the background noise at low scattering angles down to 0.5°. NBS is inelastic neutron scattering in the forward direction. Although the principle is not new, NBS has recently been developed in some spectrometers around the world by improving neutron flux at the high energy region. NBS is the most promising way to observe excitations in the forward direction from powders, polycrystals, or liquids. A suitable example of the use of this method is the observation of spin waves propagating from (000). Owing to the kinematic constraints of neutron spectroscopy, incident neutron energy (E_i) in the sub-eV region is required for measuring scattering in the meV transferred energy (E) range with a high energy resolution $\Delta E/E_i$. Furthermore, the scattered neutrons need to be detected at very low scattering angles (ϕ), in order to determine the dispersion relation of the spin waves. Low angle detectors are essential to access the present energy–momentum space. In fact, the region above the dashed line in Fig. 4, which is the envelope of scan loci for $\phi = 5°$ with respect to E_i, can never be accessed using a conventional spectrometer with the lowest scattering angle of $\phi = 5°$, for instance. Therefore, these measurements cannot be performed on standard direct geometry chopper spectrometers.

First, the NBS experiment was performed using the HRC to observe spin waves in a polycrystalline sample of ferromagnetic perovskite, $La_{0.8}Sr_{0.2}MnO_3$, having a cubic structure with a tiny distortion (Curie temperature: $T_C = 316$ K). Magnetic properties of this material are well elucidated and the measurement of spin waves using a single crystal sample has already been reported. Figure 4 shows the dispersion relation of spin waves in $La_{0.8}Sr_{0.2}MnO_3$ measured at $E_i = 100$ meV using the HRC, with an energy resolution $\Delta E/E_i = 2\%$. The observed dispersion relations at T = 6 and 245 K were well fitted to the functional form with $E = DQ^2$, where Q is the scattering vector. The D values were obtained to be 130 ± 13 and 88 ± 2 meVÅ^2 at T = 6 and 245 K, respectively. These values are in good agreement with the results (D = 131 and 89 meVÅ^2 at T = 14 and 250 K, respectively) obtained in the previous inelastic neutron scattering experiments using a single crystal. The feasibility of NBS experiments using the HRC was demonstrated by this experiment.

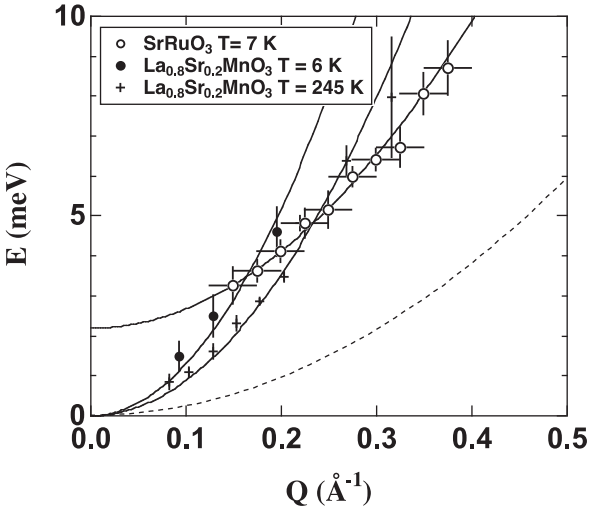

Fig. 4: Spin-wave dispersion curves for $La_{0.8}Sr_{0.2}MnO_3$ and $SrRuO_3$ determined using the HRC. The solid lines are fitted curves. The dashed line is the upper limit accessible using a spectrometer having the lowest scattering angle of $\phi = 5°$.

Similarly, spin waves in a polycrystalline ferromagnet, $SrRuO_3$ ($T_C = 165$ K), were then measured using the HRC. This material also has a cubic perovskite structure with a tiny distortion, but a large single crystal suitable for inelastic neutron scattering experiments has not yet been synthesized. The measurement was performed at T = 7 K and $E_i = 100$ meV, and well-defined spin wave peaks were observed. As shown in Fig. 4, the dispersion relation of spin waves in $SrRuO_3$ was well fitted to $E = E_0 + DQ^2$ with an energy gap E_0 and a stiffness constant D. The dispersion relation of $SrRuO_3$ shows an apparent energy gap. This characteristic feature might have originated from an induced spin anisotropy, which has been a long-standing issue, possibly from a spin-orbit coupling acting on the Ru 4d orbital. The anomalous Hall effect in $SrRuO_3$ was theoretically interpreted as a strong spin-orbit interaction. This interpretation also predicted a magnetic monopole scenario, which can potentially be proven by future neutron scattering experiments.

Soft Interface Analyzer (SOFIA)

Neutron reflectometry is one of the most powerful tools for investigating the surface and interfacial structures of materials in the spatial range of nano meters to sub-microns. The SOFIA is a horizontal-type neutron reflectometer at BL16, J-PARC/MLF, constructed in

collaboration with JST/ERATO. Two downward neutron beam lines of 2.2 and 5.7 degrees are introduced to investigate an air-liquid interface. In order to scan a wider incident angle, super mirrors are installed before the sample to change the beam path.

From this year onwards, the regulation to treat a liquid sample is drastically relaxed and the air-liquid interface measurement is now available. For this measurement, a Langmuir trough is newly installed to prepare a monolayer on a free water surface (Fig. 5). The result of the test measurement shows a clear fringe originating from a partially deuterated stearic acid monolayer (Fig. 6). Due to the high flux neutron beam of J-PARC/MLF, 30 minutes is enough to obtain data with good statistics; this duration is 10 times less than that of KEK-PS. The background noise level, however, is still higher than expected because of the scattering from the trough. A neutron absorber has been developed to suppress the background. Additionally, a sample chamber to control temperature and humidity and a new detector to accept a higher neutron flux at 1 MW operation are being tested. These developments are almost complete and are scheduled to be installed in the near future.

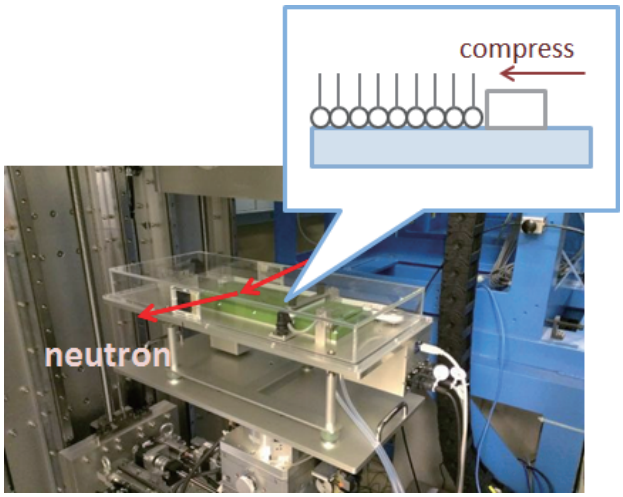

Fig. 5: Langmuir trough to prepare a monolayer on a free water surface for neutron reflectivity measurement.

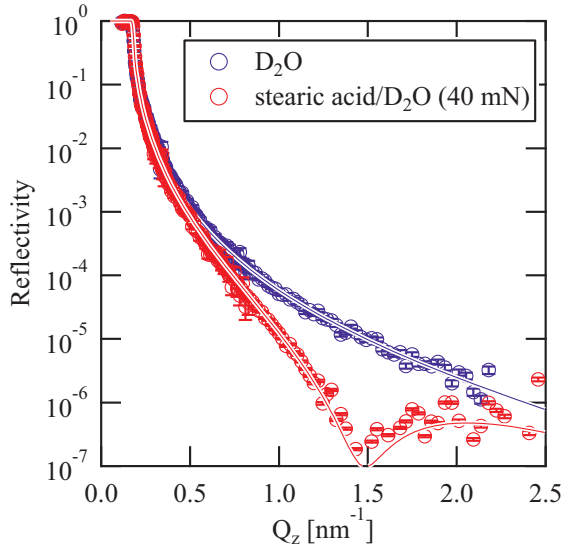

Fig. 6: Neutron reflectivity profiles from air/heavy water interface and from air/stearic acid/heavy water interface obtained using the SOFIA reflectometer.

Neutron Optics and Physics (NOP)

A precise neutron lifetime measurement is underway at the NOP beam line. The neutron lifetime is measured by tagging the electrons from the neutron decays in flight. A time projection chamber (TPC) detects the decay electrons with an efficiency of more than 99.9%. The neutron flux, the electron tagging efficiency, and background events are critical parameters for accurately determining the neutron lifetime. The neutron flux is measured by identifying the ^{3}He(n,p)^{3}H events using the TPC, and a very small portion of the ^{3}He gas is mixed. However, these ^{3}He(n,p)^{3}H reactions can also be misidentified as decay electrons since the energy depositions due to the two processes overlap as shown in Fig. 7. Another background source is ^{12}C in CO_2, which is mixed as quench gas in the TPC. The energy depositions due to ^{12}C(n, γ)^{13}C reactions also slightly overlap with those due to decay electrons (Fig. 7). Additional background events, which are due to N_2 contamination in the TPC, have been observed in data from the ^{14}N(n,p)^{14}C reactions. Figure 8 shows the energy depositions due to the ^{14}N(n,p)^{14}C reactions together with those due to the ^{3}He(n,p)^{3}H reactions. Many of these background events can be identified using the event topology and will be distinguished from the signal events. The data acquisition system and procedure are being improved, and an efficient off-line data analysis method is being studied to minimize the systematic uncertainties in the neutron lifetime measurement.

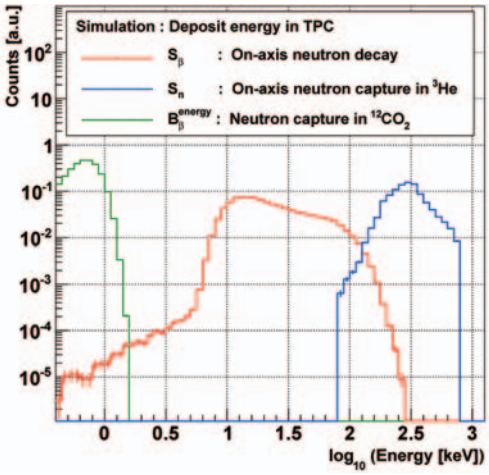

Fig. 7: Energy depositions due to the neutron decay electrons, ^{3}He(n,p)^{3}H reactions, and ^{12}C(n, γ)^{13}C reactions.

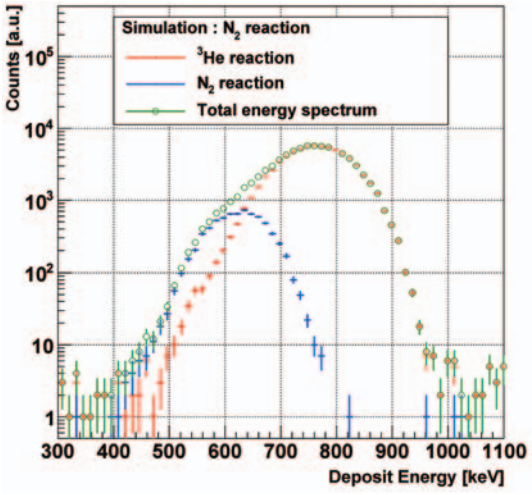

Fig. 8: Energy depositions due to the ^{3}He(n,p)^{3}H and ^{14}N(n,p)^{14}C reactions.

The High Intensity Total Diffractometer (NOVA)

NOVA is a total diffractometer used for investigating non-crystalline structures and also one of the most intense powder diffractometers with reasonable resolutions ($\Delta Q/Q \approx 0.6\%$ for 90° detectors).

To maximize the benefit of neutron usage for investigation of hydrogen in materials, a Fermi chopper system, which is same as that of the HRC, was developed by KEK and installed on NOVA. The chopper is on the off-beam position for normal total scattering measurements and moves to the on-beam position for inelastic measurements (Fig. 9). Since MLF adopted the event-recording data acquisition system, no conditional change of DAQ is required to perform inelastic measurement using NOVA. In other words, the in-situ condition of the sample can be exactly the same in diffraction and inelastic measurements. Figure 10 shows the dynamical structure factor of TiH_2 measured using NOVA. The elastic intensity becomes weak at a high-Q range because of recoil effect. Harmonic excitations, up to the 4th excitation, were observed clearly.

Activities of NOVA were partially supported by The New Energy and Industrial Technology Development Organization (NEDO), for the "Feasibility Study on Advanced Hydrogen Storage Materials for Automotive Applications (2012)."

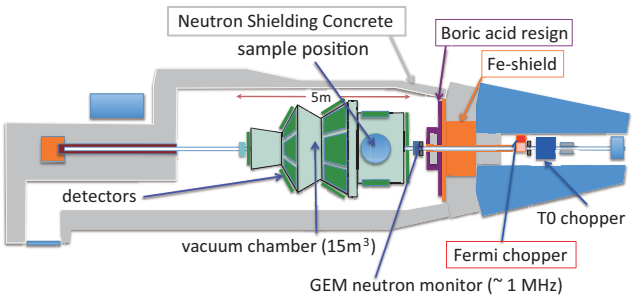

Fig. 9: Alignments of choppers on NOVA.

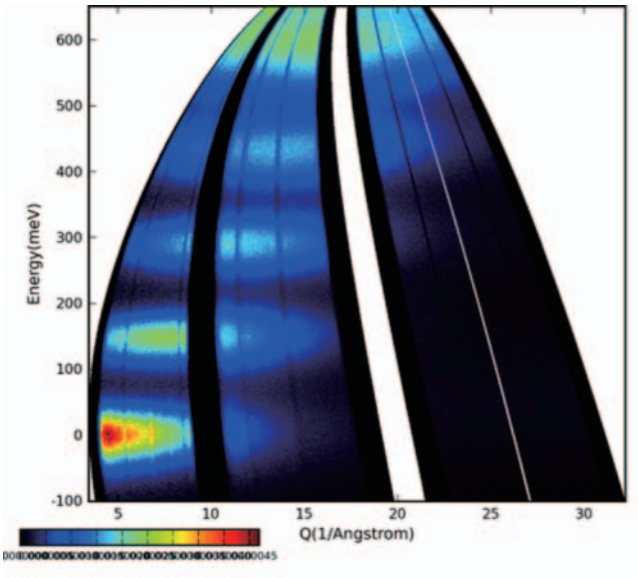

Fig. 10: Dynamical structure factor of TiH_2 measured using NOVA.

4. Device R&D

Detector and DAQ Electronics

The SOFIA system at MLF/J-PARC assembly incorporates 21 MPSD boards stacked at intervals of 5 mm with a total detection area of 105 mm (horizontal) × 128 mm (vertical). The system requires a high positional resolution in the vertical direction and a high overall count rate.

The overall system consists of the 21 stacked detectors, a support board, and 3 NEUNET modules. The support board, which supplies the adjusted voltages, is controlled using a PC through a network. Figure 11 shows the photo of the system setup, along with a 2D image result. The boards are stacked along the horizontal axis in this 2D image while varying the shading along the vertical axis on the basis of the neutron

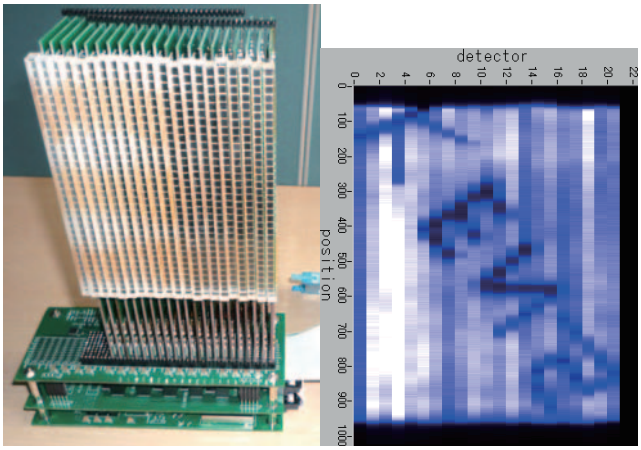

Fig. 11: MPSD system setup; 2D image result.

count. This figure also shows the positional resolution of the MPSD boards; here, the word "KENS" is formed by the pattern of cadmium masks. At SOFIA, this system obtained a maximum counting rate of 250 kilo counts per second (kcps) from a 50 mm wide horizontal neutron beam.

In order to obtain clearer images, the diffusion glass sections covering each 1D MPSD are replaced with a single glass plate, resulting in the 2D MPSD system shown in the block diagram in Fig. 12. Using crosstalk between the 1D MPSDs, this system is able to calculate the position of a captured neutron.

The image generated with this 2D MPSD can be rendered at a horizontal resolution of either 2.5 or 1.25 mm, representing two or four times improvement, respectively, compared with the 5 mm resolution of the original SOFIA assembly. Under any of the above conditions, the vertical resolution is about 1 mm. Figure 13 shows 2D images at these two improved resolutions. As the pixel pattern at 2.5 mm resolution is symmetrical with respect to the MPPC structure, it does not generate distortion. On the other hand, even though the resolution at 1.25 mm is better, the image pixels will be split at an edge or at the center of an MPPC, creating vertical stripes along the array of 1D MPSDs and thereby necessitating additional compensation.

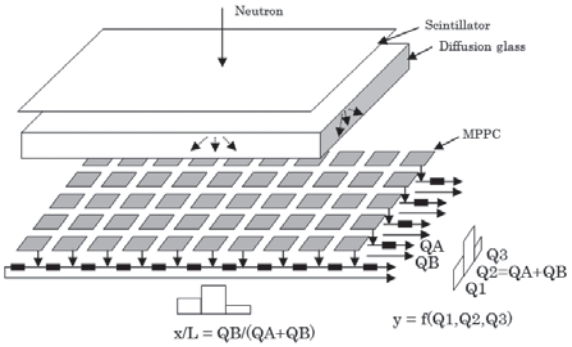

Fig. 12: Block diagram of the 2D MPSD.

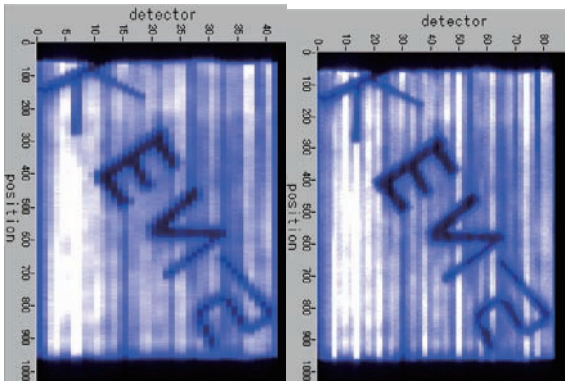

Fig. 13: Resolutions in the horizontal direction: 2.5 mm (left) and 1.25 mm (right).

KENS REPORT XIX 2012

S-TYPE PROJECT REPORT

High Resolution Chopper Spectrometer HRC at BL 12

S.Itoh[1], T.Yokoo[1], T.Masuda[2], H.Yoshizawa[2], D.Kawana[3*], M.Soda[2], Y.Ikeda[2], T.J.Sato[4], Y.Nambu[4], K.Kuwahara[5], M.Hase[6], H.Hiraka[3], K.Yoshida[7], K.Ono[3], and Y.Endoh[1]

[1]*Neutron Science Division, Institute of Materials Structure Science, High Energy Accelerator Research Organization, Tsukuba 305-0801*
[2]*Neutron Science Laboratory, The Institute for Solid State Physics, The University of Tokyo, Tokai 319-1106*
[3]*Condensed Matter Research Center, Institute of Materials Structure Science, High Energy Accelerator Research Organization, Tsukuba 305-0801*
[4]*Institute of Multidisciplinary Research for Advanced Materials, Tohoku University, Sendai 980-8577*
[5]*Institute of Applied Beam Science, Ibaraki University, Mito 310-8512*
[6]*National Institute for Materials Science, Tsukuba 305-0047*
[7]*Department of Chemistry, Fukuoka University, Fukuoka 814-0180*

1. Overview

The High Resolution Chopper Spectrometer (HRC) is being operated at BL12 in MLF, J-PARC, to study the dynamics in condensed matters with high-resolution and relatively high-energy neutrons. We report here the activity of the S-type project on the basis of the HRC in FY2012 (2012S01). This project aims to establish a comprehensive picture of the condensed matter physics by observing a wide range of electron correlated systems using the HRC. We selected -some of the researched topics and focused on the following four points of view: novel ground states in low dimensional quantum spin systems; interactions among spin, charge, orbital and lattice in electron systems with strong or medium electroncorrelations; origin of magnetism in ferromagnetic metals; magnetism related to characteristic structures in strongly correlated electron systems. We performed experiments concerning these subjects, as described below.

For this purpose, the HRC was improved. In particular, the neutron Brillouin scattering (NBS) experiments on the HRC became feasible by the improvement of the collimation of the incident neutron beam [1]. The NBS is the inelastic neutron scattering in the forward direction, and therefore, this is effective to observe ferromagnetic spin waves from polycrystalline samples. The development of the NBS method on the HRC is described in a separate section in this report.

The element strategy project conducted by the MEXT started in 2012 and the IMSS became one of its key institutes. The aim of this project is to develop functional materials without rare elements. Preliminary experiments on a strong permanent magnet $Nd_2Fe_{14}B$ as a magnetic material and an Fe-based superconductor as an electronic material were performed on the HRC, as a project of the IMSS.

The HRC has accepted experiments for general use since 2011B. In FY2012, five general use experiments were performed: successive metalnonmetal transitions with totally-symmetric electron ordering in $(Pr_{1-x}Ce_x)Ru_4P_{12}$ (part I) by K. Iwasa, confirmation of spin gap excitations in large-spin substances $RCrGeO_5$ (R = Y or Nd) by M. Hase, high-energy inelastic neutron scattering on $NiGa_2S_4$ by Y. Nambu, successive metal-nonmetal transitions with totally-symmetric electron ordering in $(Pr_{1-x}Ce_x)Ru_4P_{12}$ (part II) by K. Iwasa, and, proton entangled sates in double hydrogen bond system by S. Ikeda.

2. Instrumentation

The NBS experiments on the HRC became feasible after the improvement of the beam collimation. The computer environment was also improved for the data analysis and the instrument control, and some other developments were performed.

A collimator system was installed just upstream of the sample in order to reduce the background noise. The divergence of the incident neutron beams is controlled by the collimator, which is composed of slits of vertical cadmium sheets. The collimators with collimation of 0.3° and 1.5° are mounted in the collimator system, one of the two can be selected by an elevation mechanism with motor control. On the HRC, position sensitive detectors (PSD) are mounted at the scattering angles $\phi = 3 - 42°$ for conventional inelastic neutron scattering experiments, the background noise for these experiments was successfully reduced by using the 1.5° collimator. Also, on the HRC, PSDs are mounted at low angles down to $\phi = 0.5°$, the 0.3° collimator can reduce the background in this low angle

*Present address: Neutron Science Laboratory, The Institute for Solid State Physics, The University of Tokyo, Tokai 319-1106.

part. This 0.3° collimator is effective for NBS.

The computer environment is composed of data analysis software and an experiment control platform. The data analysis software was improved in the following points: the intensity normalization process for the inelastic neutron scattering from powder samples was improved, the analyzed data were transformed to the standard Mslice format for the convenience of users, and the process for alignment of the sample crystal became very easy. The experiment control platform was also improved, and therefore, almost all hardware on the HRC can be controlled from the computer terminal and these operations can be connected with the data acquisition (begin/end of running). In addition, a conceptual design for the analysis software and the experiment control platform was performed as a part of the improvement plan for the next year.

For conventional inelastic neutron scattering experiments, 128 pieces of 2.8 m-PSDs, which are mounted into two detector banks, cover $\phi = 3 - 42°$ at present. The PSDs for the next detector bank were purchased, and we will install them next year. The cryopump is being operated for high vacuum in the scattering chamber. The algorithm of the regeneration process of the cryopump was improved. The scattering chamber and its vacuum system were installed in 2009. The maintenance work for them was performed. In particular, the normal property of the large thin Al window on the surface of the chamber, which was designed on the assumption of a finite lifetime due to permitting the plastic deformation of the window, was confirmed. In order to cool the sample down to 4 K stably, a GM-type refrigerator was installed. Since cadmium slits were successfully used for the incident beam collimator, an oscillating radial collimator was manufactured for the collimation of the scattered neutron beam. Its performance will be investigated soon. A deck connecting the space of BL12 to the mezzanine was constructed, so the mezzanine in the 1st experimental hall was completed.

3. Neutron Brillouin Scattering Experiments

On the HRC, the NBS experiments became feasible by reducing the background noise at low scattering angles down to $\phi = 0.5°$. NBS is the most promising way to observe excitations in the forward direction from powders, polycrystals, or liquids. Owing to the kinematical constraints of neutron spectroscopy, incident neutron energy (E_i) in the sub-eV region is necessary for measuring scattering in the meV transferred energy (E) range close to (000), and with a high energy resolution of $\Delta E/E_i$, further, the scattered neutrons need to be detected at very low scattering angles (ϕ). Low angle detectors are essential to access the present energy momentum space. In fact, the region above the dashed line in Fig. 1, which is the envelope of scan loci

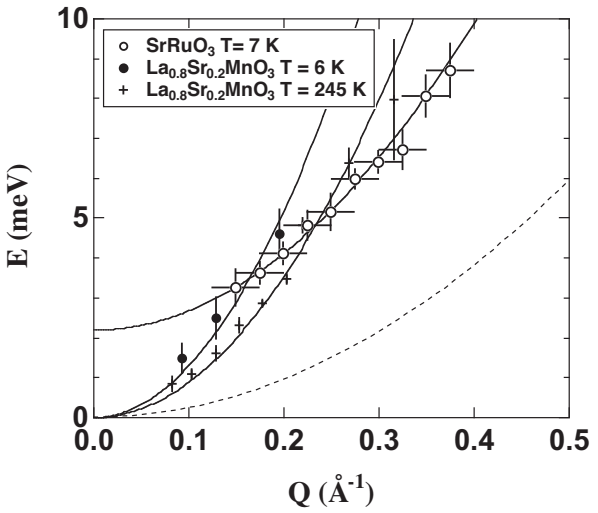

Fig. 1: Spin-wave dispersion curves for $La_{0.8}Sr_{0.2}MnO_3$ and $SrRuO_3$ determined on the HRC. The solid lines are fitted curves. The dashed line is the upper boundary accessible with a conventional spectrometer.

for $\phi = 5°$ with respect to E_i, can never be accessed using a conventional spectrometer with the lowest scattering angle of $\phi = 5°$, for instance.

First, NBS experiment was performed on the HRC to observe spin waves in a polycrystalline sample of a cubic perovskite, $La_{0.8}Sr_{0.2}MnO_3$, (Curie temperature: $T_C = 316$ K). Magnetic properties of this material are well elucidated and it has been already reported that spin waves were measured by using a single crystal sample. Figure 1 shows the dispersion relation of spin waves in $La_{0.8}Sr_{0.2}MnO_3$ measured with $E_i = 100$ meV, where $\Delta E/E_i = 2\%$. The observed dispersion relations at 6 and 245 K were well fitted to $E = DQ^2$, where Q is the scattering vector. The D values were obtained to be 130 ± 13 and 88 ± 2 meVÅ^2 at 6 and 245 K, respectively. These values are in good agreement with the results ($D = 131$ and 89 meVÅ^2 at 14 and 250 K, respectively) obtained by the previous inelastic neutron scattering experiments using a single crystal [2,3]. Therefore, the feasibility of the NBS experiments on the HRC was demonstrated [1].

Next, the spin waves in a polycrystalline ferromagnet, $SrRuO_3$ ($T_C = 165$ K), were similarly measured. This material also has a cubic perovskite structure, but a large single crystal suitable for inelastic neutron scattering experiments has not yet been synthesized. The measurement was performed at 7 K with $E_i = 100$ meV, and well-defined spin wave peaks were observed. As shown in Fig. 1, the dispersion relation of spin waves in $SrRuO_3$ was well fitted to $E = E_0 + DQ^2$ with an apparent energy gap E_0 [1]. This characteristic feature might originate from an induced spin anisotropy possibly from a spin-orbit coupling acting on the Ru 4d orbital. The anomalous Hall effect in $SrRuO_3$ was

theoretically interpreted as a strong spin-orbit interaction [4].

A strong permanent magnet $Nd_2Fe_{14}B$ shows demagnetization at high temperatures. The recovery of magnetization at high temperatures is possible by adding Dy, which is a rare element. One of the aims in the element strategy project is to develop Dy-free magnet. Before development, evaluation methods of materials should be established. We measured spin waves in $Nd_2Fe_{14}{}^{11}B$ polycrystals at 300 K and 6 K with E_i = 250 meV. As shown in Fig. 2, assuming there exists a spin wave peak in the observed range, the peak positions are just on the dispersion relation along the c-axis determined by the previous single crystal experiment [5]. To determine the interaction parameters from these data, theoretical support is required.

Acoustic phonons in liquid D_2O were observed. It was reported, previously, the observation of broad spectra with E_i = 80 meV and ΔE = 4.8 meV and the determination of the dispersion relation of the acoustic phonons [6]. We measured with E_i = 100 meV and ΔE = 2 meV with a better resolution and within a wider energy range. Similar spectra to the previous data were obtained with a slightly wider energy- momentum space, as shown in Fig. 3.

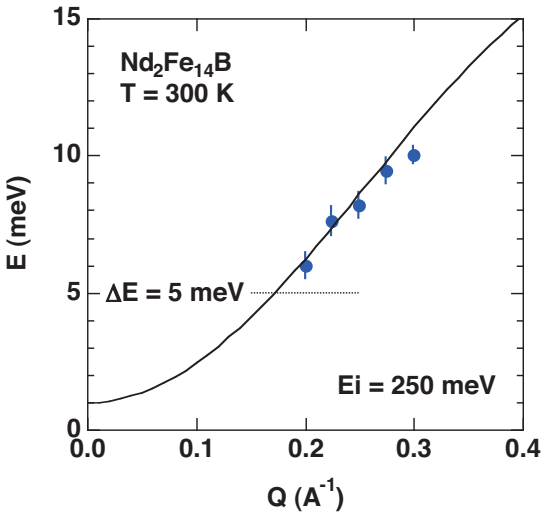

Fig. 2: Spin wave dispersion relation of $Nd_2Fe_{14}{}^{11}B$ observed on the HRC. The solid line is the dispersion curve along the c-axis determined using a single crystal sample.

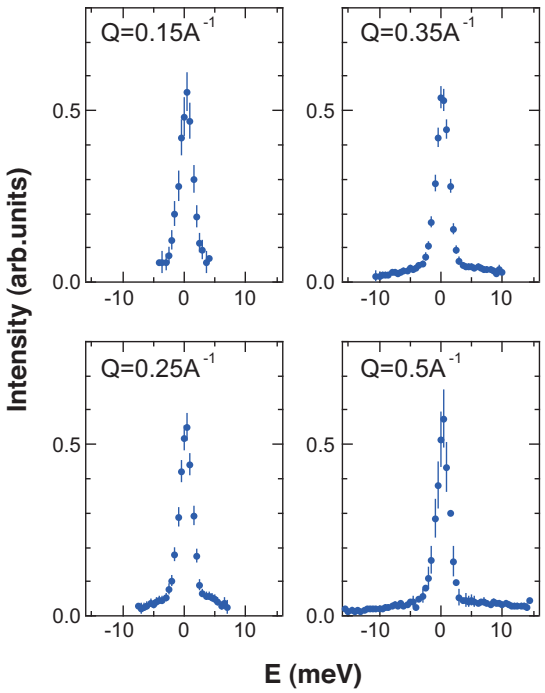

Fig. 3: Inelastic scattering spectra for liquid D_2O. The broad spectra beside the elastic scattering are acoustic phonons.

4. Experiments and Results

4.1 Search of Orbital Waves in YVO_3

The orthorhombic perovskite YVO_3 shows the G-type orbital ordering in the temperature range from 200 to 77 K [7]. In this phase, the existence of large orbital fluctuations is suggested [8], and dispersive orbital waves propagating along the *c*-axis, due to the one-dimensional spin-orbital correlations, are predicted [9]. In consideration of the neutron scattering cross-section obtained from the correlation function for the orbital angular moment, we attempted to detect the orbital waves. Figure 4 shows the observed spectra in the orbital ordered phase (133 K), subtracted from those in the orbital disordered phase (214 K). The intensity decreases with increasing $|\boldsymbol{Q}|$, where $\boldsymbol{Q} = h\boldsymbol{a}^* + k\boldsymbol{b}^* + l\boldsymbol{c}^*$, which can be explained by the magnetic form factor for the V^{3+} orbital. In addition, we found that the intensity shows a periodic behavior with the maximum at l = odd number. This indicates that the observed spectra originate from the orbital waves. This experiment was performed using the fine-resolution Fermi-chopper spectrometer, SEQUOIA at SNS, ORNL, as one of the substituted proposals related to the disaster of the earthquake on March 11, 2011.

4.2 Mind the "Gap" on Quantum Spin Systems

Quantum spins in a low-dimensional system show unusual quantum phases such as Haldane system and spin-Peierls state, by strong quantum nature. In particular, spin singlet is the basic starting point describing a ground state of the quantum spin chain. Another subject of interest in quantum spin systems is the cooperation among physical degrees of freedoms. The strong correlations between quantum spin and charge, orbital, and lattice are expected to give rise to a fascinating new quantum phase as a realization of high-T_c superconductivity in two-dimensional system.

1) Finding the Gap in TiOBr ∼ A Novel Spin-Peierls System? ∼: The newly proposed spin-Peierls system TiO*X* (*X*: Cl, Br) has been revealed showing

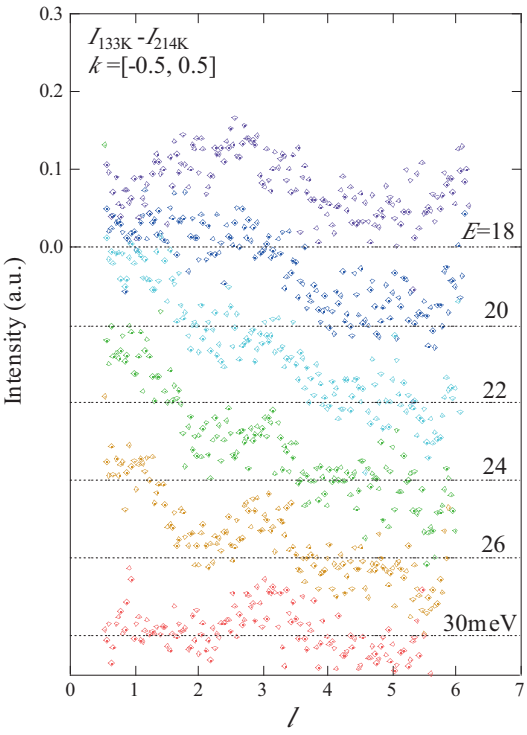

Fig. 4: Inelastic neutron spectra in the orbital ordered phase (133K), subtracted from that in the orbital disordered phase (214K). The horizontal axis l is the propagating direction of the predicted orbital waves.

one-dimensional (1D) nature associated with orbital ordering of Ti ions and super-lattice structure being related to the Peierls instability. It is pointed out that as a result only from an arrangement of Ti d_{xy} orbital, 1D spin chains and the spin-Peierls transition will be formed. Recently, it has been demonstrated that TiOBr also exhibits two successive phase transitions similar to TiOCl at T_{c1}=27 K and T_{c2}=47 K. Inelastic neutron experiments were carried out in order to find the direct evidence of a spin-Peierls transition, namely, the spin gap. The inelastic spectrum with a large amount of poly crystalline sample of TiOBr is expected to show the localized signal in the vicinity of the magnetic zone center Q=0.9 Å^{-1}. This low-Q access measurement of poly crystalline sample is only done by small angle and high incident energy (E_i) condition. Detectors at around 3 degrees of scattering angle and 200 meV of E_i are used for searching the excitation at the low-Q region. However, the obtained S(Q,E) shows no indication of the existence of magnetic signals in the spectrum except for phonon contribution. The gap energy in TiOBr is expected to be much higher than that measured in thermodynamic properties and by analogy with TiOCl, and could be 20 meV in energy. It still remains an open question if the spin-Peierls state under the cooperation of orbital ordering is realized in this system.

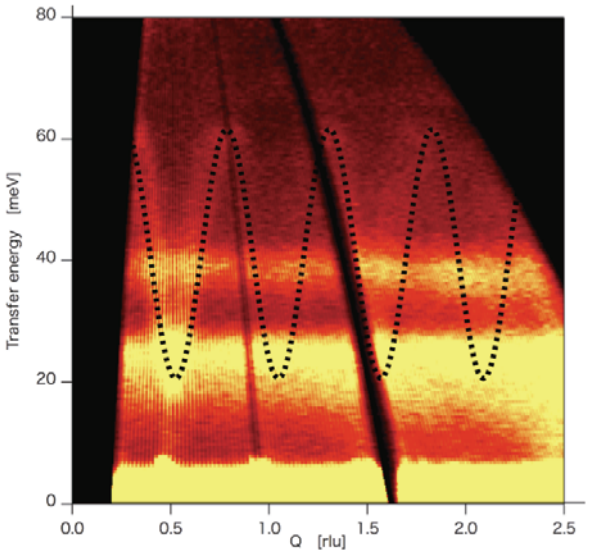

Fig. 5: Observed S(Q,E) spectrum of $Nd_{1.965}Ca_{0.035}BaNiO_5$.

2) Hole Dynamics in a 1D Spin Chain: It is practically hard to realize the carrier doping in 1D material because the localization of carriers occurs at a low temperature. We tested spin and hole dynamical properties in $Nd_{2-x}Ca_xBaNiO_5$, which is successfully hole doped 1D Haldane system. The lightly doped x=0.035 carrier content were measured by means of pulsed neutron inelastic scattering as shown in Fig. 5. It clearly shows the entire one-magnon band with spin gap (Haldane gap) at the magnetic zone center (MZC) addition to the intense cystal field excitation of Nd ions. The energy at the zone boundary reaches 60 meV that is less compared to the undoped Haldane chain. On the other hand, the gap slightly increases in its energy, but still the gap opens even with holes doped (spin correlation of Haldane state is known to be spatially exponential). Moreover, new dynamical structures within the Haldane gap were observed upon carrier doping, showing incommensurate structures centered at MZC. This originates from the dynamics of the doped- holes. For further experiments, we will focus our attention on the hole carrier dependence of the Ni chain band (Haldane band) and hole dynamics.

4.3 Multiferroic Compounds

RFe$_3$(BO$_3$)$_4$ (R=rare earth metal) are a series of multiferroic compounds that crystallize trigonal structure with three fold screw chains of FeO$_6$ octahedra and R^{3+} ions along the crystallographic c direction. In R=Nd compound easy-plane type Néel order and spontaneous electric polarization appear simultaneously at T$_N$=30 K. The weiss temperature is -115 K and the frustration ratio is -3.8. Thus the compound exhibits multiferroic property as well as the behavior of a frustrated magnet. While the magnetic structure was studied in detail [10], the magnetic excitation was mea-

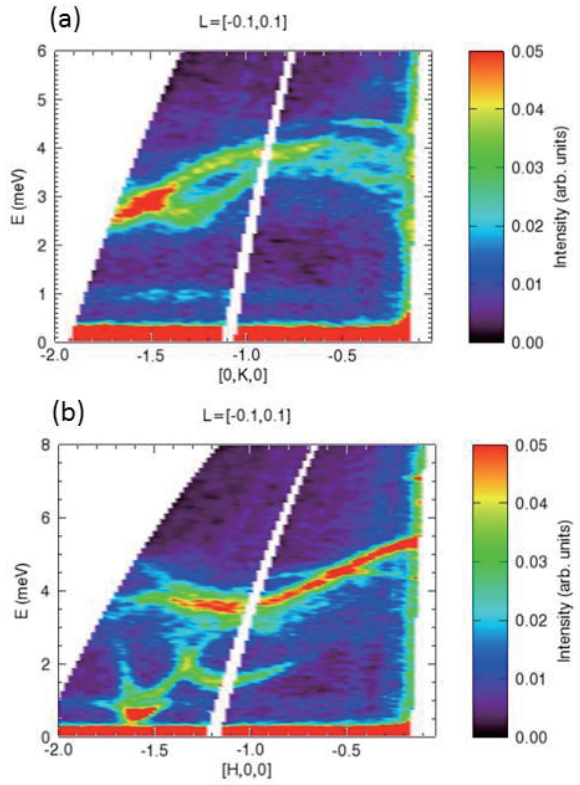

Fig. 6: Inelastic neutron scattering spectrum of $NdFe_3(BO_3)_4$ in case of k_i // a^* (a) and k_i // c^* (b).

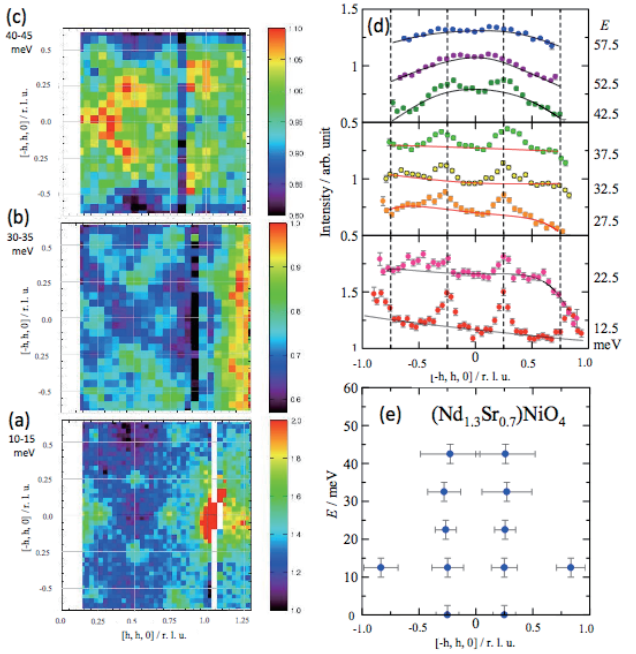

Fig. 7: Neutron-scattering measurements from $(Nd_{1.30}Sr_{0.70})NiO_4$ measured on HRC (BL12). (a) - (c) Constant energy slices showing the variation of the intensity in the (h, k) plane at different energies. The data are averaged over the range of energies indicated in the figure. (d) Constant energy cuts along [-H, H, 0] directions at various energies. The data are averaged over (H, H) = (1.0, 1.0) ± (0.1, 0.1). (e) Dispersion of the magnetic excitations in $(Nd_{1.30}Sr_{0.70})NiO_4$ along [-H, H, 0] direction.

sured only by using electromagnetic wave including ESR and Raman scattering techniques. An inelastic neutron scattering (INS) experiment to measure the $S(\mathbf{q},\omega)$ in wide $\mathbf{q}$ space is the most effective method to identify the spin Hamiltonian realized in the compound. 22 pieces of single crystals were coaligned by X-ray Laue camera so that a^*-c^* plane was the scattering plane. The total mass of the sample for INS experiment was 2.1 g. The T0 chopper was set at 50 Hz, 1.5° of collimator was installed in front of the sample, and a Fermi chopper, "S", with 200 Hz was used to obtain high neutron flux. GM-type refrigerator was used to achieve a temperature of 15 K. Figure 6 (a) shows the spectrum obtained at the configuration of k_i parallel to the crystallographic a^* direction. Flat mode at $\hbar\omega \sim 1$ meV is crystal field excitation of Nd ion, which was consistently observed by the ESR and Raman scattering experiment [11,12]. The dispersive modes at 2.5 meV $< \hbar\omega <$ 4.5 meV have not been identified yet but they would possibly originated from collective spin wave excitation from Fe^{3+} ions. Figure 6 (b) is the spectrum of k_i parallel to the c^* direction. In addition to the modes observed in Fig. 6 (b), dispersive mode with anisotropy gap of 0.5 meV is observed. The anisotropy energy scale is consistent with that of an Fe^{3+} system observed in the ESR experiment [11]. In fiscal year 2013 we will collect the $S(\mathbf{q},\omega)$ in wide $\mathbf{q}$ space by rotating crystals to identify the spin Hamiltonian realized in this compound.

4.4 Unusual Spin Dynamics in the Checkerboard Order in Two-Dimensional Layered Nickelate

When the antiferromagnetic insulating phase is melted by carrier doping in the layered transitionmetal oxides, the hole doping stabilizes the nontrivial spin-charge ordering towards the metalinsulator transition. In particular, the doped carriers tend to form stripe or simple square-lattice checkerboard patterns. Although the magnetic excitations in the insulating stripe phase region can be explained by the linear spin-wave approximation with in-plane magnetic anisotropic exchange parameters, a breakdown of the linear spin wave approximation was observed in the magnetic excitations in the checkerboard phase with higher carrier concentration. The spin dynamics in the checkerboard phase of $(La_{2-x}Sr_x)NiO_4$ (x = 0.5) and more metallic $(Nd_{2-x}Sr_x)NiO_4$ (x = 0.6, 0.7) are systematically investigated by an inelastic neutron scattering experiment using a large single crystals grown by the floating-zone method. We found that the observed magnetic excitations in the checkerboard phase is qualitatively different from those of the more insulating stripe phase.

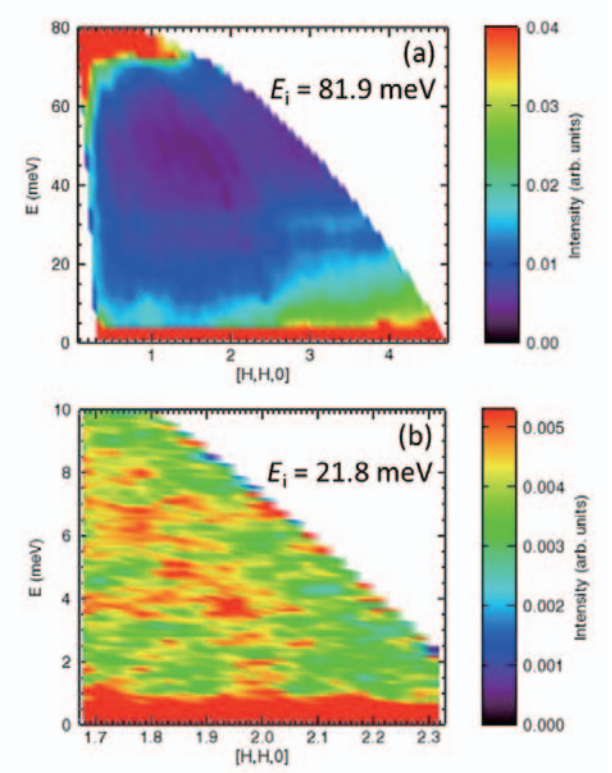

Fig. 8: Contour maps of intensity in $Cs_2Cu_3SnF_{12}$ as a function of energy and inplane wave vector for (a) $E_i = 81.9$ and (b) 21.8 meV. The intensity is integrated over the whole reachable range of (0,0,L) and (-K,K,0).

They do not show behavior of counter-propagating spin wave branches up to $\Delta E \sim$ 70 meV as shown in Fig. 7 (a-e), but are rather similar to those in the high Tc cuprates which show straight-up chimney-like excitations.

4.5 Kagome Lattice Antiferromagnet

Geometrical frustrated systems with reduced spatial dimensionality have gathered considerable interest. They can suppress conventional magnetic orders, and eventually induce novel states of magnetism. Here we concentrate on Kagome lattice antiferromagnet (KAF), which is composed of corner-sharing triangles. Since no candidate material of KAF with exact lattice geometry and strong two-dimensionality have so far been reported, low- temperature magnetism remains controversial. There have been indeed reported several scenarios to describe the magnetism of KAF in theories. One of the intriguing subjects is if the excitation from nonmagnetic ground state to magnetic excited state is gapfull or gapless. We have recently examined a prominent example of $S = 1/2$ systems, $Rb_2Cu_3SnF_{12}$, and revealed the pinwheel valence bond solid ground state. In addition, an analogue $Cs_2Cu_3SnF_{12}$ with $S = 1/2$ is revealed to magnetically order into the so-called $Q = 0$ structure. Through inelastic neutron scattering experiments, we successfully estimated the coupling constants of spins. To gain further insight into the detailed view of magnetic excitations of this compound, we performed an inelastic neutron scattering measurement on BL12 HRC. A single crystal was mounted on the (HHL) horizontal scattering plane and the (00L) was set to be parallel to the incident neutron beam. We measured spectra at $T = 5$ K using a CCR with $E_i = 81.9$ meV. Due to lack of sample mass and beam intensity, we were unable to obtain conclusive data and only phonon signals were observed at high-Q regime (Fig.8(a)). Owing to the multi-E_i system of HRC, however, we succeeded in detecting magnetic signals spanning G-point (2,2,0) to K-point (5/3,5/3,0) with $E_i = 21.8$ meV, which is in good accord with the recent results of triple-axis and BL14 AMATERAS spectrometers (Fig.8(b)). We will hereafter pursue its magnetic origin, and induce quantum critical phenomena by diluting such chemically analogous systems showing distinct low-temperature magnetism.

4.6 Intermultiplet Transition in Filled Skutterudite Compound $SmFe_4P_{12}$

Samarium-based filled skutterudite $SmFe_4P_{12}$ was reported to be the first ferromagnetic Kondo-lattice compound. It shows an unconventional heavy-electron state with a large electronic specific-heat coefficient 370 mJ/mol K^2 and a ferromagnetic transition at 1.6 K. Although the 4f electrons clearly play a key role in the formation of heavy quasiparticle at low temperatures, there has been lack of basic information about the 4f electronic states in this system because neutron scattering experiments on materials containing thermal neutron absorber elements such as Sm. To avoid this problem, we conducted an INS experiment on $SmFe_4P_{12}$ by using higher energy neutrons. Figure 9 shows the inelastic neutron spectra of polycrystalline $SmFe_4P_{12}$ at 6.5 K and 280 K. The sample was prepared by using a tin flux method, where natural abundant Sm isotopes were used. In the low Q range, a small peak around 80 $\sim$ 90 meV was observed at low temperature. This peak is not visible in high Q range, indicating that it is of magnetic origin. If this peak is associated with the intermultiplet transition from $J = 5/2$ ground state to $J = 7/2$ multiplet, interestingly, the energy splitting is very small compared to usual Sm-based compounds. This might originate from the strong c-f hybridization in filled skutterudite compounds.

4.7 Magnetic Excitations in Antiferromagnetic Alternating Spin-3/2 Chain Substance $SmCrGeO_5$

One interesting phenomenon in quantum spin systems is the appearance of a spin-singlet ground state with a spin gap (singlet-triplet excitation). When the spin value is larger than 1, the existence of a spin-singlet ground state with a spin gap has not been proven experimentally. We can expect antiferromagnetic (AF) alternating spin-3/2 chains of Cr^{3+} in $SmCrGeO_5$ and

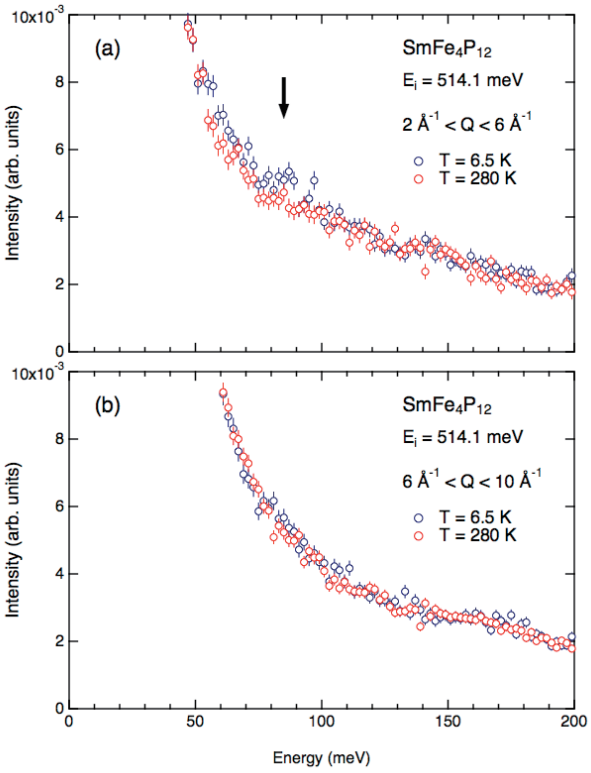

Fig. 9: Inelastic neutron spectra of $SmFe_4P_{12}$ at T = 6.5 K and 280 K for (a) momentum transfer range 2 Å^{-1} < Q < 6 Å^{-1} and (b) 6 Å^{-1} < Q < 10 Å^{-1}.

a spin-singlet ground state with a spin gap. We performed inelastic neutron scattering experiments on $SmCrGeO_5$ powders to confirm the spin gap excitation. Excitations were apparent between 15 and 25 meV at 7.8 K. The intensities of the excitations were strong in the small Q range and decrease with increasing the temperature. Therefore, most of the excitations are magnetic excitations. We could confirm a spin gap in the magnetic excitations. Figure 10 shows the intensity map in the ω-Q_{1D} plane at 7.8 K obtained using the conversion method developed by Tomiyasu et al. The results correspond to results of a single crystal measured along the spin chain direction. The intensity is strongest around $Q_{1D} = 0.5$ as expected in AF spin chains. The white line shows $\omega = \sqrt{13.8^2\ sin^2(2\pi Q_{1D}) + 18.6^2}$. The spin gap value is estimated as 18.6 meV. The dispersion is apparent below $Q_{1D} = 0.75$.

4.8 Spin Density Waves in Chromium

The spin-density wave (SDW) in Cr is one of the most fascinating subjects in condensed matter physics. It has a history of long and continuing research. One of the open issues is its magnetic excitation, which arises from incommensurate magnetic Bragg positions with a steep dispersion slope and extends to more than 600 meV. In order to examine the detailed structure of the high-energy magnetic excitations of Cr in ($\boldsymbol{Q}$, ω)

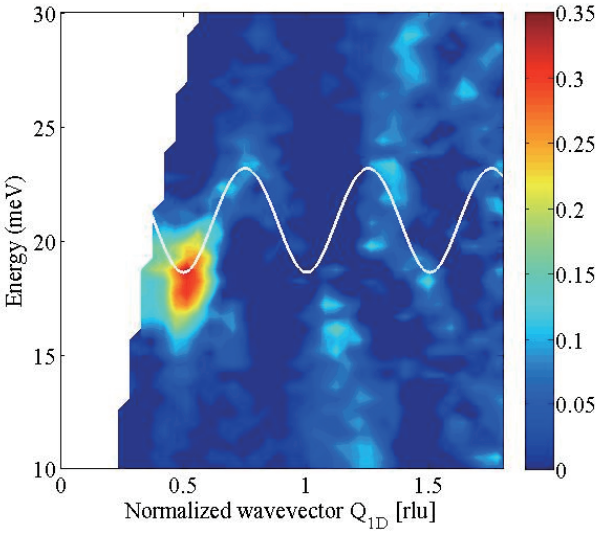

Fig.10: The intensity map in ω-Q_{1D} plane obtained from the data of $SmCrGeO_5$ at 7.8 K with E_i = 91.6 meV. Q_{1D} is Q parallel to the spin chain and is normalized by 2π/d, where d is the Cr-Cr average distance (0.286 nm).

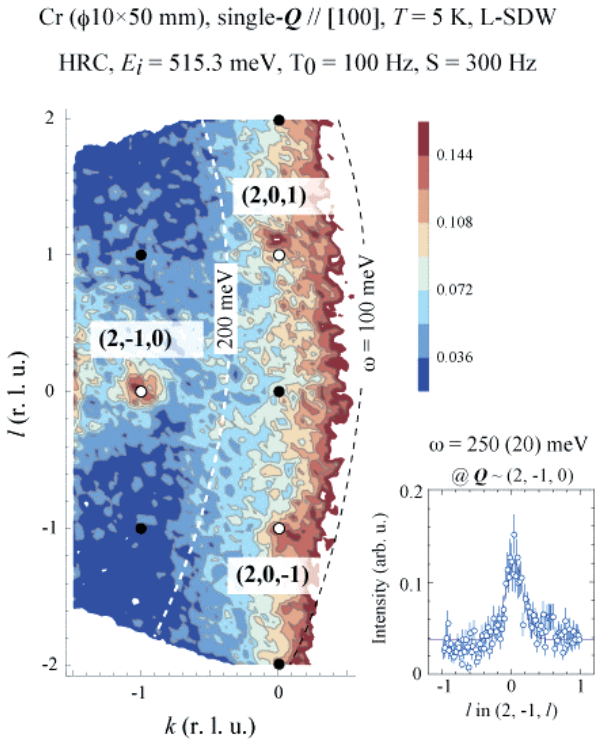

Fig. 11: Intensity contour onto (2, k, l) plane with a thickness of 1.9 ≤ h ≤ 2.1. The inset shows a line cut profile along l at (2, -1, 0) integrating within a range of 1.9 ≤ h ≤ 2.1 and -1.1 ≤ k ≤ -0.9.

space, we performed inelastic magnetic neutron scattering on HRC using a single crystal with 4 cc in volume. Figure 11 shows an intensity contour map in the longitudinally-spin-polarized SDW state, where the intensi-

ty is projected on (2, k, l) plane over a wide energy range. Sharp spots appear at three magnetic Γ points: (2, -1, 0) at ω = 250 meV, and (2, 0, $\pm$1) at ω = 150 meV. The line-cutting profiles along l direction are an evidence that the magnetic cross sections are well localized in $\boldsymbol{Q}$ space. No consensus has been established yet for this novel high-energy excitation. One scenario is based on spin-wave excitations from a pseudo localized-spin system with a zone-boundary energy of $\sim$1 eV, though Cr is usually regarded as a typical itinerant-electron system. Another possibility comes from electron excitations across the Fermi energy, possibly reflecting the peculiar Fermi surfaces. Further experimental studies toward high-energy region are required not only to settle such the argument, but also to get a clue to unknown spin dynamics in metallic magnets.

4.9 Collective Dynamics of Hydrated β-Lactoglobulin

Protein hydration plays a fundamental role in protein behavior: water-protein interactions affect protein folding, maintain structural integrity, mediate molecular recognition, and accelerate enzymatic catalysis. Many scattering measurements, both elastic and inelastic, and many molecular dynamics simulations, have been performed to investigate the relation between protein dynamics and that of the surrounding solvent molecules. Single particle dynamics of proteins and hydrated water have been investigated using incoherent scattering from hydrogen in hydrated protein powder. On the other hand, the investigation of collective dynamics of proteins and hydrated water using coherent scattering is relatively scarce although it contains important information of structure and dynamics. First, we performed an NBS experiment of pure D_2O at room temperature on HRC, as mentioned above. The fast sound mode due to the collective dynamics of water was detected as well as the inelastic X-ray scattering [13]. Next, hydrated β-lactoglobulin powder (water 0.4g/ dry protein g) was measured at 298 K -180 K. The sample dimension was 40 $\times$ 40 $\times$ 8 mm. Figure 12 shows INS signals of the sample at different Q values. The spectra show well-defined acoustic excitations as shoulders (see arrows in the figure) that change in excitation energy with Q in the low Q region. This trend is similar to the results of hydrated ribonuclease A measured on BRISP (ILL) [14]. The analysis is in progress.

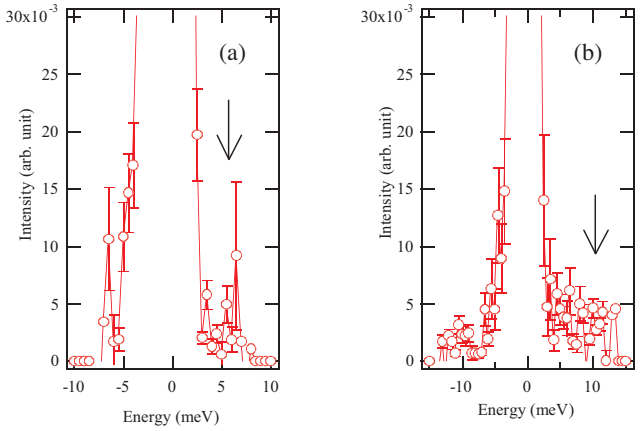

Fig. 12: Inelastic neutron spectra of hydrated β-lactoglobulin at 180 K for (a) momentum transfer range 2 Å^{-1} < Q < 3 Å^{-1} and (b) 5 Å^{-1} < Q < 6 Å^{-1}

Acknowledgements

We are grateful to Y. Kaneko, Y. Tokura, and M Fujita for preparing the perovskite samples for the NBS experiments. The collaborators are N. Inami and Y. Takeichi for the experiment on $Nd_2Fe_{14}B$, T. Nakabayashi and S. Suzuki for the experiment on the two-dimensional nickelates, S. Konno, Y. Utsumi, and A. Suzuki for the experiment on $SmFe_4P_1$, T Fukuda and K. Ikeuchi for the experiment on Cr.

References

[1] S. Itoh *et al.*, J. Phys. Soc. Jpn. 82 (2013) 043001.
[2] F. Moussa *et al.*, Phys. Rev. B 76 (2007) 064403.
[3] K. Hirota and Y. Endoh, J. Phys. Soc. Jpn. 66 (1997) 2264.
[4] Z. Fang *et al.*, Science 302 (2003) 92.
[5] H. M. Mayer *et al.*, J. Magn. Magn. Mater. 97 (1991) 210.
[6] J. Teixeira *et al.*, Phys. Rev. Lett. 55 (1985) 2681.
[7] S. Miyasaka *et al.*, Phys. Rev. B 73 (2006) 224436.
[8] C. Ulrich *et al.*, Phys. Rev. Lett. 91 (2003) 257202.
[9] S. Ishihara, Phys. Rev. B 69 (2004) 075118.
[10] M. Janoscheket *et al.*, Phys. Rev. B 81 (201) 094429 .
[11] A.M. Kuz'menko *et al.*, JETP Letters 94 (2011) 294.
[12] M.N. Popova, Phys. Rev. B 75 (2007) 224435.
[13] G. Ruocco *et al.*, Nature 379 (1996) 521.
[14] A. Orecchini *et al.*, J. Am. Chem. Soc. 131 (2009) 4664.

Studies of Neutron Optics for Physics Researches

Y.Arimoto[a], T.Ino[a], S.Muto[a], K.Taketani[a], H.Oide[a], T.Yoshioka[b], H.Otono[b], K.Mishima[c], S.Yamashita[c], H.Sumino[d], S.Imajo[e], Y.Iwashita[e], M.Yamada[f], Y.Seki[f], Y.Otake[f], Y.Yamagata[f], P.Geltenbort[g], K.Hirota[h], M.Kitaguchi[h], H.M.Shimizu[h], T.Shima[i], H.Funahashi[j], K.Asahi[k], and Y.Kiyanagi[l]

[a]*Neutron Science Division, High Energy Accelerator Research Organization (KEK), 1-1 Oho, Tsukuba, Ibaraki 305-0801, Japan*
[b]*Faculty of Science, Kyushu University, Fukuoka 812-8581, Japan*
[c]*International Center for Elementary Particle Physics, University of Tokyo, Hongo, Bunkyo, Tokyo 113-0033, Japan*
[d]*Faculty of Science, University of Tokyo, Hongo, Bunkyo, Tokyo 113-0033, Japan*
[e]*Institute for Chemical Research, Kyoto University, Gokasho, Uji, Kyoto 611-0011, Japan*
[f]*RIKEN, 2-1 Hirosawa, Wako, Saitama 351-0198, Japan*
[g]*Institut Laue Langevin, 6 rue Jules Horowirz, BP 156 - 38042 Grenoble Cedex 9, France*
[h]*Department of Physics, Nagoya University, Nagoya, Aichi 464-8603, Japan*
[i]*Research Center for Nuclear Physics, Osaka University, Ibaraki, Osaka 567-0047, Japan*
[j]*Department of Physics, Kyoto University, Kitashirakawa-Oiwakecho, Sakyo, Kyoto 606-8502, Japan*
[k]*Department of Physics, Tokyo Institute of Technology, 2-12-1 O-Okayama, Meguro, Tokyo 152-8551, Japan*
[l]*Faculty of Engineering, Hokkaido University, Sapporo, Hokkaido 060-8628, Japan*

1. Overview

At the NOP beamline (Neutron Optics and Physics) installed at the port BL05, the final preparation for neutron lifetime measurement and some other researches and developments are continuing. The time projection chamber (TPC) designed to detect neutron beta decay was adjusted precisely for data acquisition with high quality at high polarization beam branch. Neutron guide tubes were installed in upstream of the unpolarization neutron beam branch to extract very slow neutrons for UCN experiments. The chamber for gas scattering experiments was tested at low divergence beam branch.

2. Polarized Beam Branch

The recent values deviate far beyond the systematic errors claimed in the past and require further improvement with an accuracy of 10^{-3} in measurement methods other than the ultracold neutrons for consistency with the primordial nucleosynthesis. We are continuing the neutron lifetime measurement at the polarized beam branch of the NOP beamline installed at port BL05. The system consists of a neutron chopper and a gas chamber [1] for detecting the electrons from the neutron β-decay. This method was applied in the past by introducing monochromized neutron beam bunches into a gas chamber as reported in Ref. [2]. The continuous neutron beam from a reactor source was monochromized and chopped in the experiment, which resulted in poor statistics. The intense pulsed neutron source enables us to overcome the disadvantage by chopping the cold neutrons synchronizing to the neutron time of flight. We have already developed and installed the neutron spin-flip chopper (SFC) for this purpose [3]. The time sequence of chopping is selected so that each neutron bunch reaches the detector fiducial volume with fully separated time from the other bunches. The SFC is working stably with an S/N ratio better than 400:1.

The gas chamber for the detection the electrons is a time projection chamber (TPC) containing diluted ^{3}He and the rate of the ^{3}He$(n,p)^3$H reaction is measured by counting the protons. The neutron lifetime is measured as the ratio of the electron events to the proton events. The background event rate has been remarkably suppressed by employing cosmic-ray veto counters, radiation shields, low-radioactivity materials for chamber components and neutron absorbers covering the inner surface of the detector chamber.

We have started the measurements of neutron lifetime, while the detector response has been studied by the commissioning (Fig. 1). The ^{3}He density and the gas pressure, which cause the systematic uncertainty of the measurement, are also studied by using a mass

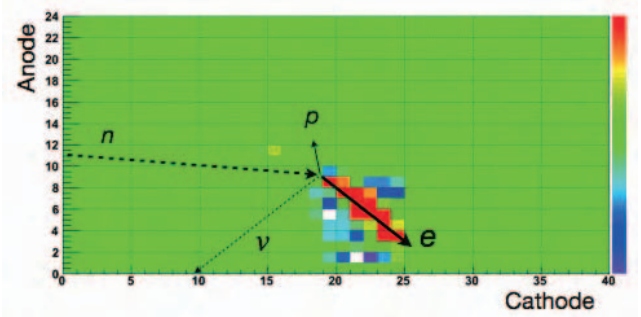

Fig. 1: Typical display of neutron β-decay event.

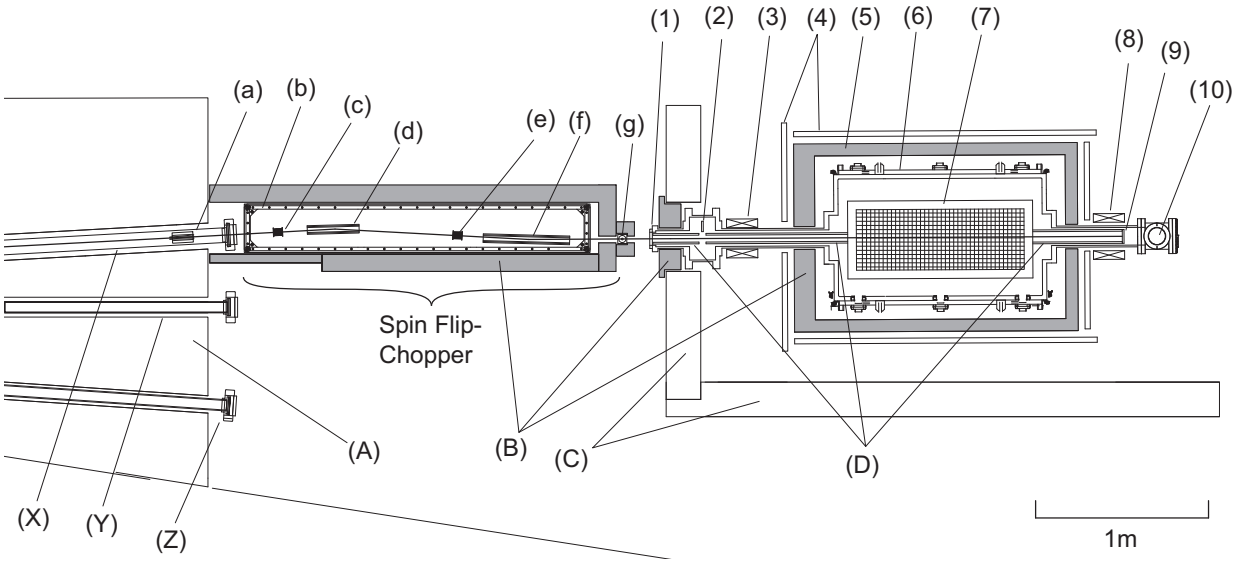

Fig. 2: A drawing of the experimental setup: (A) beam dump, (B) lead shield, (C) iron shield, (D) ^{6}LiF-PTFE beam collimator, (X) Polarization branch, (Y) Unpolarization branch, (Z) Low divergence branch, (a) short-pass wavelength neutron lter, (b) guide coil, (c) spin ipper, (d) magnetic super mirrors, (e) spin ipper, (f) magnetic super mirrors, (g) neutron beam monitor, (1) Zr window, (2) neutron switching shutter, (3) electron suppression magnet, (4) cosmic veto counter, (5) lead shield, (6) vacuum chamber, (7) TPC, (8) electron suppression magnet, (9) ^{6}LiF beam catcher, and (10) turbo molecular pump.

spectrometer. The precise analysis of the data is also in progress. Consequently, we estimate that the experimental error of about 10^{-2} can be achieved within 150 days with the primary proton beam power of 220 kW.

3. Unpolarization Beam Branch

In order to increase the neutron flux, we installed supermirror guide tubes of $m = 2.0$ instead of a vacuum guide during shutdown in the summer of 2012 (Fig. 3). The neutron spectra with/without beam ben-der measured by a neutron beam monitor are shown in Fig. 4. The intensities were normalized by using the proton beam power and the efficiency of the beam monitor. The total intensity increased 4.1 times by the bender, since it was 4.0×10^8/cm^2/s with the bender and 9.6×10^7/cm^2/s without the bender assuming 1 MW beam power.

A Doppler shifter is working at an Unpolarization beam branch to produce Ultra Cold Neutron (UCN), which is neutron with velocity of less than 7 m/s. The Doppler shifter is rotating with synchronizing the neutron pulses so that it produces pulsed UCNs which are unique in the world. However, the intensity of the UCN from the Doppler shifter was as low as about 0.3 cps with 100 kW beam power. The Doppler shifter converts from neutrons of 3.0 nm to UCNs. New neutron guides and monochromatic mirrors were also installed to increase the number of 3 nm-neutrons into the Doppler shifter. A neutron spectrum obtained by the Doppler shifter is shown in Fig. 5. Note that the efficiency of the UCN detector was degraded by a leak but was corrected. As a result, the intensity of neutrons from the Doppler shifter, consisting of UCNs and faster neutrons, was 49 cps with 300 kW proton beam power. It means that by improving the neutron optics the intensity increases by about 20 times. The result was consistent with a simulation within 15%.

Fig. 3: Installation of supermirror guide tubes in unpolarization branch.

The UCNs are mainly used for developing devices for the next-generation experiment to search neu-tron electric dipole moment, which requires UCNs with high

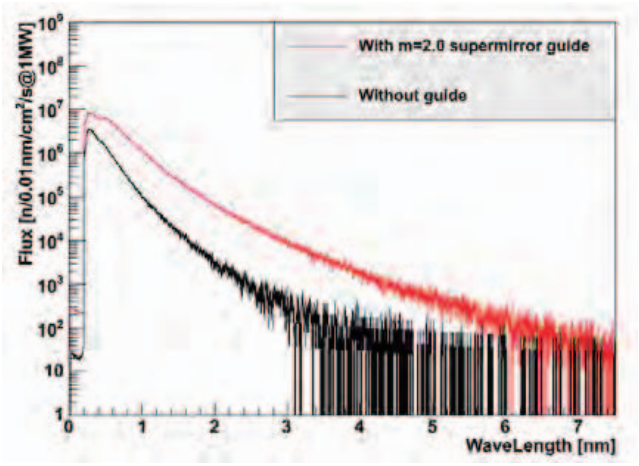

Fig. 4: Neutron spectra with (red) and without (black) the neutron guide measured by a beam monitor at the exit of an unpolarization beam branch. The intensities were normalized by using the proton beam power and the efficiency of the beam monitor.

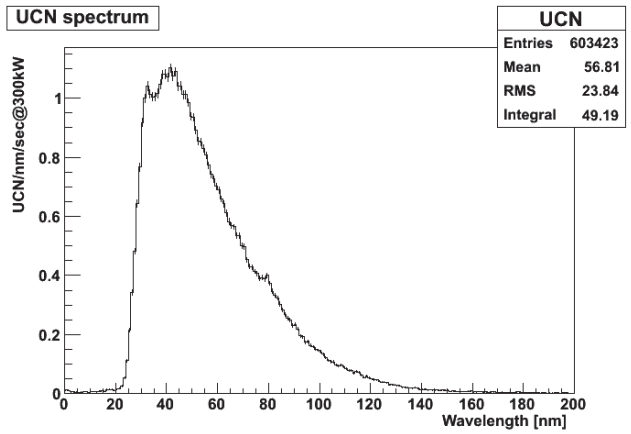

Fig. 5: Wavelength spectrum of neutrons from the Doppler shifter. The total intensity is 49 cps with 300 kW proton beam.

density. The time focusing optics, which functions as the spatial compression of pulsed neutrons along the beam axis, enables us to deliver denser UCNs into the storage volume for the physics experiment. We performed demonstration of the time focus of chopped UCNs to rebunch them at the TEST beam port of the ILL/PF2. Figure 6 shows the experimental apparatus. An RF field applied in the gradient field flips the neutron spin when the RF frequency coincides with the Larmor precession frequency. The neutron accelerator was made by using magnet with anisotropic inter-pole and RF coil with variable frequency. We successfully measured the UCN focusing by sweeping the RF frequency so that the bunched UCNs reach the detector at the same time. The results are in good agreement with the simple simulations that control the velocities of the neutrons (Fig. 7) [4]. However, the focusing of the bunch was not so sharp because the spin ip efficiency was low and the range of quantity of acceleration was narrow. Currently, we have developed a new accelerator system with more efficient spin ip and wider RF frequency. RF power supply with 3 kW and a resonance circuit system with six variable capacitors has been developed. We are now preparing the precise measurement of time-focusing by using UCNs from the Doppler shifter at the unpolarization branch. The sharp UCN pulse also enables us to get the spectra with sharp focusing. The combination of high instantaneous UCN density and time focusing transportation enables us to improve the experimental sensitivity to the level of the new physics beyond the standard model of elementary particles through the measurement of electric dipole moment [5].

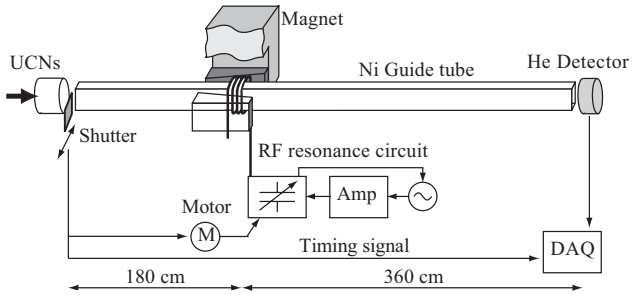

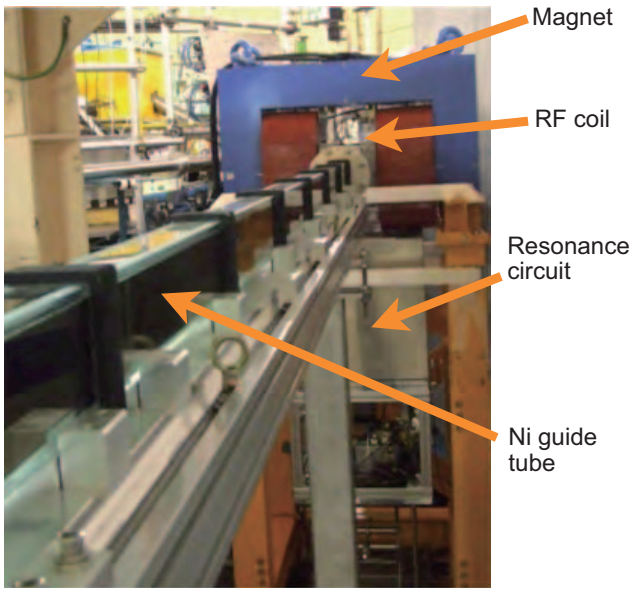

Fig. 6: Experimental Setup at ILL/PF2. Neutrons are incident from the left and transported to the right through the static magnet and RF coil.

4. Low Divergence Beam Branch

A measurement of angular distribution of scattering cross section is planned for the search of unknown medium range interactions between neutrons and neutral atoms using an unpolarization beam branch. Because the change of cross section which is caused by the un-

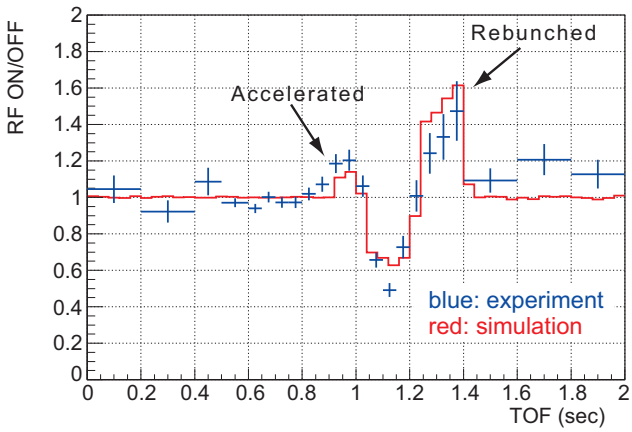

Fig. 7: The ratio of two TOF histograms with and without focusing.

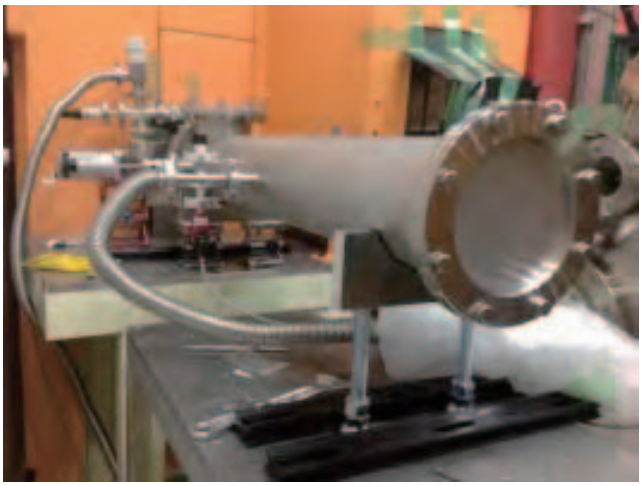

Fig. 8 : Setup for precise measurement of scattering from window material at Low Divergence Beam Branch.

known force is small, the scattering from the window material of the chamber for the neutral atom gas must be large background for the measurements. We have started the precise studies of the scattering from the window material. Well-collimated neutron beam at low divergence beam branch was injected into thick silicon block as a scatterer large enough to measure precisely (Fig. 8). We are now able to discuss the feasibility to use it for the experiment.

5. Neutron Sources at Users' Sites

Linear proton accelerators for small-scale neutron sources was installed both in the Department of Physics of Kyoto University and RIKEN. The first beam has been successfully delivered for both sources.

6. Acknowledgement

This work was partially supported by the Creative Scientific Research Grant (no.19GS0210) of the Japan Society for Promotion of Science and the S-type Research Program (no.2009S03) of the Institute of Material Structure Science of KEK.

References

[1] H. Otono, Dr. Sc. dissertation (Univeristy of Tokyo, 2012).
[2] R. Kossakowski, *et al.*, Nucl. Phys. **A503** (1989) 473.
[3] K.Taketani, *et al.*, Nucl. Instr. Meth. Phys. Res. **A634** (2011) 134.
[4] Y. Arimoto, *et al.*, Phys. Rev. **A86** (2012) 023843.
[5] H. M. Shimizu, *et al.*, Nucl. Instr. Meth. Phys. Res. **A634** (2011) 25.

Structural study of functional materials and development of advanced methodology (BL08: SuperHRPD)

Y.Noda*, T.Kamiyama, S.Torii, J.Zhang, Y.Ishikawa, M.Yonemura, and T.Muroya

*Tohoku University, Aoba-ku, Sendai 980-8577, Japan
High Energy Accelerator Research Organization, Tokai-mura, Naka-gun 319-1106, Japan

After the recovery from the damage caused by the earthquake on March 11, 2011, we restarted the activities on BL08 SuperHRPD from April 2012. In the last report, the damage and reconstruction of BL08 were shown in detail [1]. The most difficult point had been the replacement of the broken mirror and the re-alignment of the beam-line to the experimental hatch. The BL08 building moved to the north by 3 cm and to the east by 5 cm and subsided by 9 cm at the expansion joint. The sample position of SuperHRPD moved to the north by 1.25 cm, to the east by 3.39 cm and subsided by 2.77 cm. In addition to the recovery process of the beam-line, we installed a new disk chopper with $^{10}B_4C$ in order to cut fast neutrons to reduce the background.

The first trial of the measurement and analysis using standard sample CeO_2 taken in April 2012 is shown in Fig. 1, in it we successfully performed the powder diffraction measurement and Rietveld analysis as we did before the earthquake. The intensity was also at the same level as before the earthquake damage. The upper panel of the figure shows the data taken at three different detector banks, backward bank, 90° bank and low-angle bank. Clearly, the hump in the background due to the scattering of unwanted fast neutrons is diminished and the background level is greatly improved. The lower panel shows the Rietveld analysis of the backward bank, and the fitting is satisfactory.

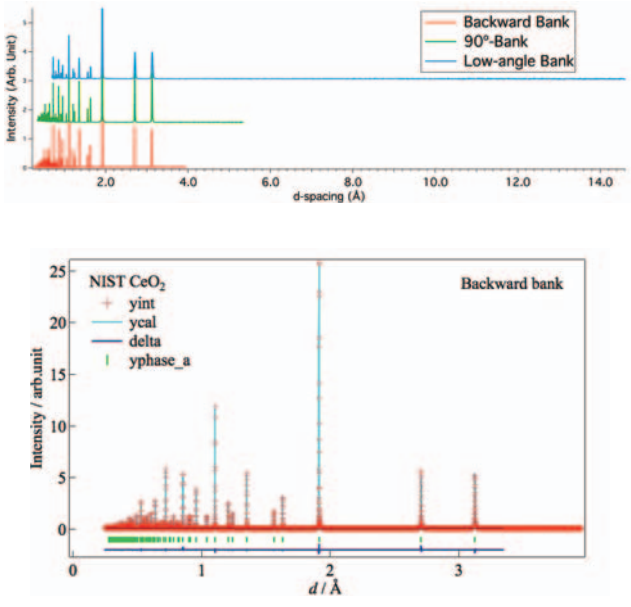

Fig. 1: First-trail of the measurement and Rietveld analysis of standard sample CeO_2 after the recovery of SuperHRPD.

One of the tasks of SuperHRPD is powder diffraction with super-high-resolution experiment and also application to a very complicated organic compound. We have progressed on several of these issues. Let us show the status of the resolution of SuperHRPD first. The resolution of the TOF method is simply expressed by the following equation:

$$(\Delta d/d)^2 = (\Delta t/t)^2 + (\Delta L/L)^2 + (\Delta\theta/\tan\theta)^2$$

Shown in Fig. 2 is the contribution of each term at BL08. Because of the long distance beam-line and the very short pulse shape at the source, the first two terms for $\Delta d/d$ are very small and it is possible to achieve the final goal of the designed resolution at SuperHRPD; $\Delta d/d = 0.035\%$. However, the current bottleneck is the third term, especially the resolution of the detector pixel size. Since we are still using the old detector reused from the ones at the Sirius diffractometer in KENS, the pixel size is about 12 mm, while the designed parameter for SuperHRPD is assumed to be 3

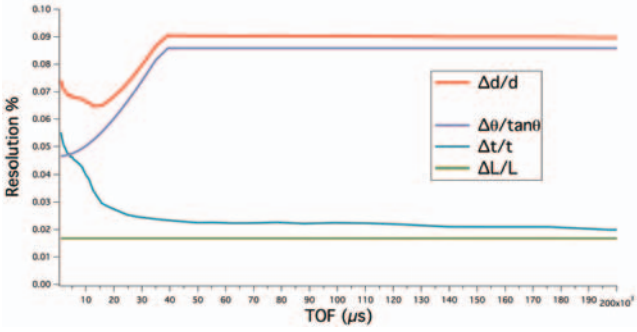

Fig. 2: Resolution of BL08 expressed by three different contributions and the total one. 2θ angle is assumed as 165°.

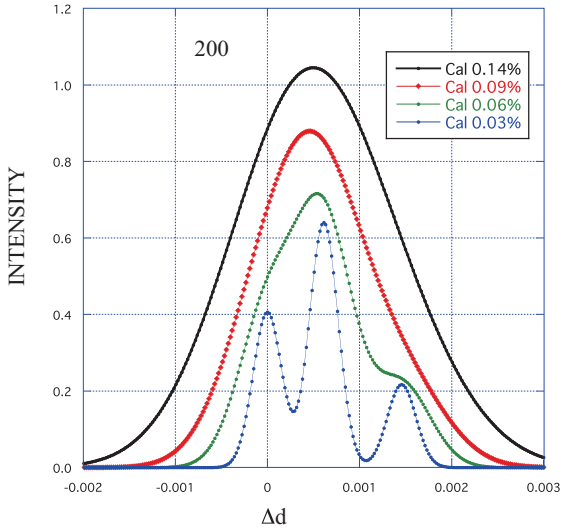

Fig. 3: Simulation of the splitting of the (200)c Bragg reflection at various instrumental resolution, by assuming the orthorhombic unit cell.

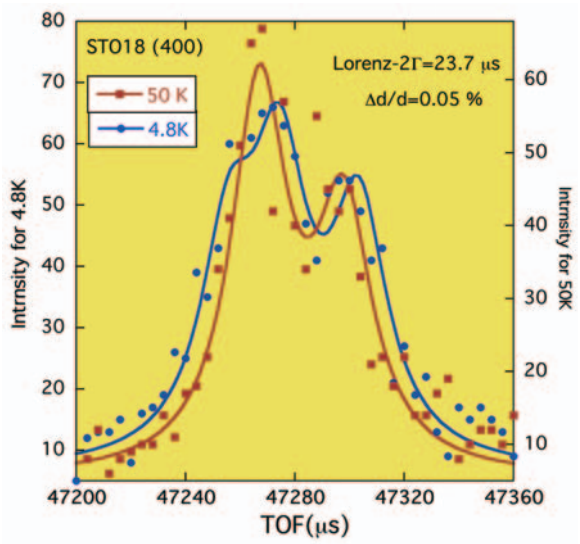

Fig. 4: Observed profile of (400)c Bragg reflection at 50 K (tetragonal phase) and at 4.8 K (ferroelectric phase). Data is accumulated only above 175° area.

mm in pixel size. Due to financial problems, the improvement of the detectors at BL08 is postponed so far, thus we have tried to get better resolution by using only very high angle area data to increase tanθ term in the equation. Figure 2 is calculated at 2θ=165°. The calculation tells us that almost all of the resolution at the present BL08 is coming from the detector pixel effect.

In order to overcome the resolution within the present condition, we measured the powder diffraction profile using a very high angle region, that is, higher than 175° in $SrTi^{18}O_3$. The purpose of the study is to pin down the space group of the ferroelectric phase and then the atomic displacement pattern to induce the polarization. $SrTiO_3$ is s special material among the well-known perovskite type structure because the so-called tolerance-factor is almost 1 in this compound so that soft-mode occurs not only at R and M points but also at Γ point. Not only that, but the distortion of the lattice is two order magnitude smaller than those in the other typical perovskite type materials. This is the reason why the structural study of the ferroelectric phase of $SrTi^{18}O_3$ has not been accomplished yet in the diffraction experiment. Only SuperHRPD has an ability or possibility to do this task. Figure 3 shows the simulation of the splitting of (200)c Bragg reflection upon the ferroelectric phase transition from tetragonal phase to orthorhombic phase. Note that the unit cell form at the ferroelectric phase is still unknown. If the model is correct as orthorhombic cell and the resolution is 0.035%, the final goal of SuperHRPD, the (200)c profile will change to three peaks shape. At least, when the resolution approaches 0.05%, we can expect the shoulder peaks of three-peak features.

Figure 4 shows the observed profile of (400)c Bragg reflection at 50 K (tetragonal phase) and at 4.8 K (ferroelectric phase). The data is accumulated only at the high angle area, larger than 175°. The resolution is estimated as 0.05%. At the tetragonal phase, we can see two peaks as is expected from the tetragonal symmetry. On the other hand, at 4.8 K it seems to split furthermore to three peaks. Thus, we can say that the unit cell is orthorhombic or less symmetrical. We have performed the Rietveld analysis using all the area data since the statics of the data at only the limited region more than 175° is too poor. Based on the conclusion as shown in Fig.4, we pin down the space group as F2 mm with the unit cell size 2a × 2b × 2c. The obtained atomic displacement pattern is the so-called Slater mode plus the anti-phase rotation of TiO_6 molecule.

In order to improve the resolution, we are planning to replace part of the existing position sensitive detectors (diameter of ϕ12.7) at a high angle region by new detectors with smaller diameter of ϕ8. Figure 5 shows the new detector, and when the present detectors are replaced with new ones, the resolution will be improved drastically, by 2/3 of the Δθ term.

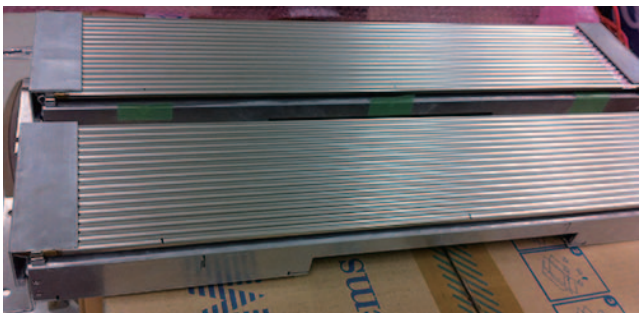

Fig. 5: New position sensitive detector for SuperHRPD. The diameter is ϕ8.

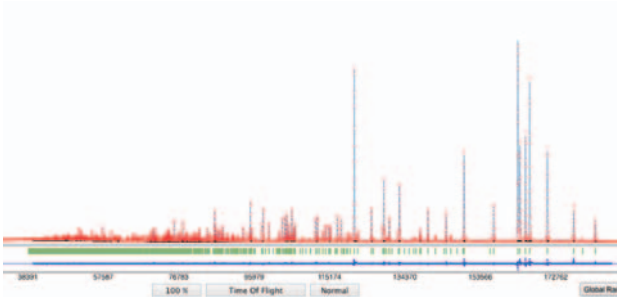

Fig. 6: Rietveld fitting of glycyl-glycine based on the $P2_1/c$ model.

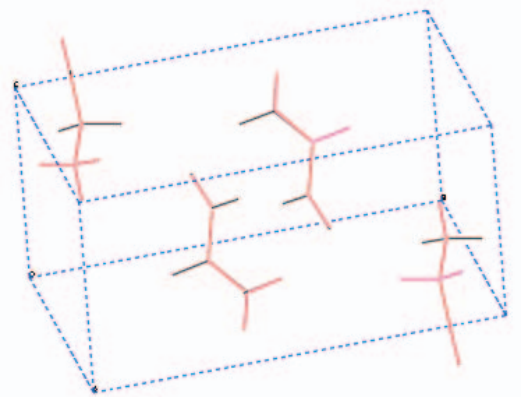

Fig. 7: Wire-frame drawings of α-glycine based on the present analysis with that in reference [2]. Two drawings completely overlap.

The next issue is the structure analysis of organic compounds. Under the increasing demand of structure science with complicated structures such as inorganic-organic composite materials, super molecule, pharmaceuticals, biomaterials, *etc.*, crystal structure analysis of several small molecules of amino acids and peptides such as glycine, alanine and glycyl-glycine, *etc.*, has been performed.

Figure 6 shows the Rietveld fitting of deuterated glycyl-glycine ($P2_1/c$, $a = 8.819$ Å, $b = 9.756$ Å, $c = 9.782$, $\beta = 104.30°$). The fitting was satisfactory. Figure 7 shows the crystal structure of deuterated α-glycine obtained from the present analysis together with that of hydrogenated α-glycine [2]. Because of the difference of H and D in the molecule, the lattice parameters are different but the obtained atomic coordinates are almost the same except the differences of H and D atoms. In the figure, the reported structure and the present result are simultaneously drawn and completely overlap. Details of the activity of organic materials on SuperHRPD will be reported separately.

References

[1] T. Kamiyama *et al.*, KENS report **XVIII** (2011) 23-26.

[2] Per-Gunnar Jonsson and Ake Kvick, Acta Cryst., B28, (1972)1827.

Fundamental Research of the Hydrogen Storage Mechanism with High-Intensity Total Diffractometer

T.Otomo[1], K.Suzuya[2], K.Ikeda[1], H.Ohshita[1], N.Kaneko[1], T.Seya[1], F.Fujisaki[1], T.Fukunaga[3], K.Mori[3], Y.Onodera[3], K.Itoh[4], Y.Kameda[5], T.Yamaguchi[6], K.Yoshida[6], K.Maruyama[7], Y.Kawakita[2], S.Shamoto[8], K.Kodama[8], S.Takata[2], S.Satoh[1], S.Muto[1], T.Ino[1], H.M.Shimizu[1], T.Kamiyama[1], and S.Ikeda[1]

[1]*Neutron Science Laboratory, High Energy Accelerator Research Organization (KEK), 1-1 Oho, Tsukuba, Ibaraki, 305-0801, Japan*
[2]**J-PARC center, Japan Atomic Energy Agency (JAEA), 2-4 Shirane Shirakata, Tokai-mura, Naka-gun, Ibaraki 319-1195, Japan*
[3]*Research Reactor Institute, Kyoto University, 2 Asashiro-Nishi, Kumatori-cho, Sennan-gun, Osaka 590-0494, Japan*
[4]*Graduate School of Education, Okayama University, 1-1-1 Tsushima-naka, Kita-ku, Okayama, Okayama 700-8530, Japan*
[5]*Faculty of Science, Yamagata University, Koshirakwa, Yamagata, Yamagata 990-8560, Japan*
[6]*Department of Chemistry, Fukuoka University, Nanakuma, Johnan, Fukuoka 814-0180, Japan*
[7]*Graduate School of Science and Technology, Niigata University, 8050 Igarashi, Nishi-ku, Niigata, Niigata 950-2181, Japan*
[8]*Quantum Beam Science Directorate, Japan Atomic Energy Agency (JAEA), 2-4 Shirane Shirakata, Tokai-mura, Naka-gun, Ibaraki 319-1195, Japan*

Brief over-view of NOVA in 2012

When in 2012 NOVA was opened for the general user program, a total of 5 experiments in 2012A and 20 ones in 2012B were performed on it.

Within the S-type project of NOVA, various experiments were performed: structure analysis of disordered $LiAl(ND_2)_4$ to investigate the hydrogen (ammonium) desorption process, nano-particle size estimation with PDF, void size distribution in amorphous Se by a structural modeling, structure of aqueous $LiNO_3$ solutions and so on.

The preliminary stages of the *in-situ* experiments with hydrogen gas atmosphere to test the background level of high-pressure cells were conducted successfully: we observed that the pair distribution function (PDF) of silicon with vanadium high-pressure cell designed for 10 MPa gas pressure was very similar to PDF of silicon with vanadium ambient pressure cell with a 0.1 mm thick wall. A "Levitation apparatus" to realize containerless experiments for liquid-amorphous transition was introduced. The upgrade of the neutron beam monitoring system (GEM) was started to prepare for the 1 MW operation of J-PARC.

Performance of NOVA – minimum sample amount

The background of NOVA was estimated as low as 1/100 of a vanadium sample cell (with 0.1 mm thickness). The minimum sample amount measured at NOVA was about 1 mg. The sample was $YLiFeH_6$, which was synthesized in a high-pressure condition (6 GPa and 600-800 Celsius degree) with size 0.8 mm in diameter and 0.2 mm in thickness. The Bragg peaks of the sample measured in 8 hrs were confirmed as F-43m as measured by X-ray as shown in Fig. 1. This result suggests that a background reduction for such a small sample should be considered in NOVA.

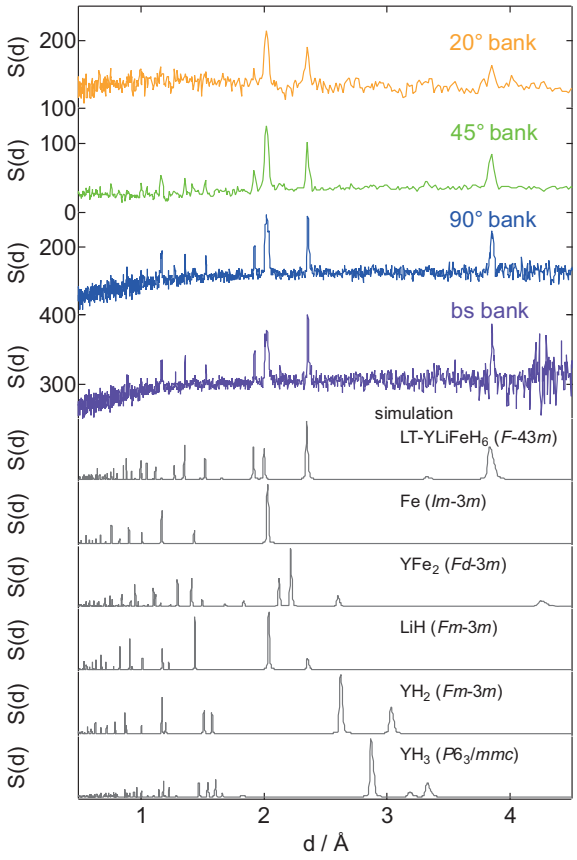

Fig. 1: Measured diffraction pattern of $YLiFeH_6$ on NOVA and simulated diffraction pattern.

Structure analysis of $LiAl(ND_2)_4$

$LiAl(ND_2)_4$, hereafter Li-Al-amide, stores hydrogen in the form of ammonia. At 100∼160 C, Li-Al-amide releases ammonia and the structure becomes amorphous.

$$LiAl(NH_2)_4 \rightarrow LiAl(NH)_2 + 2NH_3$$
$$\rightarrow 1/3Li_3AlN_2 + 2/3AlN + 8/3NH_3$$

It is essential to analyze the amorphization process in order to understand the reaction mechanism. Heat treated sample of deuterated Li-Al-amide as well as as-prepared one were measured on NOVA. The amounts of the samples were about 50 mg each.

A Reitveld refinement of the as-prepared sample was performed and its crystal structure parameters were refined. Other samples, heat treated at 160 C and 400 C, showed broad peaks and the Reitveld refinement was not feasible. Measured $S(Q)$ were depicted in Fig. 2.

The atomic pair correlation function, $G(r)$, doesn't show N-D correlation of Li_2ND (Fig. 3). This means that Li_2ND is not formed by the heat treatments. Then, it was assumed that $LiAl(NH)_2$ is not formed through the reaction.

$$(1\text{-}x)LiAl(NH_2)_4$$
$$\rightarrow x/3Li_3AlN_2 + 2x/3AlN + 8x/3NH_3$$

With the crystal structure parameters refined by the as-prepared sample, structural refinements of $G(r)$ were performed (Fig. 4). Formation of a network structure of AlN_4 was suggested since Al-N and N-N correlation becomes clearer in heat-treated samples. The network structure was also suggested by synchrotron X-ray measurements but it was the first time that the adequateness of the reaction without $LiAl(NH)_2$ was verified based on experimental results.

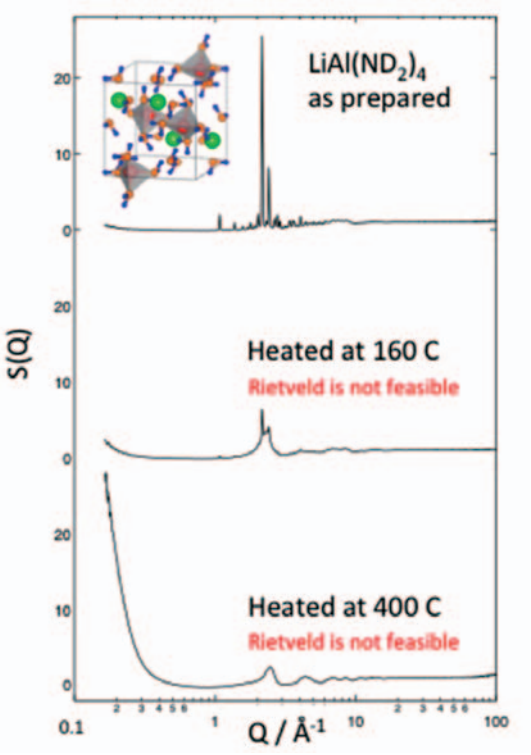

Fig. 2: Measured S(Q) of $LiAl(ND_2)_4$ on NOVA.

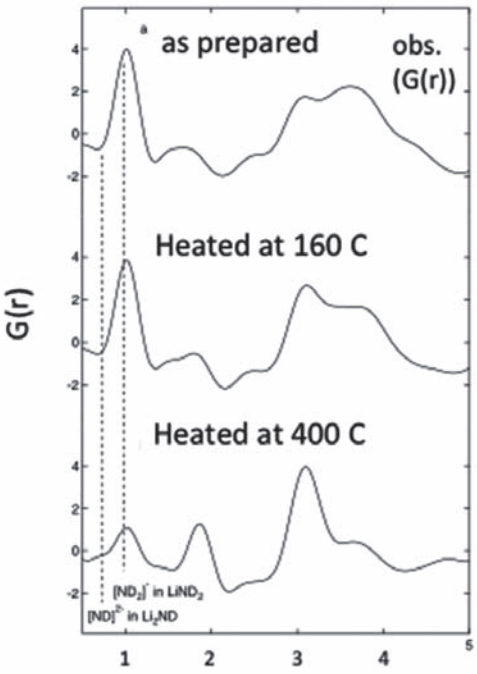

Fig. 3: Atomic pair correlation function, $G(r)$, of $LiAl(ND_2)_4$ obtained by Fourier transformation of $S(Q)$.

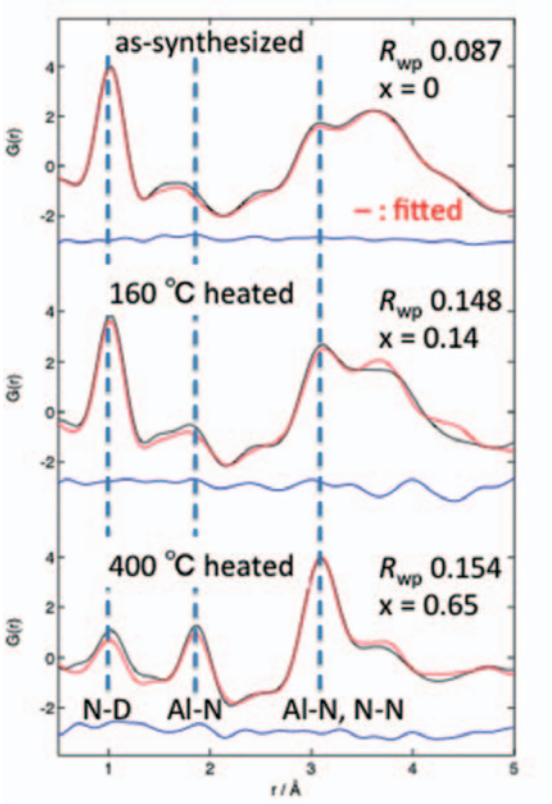

Fig. 4: Refinements of $G(r)$ of $LiAl(ND_2)_4$.

Size estimation of nano-particle size with PDF

Nano-particulation is often adopted to improve the reaction speed of the hydrogen storage materials. $G(r)$ of silicon powder shows that NOVA can observe atomic pair correlation of up to 200 Å without significant broadening or dump of peaks. In the case of nano-particles, since the particle size and the maximum atomic distances are comparable, dumping of intensity of $G(r)$ is more significant than bulk.

The dumping function of $G(r)$ of 90-deg bank of NOVA was fixed by a standard sample (Al_2O_3) and the diameter of the TiO_2 nano particle was successfully estimated as 7.3 nm. The shape was assumed to be spherical. This is consistent with the result of the micro-scope measurent.

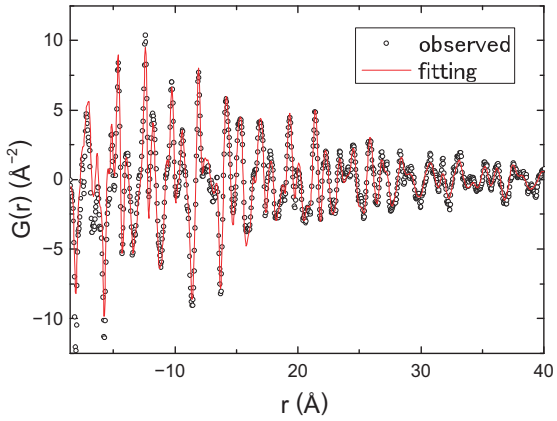

Fig. 5: $G(r)$ of TiO_2 nano-particle. Fitted with a spherical particle (diameter: 7.3 nm).

Void size distribution in amorphous Se by structural modeling

Void structure analysis is one of the key tools for hydrogen materials studies. The modeling of amorphous structure on void structure is important in various materials.

Figure 6 shows S(Q) of amorphous Se at ambient temperature measured by NOVA and liquid Se at 230 C and 500 C measured by HIT-II at KENS. Observed changes according to sample temperatures. A small hump observed at the foot of the third peak was the expected difference between the amorphous phase and liquid one.

Structural modeling based on these $S(Q)$ was performed by reverse Monte-Carlo method with 800 selenium atoms (Fig. 7). The void distributions were estimated with these models and it was found that the most common size of the void was about 2.2 Å. This size, smaller than liquid, could be interpreted through the spiral structure in the amorphous phase, which is similar to the crystalline one.

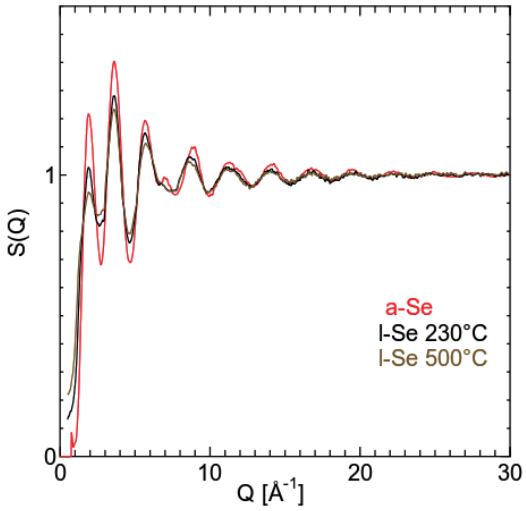

Fig. 6: $S(Q)$ of amorphous and liquid Se.

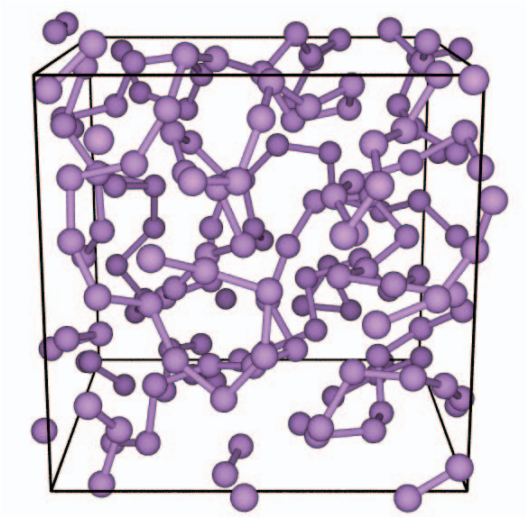

Fig. 7: Structural model of amorphous Se by revrese Monte-Carlo method.

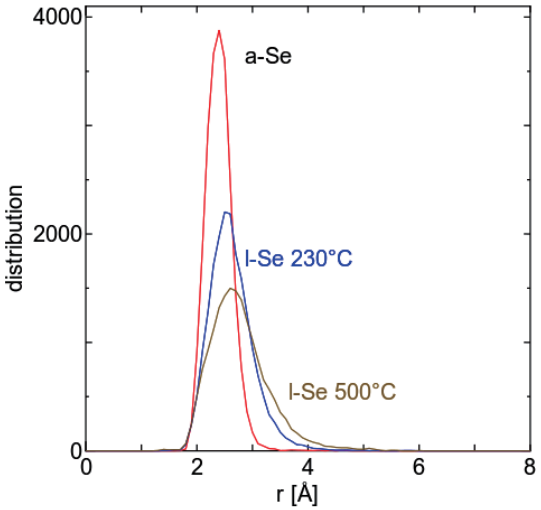

Fig. 8: Void diameter distribution in amorphous (a-Se) and liquid (l-Se) selenium.

Neutron diffraction study of the structure of aqueous $LiNO_3$ solutions

Despite the prolonged efforts, there are still some serious problems about determining the hydration structure of Li^+. The concentration dependence of the hydration number of Li^+ and the nearest neighbor $Li^{+\cdots}O$ with regard to distance seems still uncertain [1,2]. The neutron diffraction with $^6Li/^7Li$ isotopic substitution method is considered the most reliable experimental technique to determine the values of r_{LiO} and n_{LiO} because the observed difference function involves partial structure factors relating to Li-j atom pairs.

The first-order difference function, $\Delta_{Li}(Q)$ [3], is derived from the difference between the scattering cross sections observed for two solutions that are identical except for the scattering length of Li. The $\Delta_{Li}(Q)$ normalized for a stoichiometric unit, $(*LiNO_3)_x(D_2O)_{1-x}$, can be written as a linear combination of partial structure factors, $a_{Lij}(Q)$, involving contributions from the Li-j pair:

$$\Delta_{Li}(Q) = A[a_{LiO}(Q)\text{-}1] + B[a_{LiD}(Q)\text{-}1] + C[a_{LiN}(Q)\text{-}1] + D[a_{LiLi}(Q)\text{-}1]. \quad (1)$$

where, $A=2x(1+2x)(b_{6Li}-b_{7Li})b_O$, $B=4x(1-x)(b_{6Li}-b_{7Li})b_D$, $C=2x^2(b_{6Li}-b_{7Li})b_N$, and $D=x^2(b_{6Li}{}^2-b_{7Li}{}^2)$.

The first order difference function, $\Delta_{Li}(Q)$, observed for 1, 5 and 10 mol% $LiNO_3$ solutions is represented in Fig. 9. The structural parameters concerning the hydration shell of Li^+ were obtained through the least squares fitting procedure applying the following model function [4,5]:

$$\Delta_{Li}{}^{model}(Q)=\Sigma 2c_{Li}n_{Li\alpha}b_\alpha(b_{6Li}-b_{7Li}) \times \exp(-l_{Li\alpha}{}^2Q^2/2)\sin(Qr_{Li\alpha})/(Qr_{Li\alpha}) +4\pi\rho(A+B+C+D)\exp(-l_0{}^2Q^2/2) \times[Qr_0\cos(Qr_0)-\sin(Qr_0)]Q^{-3}+\gamma \quad (3)$$

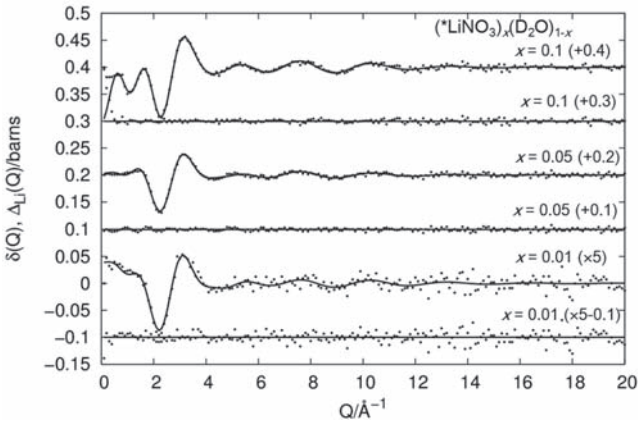

Fig. 9: The first-order difference function, $\Delta_{Li}(Q)$, observed for $(*LiNO_3)_x(D_2O)_{1-x}$ solutions, x = 0.1, 0.05 and 0.01.

where, c_{Li} and $n_{Li\alpha}$ are the number of Li^+ in the stoichiometric unit and the coordination number of α atom around Li^+, respectively. Parameters $l_{Li\alpha}$ and $r_{Li\alpha}$ denote the root-mean-square amplitude and the internuclear distance of the $Li^{+\cdots}\alpha$ pair, respectively. The long-range parameter, r_0, means the distance beyond which the continuous distribution of atoms around Li^+ can be assumed. The parameter, l_0, describes the sharpness of the boundary at r_0. A constant, γ, was introduced to adjust the center of the interference oscillation. Structural parameters $n_{Li\alpha}$, $l_{Li\alpha}$, $r_{Li\alpha}$, l_0, r_0 and γ are determined from the least squares fit to the observed $\Delta_{Li}(Q)$. The fitting procedure was performed in the range of $0.1 \le Q \le 20.0$ Å^{-1}. The nearest neighbor $Li^{+\cdots}O_W$ distance and coordination number determined for 10, 5 and 1 mol% $LiNO_3$ solutions are 1.97(1) Å and 4.1(1), 1.96(1) Å and 5.2(1), and 2.00(2) Å and 6.0(2), respectively. These results clearly indicate that the concentration dependence of the hydration number of Li^+ is actually present.

Upgrade of the neutron beam monitoring system

In preparation for the increment of the J-PARC beam power, we have developed a new electronics board for a Gas Electron Multiplier (GEM) [6] detector system (nGEM). nGEM has a compact body including the electronics, and is able to transfer data directly to a PC via network. The outline view of nGEM is shown in figure 1.

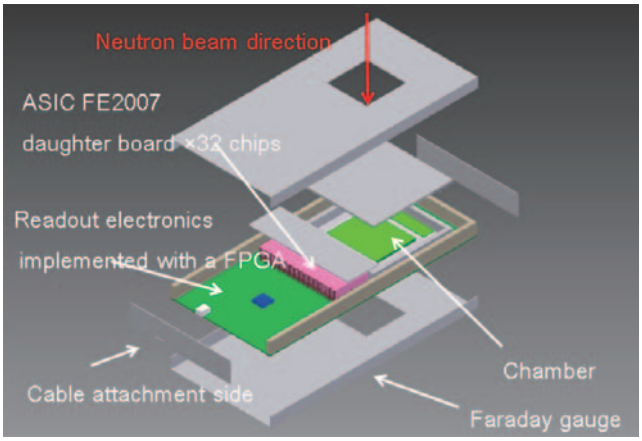

Fig. 10: The outline view of nGEM.

nGEM is an upgraded system of an existing neutron beam monitor [7] at NOVA. The upgrade points include detecting efficiency, time-slicing support and high-counting ability of the electronics. nGEM with thermal neutron efficiency from 0.1% to 1% is realized by exchanging an enriched-boron deposited aluminum cathode. Time-slicing of the event data is possible by encoded T0 information (proton injection timing signal) from a GATENET board [8]. When compared to

the existing neutron beam monitor in point of the detector performance, the data transfer capability of nGEM is 10 times larger than that of the existing system. Since the repetition of the electronics was changed from 100 MHz to 200 MHz, the recorded minimum time step was reduced from 10 ns to 5 ns. Besides, the algorithm of the event selection in the onboard electronics has been refined and we expect improvements of the high counting capability and the position resolution. The hit information such as Time-Of-Flight (TOF), hit position and pulse width is included in the data format of nGEM. The system information such as the amount of data loss is also included in the event data format. The system performance is analyzed by those data. The basic characteristics of nGEM are summarized in table 1.

Table 1: The basic characteristics of nGEM.

Neutron efficiency	0.1%∼1% for 1.8 Å
Data taking rate	Over 1 MHz
Position resolution	∼0.85 mm (FWHM)
Operation voltage	2600 V
Sensitive area	100 mm × 100 mm
Detector size	524 mm × 254 mm × 50 mm

The neutron irradiation test will be performed in May 2013 at the NOVA beam line and then installed on NOVA and SPICA.

Ackowlegdments

This work was partially supported by NEDO projects of “Advanced Fundamental Research Project on Hydrogen Storage Materials” (2007-2011) and “Research of Advanced Evaluation Technique of Hydrogen Storage Materials” (2012), JSPS KAKENHI Grant-in-Aid for Scientific Research (A)(24241034) and (B) (24310075), Grant-in-Aid for Young Scientists (A) (23686101, (B) (24710103).

References

[1] H. Ohtaki and T. Radnai, Chem. Rev. **93** (1993) 1157.
[2] P. R. Smirnov and V. N. Trosin, Russ. J. Gen. Chem. **76** (2006) 175.
[3] J. E. Enderby and G. W. Neilson, Water, A Comprehensive Treatise, Vol. 6, pp. 1-46, Plenum press, N. Y. (1979).
[4] A. H. Narten, M. D. Danford and H. A. Levy, Discuss. Faraday Soc. **43** (1967) 97.
[5] H. Ohtaki and N. Fukushima, J. Solution Chem. **21** (1992) 23.
[6] F. Sauli, Nucl. Instr. and Meth. A **386** (1997) 531.
[7] H. Ohshita, *et al.*, Nucl. Instr. and Meth. A **623** (2010) 126.
[8] S. Satoh, *et al.*, Development of a Trigger-Gate (GATENET) Module for Pulse Neutron Experiments, Presented at the TIPP 09.

Current status of the BL06 neutron guide system at J-PARC/ MLF for VIllage of Neutron ResOnance Spin Echo spectrometers (VIN ROSE)

M.Hino[1], T.Oda[2], N.L.Yamada[3], M.Kitaguchi[1*], H.Sagehashi[3], Y.Kawabata[1], and H.Seto[3]

[1]*Research Reactor Institute, Kyoto University, Kumatori, Osaka 590-0494, Japan*
[2]*Department of Nuclear Engineering, Kyoto University, Kyoto 615-8530, Japan*
[3]*Neutron Science Laboratory, High Energy Accelerator Research Organization (KEK), 1-1 Oho, Tsukuba, Ibaraki, 305-0801, Japan*
[*]*Present address: Center for Experimental Studies, KMI, Nagoya University, Nagoya, 464-8601, Japan*

Kyoto University and KEK started to construct a new beam line for neutron spin echo (NSE) spectrometers at the BL06 in the Materials and Life Science Facility (MLF) of the Japan Proton Accelerator Research Complex (J-PARC). The NSE method proposed by F. Mezei [1] is a powerful tool to investigate the slow dynamics of condensed matter. It directly measures the intermediate scattering function S(q,t) with very high neutron energy resolution. In order to cover a wide range of energy and momentum transfer with various sample environments, two types of NSE spectrometers will be installed in BL06: NRSE (Neutron Resonance Spin Echo) [2, 3] and MIEZE (Modulated Intensity by Zero Effort) [4]. NRSE is suitable to study slow dynamics of soft condensed matter with high energy resolution. MIEZE has a big advantage in flexible sample environments with the potential to open new fields of study. Thus we named them "VIN ROSE" (Village of Neutron Resonance Spin Echo Spectrometers) [5].

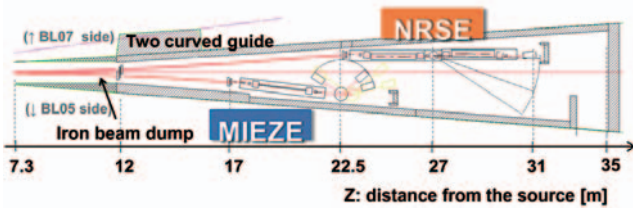

Fig. 1: Schematic top view of MIEZE and NRSE beam line at BL06 at J-PARC/MLF.

Figure 1 shows schematic top view of the BL06 beam line. There are two curved supermirror guide tubes for each spectrometer. The BL06 experimental space is also very limited, so the role of these curved guides is to create experimental space only for two spectrometers and a transport optimized neutron beam. By using curved guide tube, fast neutrons and gamma rays from the source are stopped by an iron beam dump. Before the construction, it was necessary to estimate the radiation shielding performance and the result had to fulfill the legal requirements and the rules of MLF concerning the prevention of radiation hazards. The limit value of dose rate is 12.5 μSv/h in the areas where experimenters can enter during beam operation [6]. In the VIN ROSE, the neutron optical devices are a key component and there are many devices in the spectrometers. We have to develop and improve step by step some of the key devices, such as the focusing mirror and related devices. It is not effective to calculate the shielding design with the fully-equipped spectrometer in this commissioning phase. It is important to make sure that the commissioning phase is more secure and the components easy to adjust.

Figure 2 (a) and (b) show the geometry of the calculation of PHITS (Particle and Heavy Ion Transport code System), a Monte Carlo simulation code [7,8,9] and the representative evaluation points to judge the dose level. The letter z indicates the distance from the source, and the center of the source duct is at the position of x=0, y=0. The straight neutron guide tubes will be installed inside the shutter (z=2.3-4.2 m) and the biological shielding (z=4.3-7.2 m). The neutron beam cross section is 93 mm^2 and m=2 supermirrors are used. Here, the number of m indicates the unit of the critical momentum transfer of natural nickel. The spallation neutron source of MLF produces neutrons in very wide energy region up to 1 GeV. Fast neutrons cause high dose rate and require space-occupying massive shielding. In order to stop such fast neutrons and gamma rays from the source and transport an optimized slow neutron beam for MIEZE and NRSE spectrometers, we installed two curved neutron guides from z=7.3 to z=17.1 m and an iron beam dump between the branches inside the iron pre-shield (z=7.2-12 m). The curvature radii of both guides are 140 m. The disk choppers are installed to the gap area (z=12.0-12.3 m) to selected wavelength band. It is very important for

the high resolution measurement to transport slower neutrons since the energy resolution of the NSE method is proportional to the third power of incident neutron wavelength. The high resolution NRSE uses a pinhole beam with a wide divergent angle by employing a pair of ellipsoidal focusing mirrors [10, 11]. The NRSE guide has elliptical focusing shapes in the vertical direction (z=7.3-22.7 m) and in the horizontal direction of the last guide part (z=17.3-22.7 m).

All the supermirrors for these guides are deposited on silicon wafers with thickness of 3 mm by using the ion beam sputtering machine at KURRI(KUR-IBS) [5, 12]. The supermirrors are held precisely and covered by iron shields to reduce the dose level. The NRSE and MIEZE guides use m=2.5 and 3 supermirrors, respectively. These reflectivities were measured mainly with the BL16 (SOFIA) reflectometer at J-PARC/MLF. Most of the supermirrors have been measured and the average performance was high. Figure 3 shows typical reflectivities of a supermirror for the MIEZE and NRSE guides.

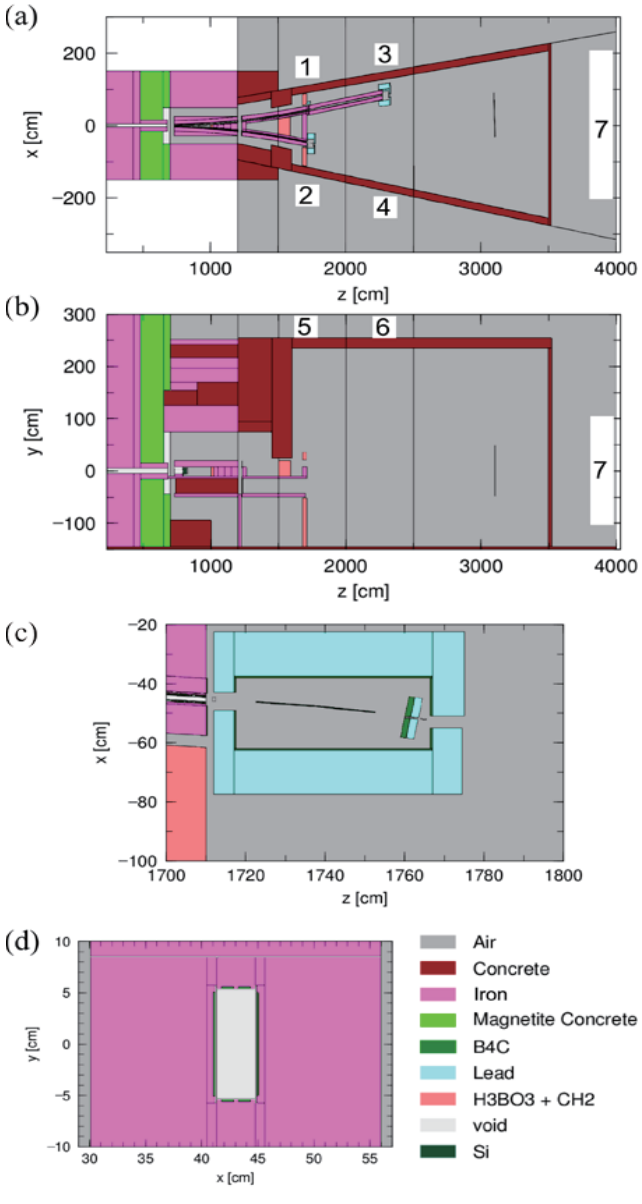

Fig. 2: BL06 shielding geometry of PHITS calculation and evaluation points in (a) horizontal (xz plane) and (b) vertical (yz plane) views. (c) Polarizing mirror and beam slit housing structure of the MIEZE spectrometer. (d) Typical cross-sectional view of the NRSE guide. The numbered positions are the evaluation points of the dose rate.

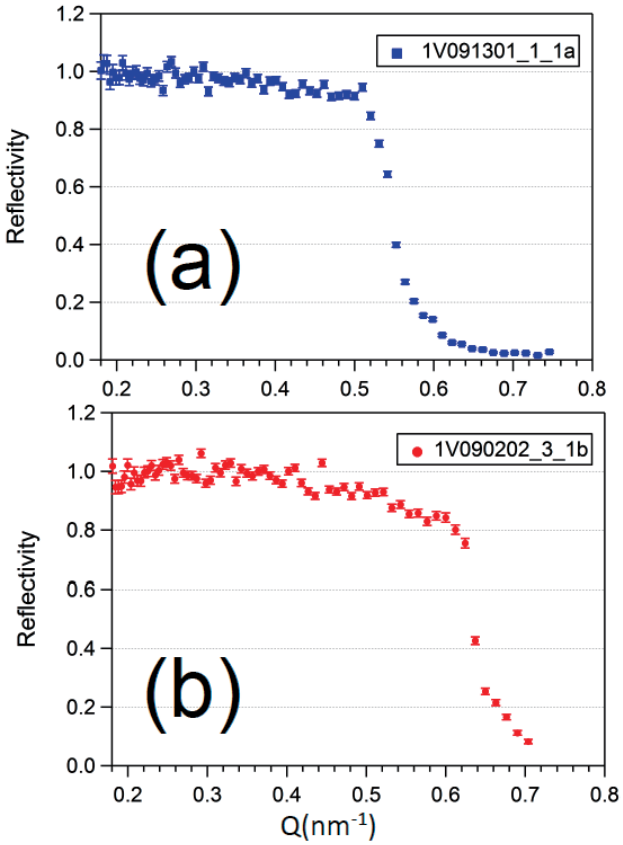

Fig. 3: Reflectivity of a typical m=2.5 and 3 supermirror for (a) NRSE and (b) MIEZE spectrometer, respectively.

We have already constructed upstream concrete shielding (z=12-16 m) and installed it to the BL06 as shown in Fig. 4. Polarizing mirrors and beam slits were installed to the exits of the guide of NRSE and MIEZE as required neutron optical devices in the commissioning phase. The mirror and silts housing consists of 50 wt% B4C-containing rubber and lead to stop scattered neutrons and gamma rays as shown in Figure 2 (c). The Beam stoppers for MIEZE and NRSE made of B4C rubber and lead were set at the beam end positions of z=25 m and z=31 m, respectively. These positions are the same as the fully-equipped setup we plan to build in the future. The thickness of the B4C rubber and lead were 5 mm and 3 cm respectively. Figure 2 (d) shows the cross-section

Fig. 4: Photograph of the upstream concrete shielding installed to BL06 at J-PARC/MLF.

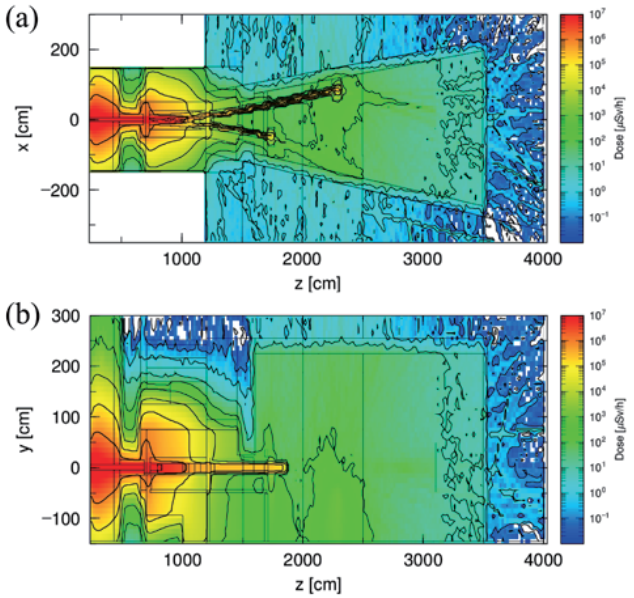

Fig. 5: Total (neutron + photon) dose rate map in (a) horizontal (xz plane) and (b) vertical (yz plane) views.

of the supermirror guide covered by iron shield.

The neutron intensity at each guide exit was estimated to be about 2×10^8 n/cm^2/s/Å at the 1 MW operation. The wavelengths of the maximum intensity were 3.5 Å and 5.2 Å, respectively. The dose level in the experimental hall at MLF was calculated with three points of concrete thicknesses, 10, 20 and 30 cm, for side and ceiling part from z=16 to z=35 m. We changed the thickness only for the side and the ceiling part and kept 30 cm thickness of the backmost concrete wall (z=35 m) to compare with the limit dose rate (12.5 μSv/h) in the MLF experimental hall. The thickness of the backmost concrete wall was changed by 50 cm to achieve a suppressed level of dose rate as low as possible outside of the experimental hall.

Figure 5 illustrates the two-dimensional distribution of radiation dose rate converted from neutron and photon flux in the setup for commissioning. Table 1 shows the dose rate values at the evaluation positions shown in Figure 2 (a) and (b). They indicate that 10 cm concrete thickness is not enough but 20 cm thickness is acceptable for regulation of the MLF experimental hall.

We also calculated the dose rates with backmost concrete wall (z=35 m) with thickness of 40 cm and 50 cm. The dose rates for thickness of 30, 40 and 50 cm outside of the experimental hall (the position No.7) were estimated to be 0.2±0.3, 0.06±0.3, and 0.07±0.2 μSv/h, respectively. These values were calculated by averaging dose rates of mesh points (10 cm×10 cm in the xz plane) over the xyz space (x=-200-200 cm, y=-50-50 cm, z=3800-3900 cm), in which the volume was 4 m^3. The variance of the mesh points was of the order of 0.1μSv/h and this large variance came from a photon dose. We found that 20 cm concrete thickness

Table 1: Calculated dose rates [μSv/h] for variety of thickness of the side and ceiling concrete shield at the evaluation points as shown in Fig 2(a) and (b).

Position of evaluation	Concrete 10 cm	Concrete 20 cm	Concrete 30 cm
No. 1	4.9	2.3	1.4
No. 2	6.6	3.5	2.0
No. 3	15.6	10.3	5.8
No. 4	12.5	7.9	4.1
No. 5	7.1	6.4	3.9
No. 6	24.2	8.1	2.9

was acceptable but 30 cm provided more safety in the side and ceiling part. We also investigated the dose level outside the experimental hall as a function of the backmost concrete thickness. This shielding design was dedicated for the commissioning phase. After the commissioning, most parts of the beam line should be covered by neutron mirrors with vacuum flight paths to reduce the nimber of neutrons scattered by the air. It also reduces the dose rates and furthermore, in NRSE, we will use a smaller beam size after the polarizing mirror. Thus we expect that the dose rate in the future will be smaller than that of the present shielding geometry.

In FY2012, we designed the details and purchased the BL06 downstream (z=16-35 m) concrete shielding. We finished succeefully the fabrication of all mirrors for those guides in which the total length is about 29 m. During this manufacturing process, we got a lot of experience and established better fabrication conditions

for a large scale neutron supermirror with high reflectivity for a real neutron guide.

We are going to install the neutron guide and all the shielding to observe the MIEZE signal in FY2013.

Reference

[1] F.Mezei, Z.Phys 255 (1972) 146.
[2] R. Golub and R. Gähler, Z. Phys.B 65 (1987) 43.
[3] R. Gähler, R. Golub, Z. Phys.B 65 (1987) 287.
[4] R. Gähler, R. Golub and T. Keller, Physica B 180-181 (1992) 899.
[5] M.Hino, T.Oda, M.Kitaguch, N.L.Yamada, H.Sagehashi, Y.Kawabata, H.Seto, Physics Procedia 42 (2013) 136.
[6] M. Harada, K. Oikawa, Y. Kasugai and F. Maekawa, Prog. Nucl. Sci,. Technol. 1 (2011) 94.
[7] H.Iwase, K.Niita and T.Nakamura. J. Nucl. Sci.Technol., 39 (2002) 1142.
[8] K. Niita, N. Matsuda, Y. Iwamoto, H. Iwase, T. Sato, H. Nakashima, Y. Sakamoto and L. Sihver, "PHITS: Particle and Heavy Ion Transport code System, Version 2.23", JAEA-Data/Code 2010-022 (2010).
[9] T.Oda, M.Hino, M.Kitaguch, N.L.Yamada, H.Sagehashi, Y.Kawabata and H.Seto, PNST, in press.
[10] M. Bleuel, F. Demmel, R. Gähler, R. Golub, K. Habicht, T. Keller, S. Klimko, I. Köper, S. Longeville, S. Prokudaylo, Lecture Notes in Physics, 601 (2003) 176.
[11] T.Oda, M.Hino, M.Kitaguch, Y.Kawabata, Physics Procedia, 42 (2013) 121.
[12] M.Hino, H.Sunohara, Y.Yoshimura, R.Maruyama, S.Tasaki, H.Yoshino and Y.Kawabata., Nucl. Inst. Meth. A 529 (2004) 54.

Structural Analysis of Nano Interface of Functional Soft Matter Using Neutron Reflectometer at BL16 in J-PARC/MLF

M.Kobayashi[1], N.L.Yamada[2], N.Torikai[3], H.Sagehashi[2], S.Sato[2], H.Seto[2], M.Furusaka[4] M.Hino[5], T.Fujiwara[6], H.Takahashi[7], H.Arita[2], H.Jinnai[1], H.Ogawa[8], T.Xia[9], R.Inoue[9], T.Kanaya[9], K.Nishida[9], M.Inutsuka[10], K.Ito[10], H.Yokoyama[10], T.Hirata[11], H.Matsuno[11], M.Tanaka[12], K.Tanaka[11], K.Azuma[3], Y.Kamata[3,13], and A.Takahara[1,2,14]

[1]*Japan Science and Technology Agency (JST), ERATO, Takahara Soft Interface Project*
[2]*Neutron Science Laboratory, KEK, Tsukuba, Ibaraki, Japan*
[3]*Graduate School of Engineering, Mie University, Tsu, Mie, Japan*
[4]*Department of Quantum Science and Engineering, Hokkaido University, Sapporo, Japan*
[5]*Research Reactor Institute, Kyoto University, Kumatori, Osaka, Japan*
[6]*Nuclear Professional School, The University of Tokyo, Tokyo, Japan*
[7]*Department of Nuclear Engineering and Management, The University of Tokyo, Tokyo, Japan*
[8]*Japan Synchrotron Research Institute, Sayo-gun, Hyogo, Japan*
[9]*Institute for Chemical Research, Kyoto University, Gokasho, Uji, Kyoto, Japan*
[10]*Department of Advanced Materials Science, University of Tokyo, Chiba, Japan*
[11]*Department of Applied Chemistry, Kyushu University, Fukuoka, Japan*
[12]*Department of Biochemical Engineering, Yamagata University, Yonezawa, Japan*
[13]*Kurashiki Research Center, Kuraray Co., Ltd, Kurashiki, Okayama*
[14]*Department of Engineering, Kyushu University, Fukuoka, Japan*

1. Instrumentation

1.1 Upgrade history and current status

Neutron reflectometry (NR) is very useful for investigations on structures of surfaces and buried interfaces composed of soft materials. A beam line (BL) 16 in J-PARC/MLF is dedicated for a horizontal type neutron reflectometer. At BL16, two downward neutron beams (2.22° and 5.71°) are transported from a coupled hydrogen moderator to irradiate a free surface such as air-water interface. In order to realize neutron reflectivity measurement with a high flux neutron beam at J-PARC/MLF as early as possible, we started to accept the neutron beam with "ARISA-II" reflectometer relocated from KENS facility in 2008 [1]. However, the motion range of the slits, sample and detector stages were so short that only the 2.22° beam line at BL16 was used, because the components of ARISA were not designed for this beam line. This is a serious disadvantage in an air-liquid interface measurement when it is necessary to observe a high-q region with a high incident angle. To overcome this problem, ARISA-II was replaced in 2011 with the brand-new reflectometer " SOFIA (SOFt-Interface Analyzer)" through the collaboration between JST/ERATO and KEK [2, 3]. Figure 1 shows a schematic drawing of SOFIA in the

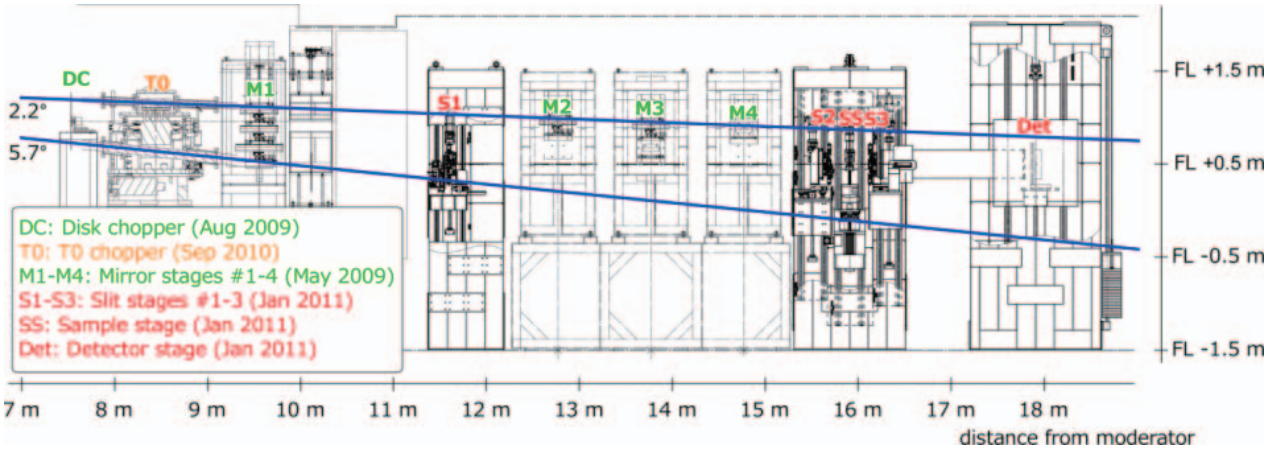

Fig. 1: Side view of SOFIA reflectometer placed at BL16 in J-PARC/MLF.

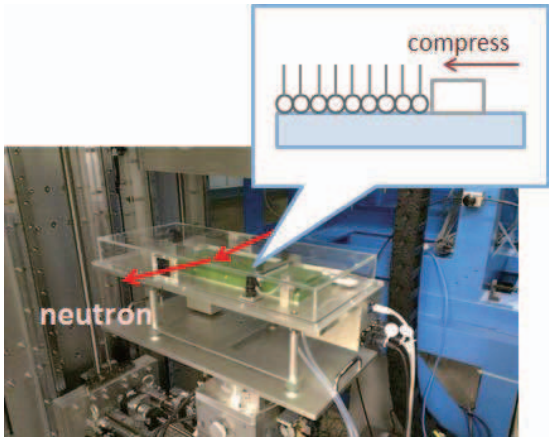

Fig. 2: New Langmuir trough to make a monolayer on a free water surface for neutron reflectivity measurement.

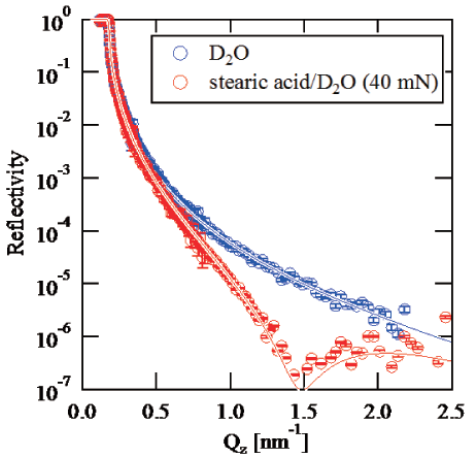

Fig. 3: Neutron reflectivity profiles from air/heavy water interface and from air/stearic acid/heavy water interface.

experimental hutch. With the new slit, sample, and detector stages, we can accept both the 5.71° and 2.22° beam lines. This enables us to measure NR over wide scattering vector (q) region on free liquid surfaces. Also, the slit system can finely collimate to irradiate an area of 10 mm square, a typical sample size for synchrotron light sources, with an angular resolution of 3%.

The regulation on how to treat liquid samples was, however, very strict and did not allow measuring air-liquid interface at J-PARC/MLF. This year, this regulation was drastically relaxed and the air-liquid interface measurement is permitted. For this measurement, we installed a new Langmuir trough to make a monolayer on a free water surface (Fig. 2). The result of the test measurement shows that a clear fringe originated from a partially deuterated stearic acid monolayer (Fig. 3). Thanks to the high flux beam of J-PARC/MLF, only 30 minutes is enough to take good statistics, which is 10 times less than that of KEK-PS. The background

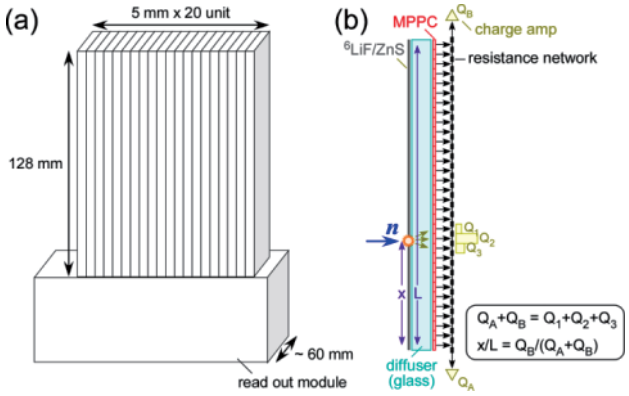

Fig. 4: Schematic illustration of the new detector. (a) dimension of the 1D-detector array. (b) side view of each 1D-detector.

level is, however, still high due to neutrons hitting at the trough. To solve this problem, we are developing a neutron absorber for suppressing the background.

1.2 Data acquisition system

We currently use a 2-dimensional photo-multiplier tube with a ^{6}LiF/ZnS scintillator as a neutron detector. Thanks to this detector, we can measure specular reflection, off-specular reflection, and background at a time. The neutron signals were taken with a NeuNET module and stored as event data with time stamps inserted by a GateNET module. Thanks to this recording system, we can arbitrarily change the binning of time-slicing for kinetics measurement. In addition, double frame mode (12.5 Hz operation) is available to extend the wavelength band by up to 1.76 nm, whereas 0.88 nm is the maximum wavelength in the single frame mode (25 Hz operation). The equipment enables us to perform kinetics measurement very efficiently, and this is a remarkable feature of SOFIA.

The detector, however, starts pulse pileup at around 10k counts per second because of the afterglow of the scintillator. Since the minimum accumulation time is limited by the count rate, this would be a problem for the time-slicing measurement especially when J-PARC is upgraded to be 1 MW. In order to increase the count rate, we have been developing a new photon detector with an opto-semiconductor device, multi-pixel photon counter (MPPC), in collaboration with the KENS-DAQ group.

Figure 4(a) schematically illustrates a new detector consisting of twenty 1-dimensional detectors and a read out module. The sensitive area of each detector is 5 mm in width and 128 mm in length, and tothe total for all will be 100 mm × 128 mm. Since the neutron beam for reflectivity measurement is collimated in one dimension but is very wide in the other dimension, the neutron counts for a detector can be reduced by sepa-

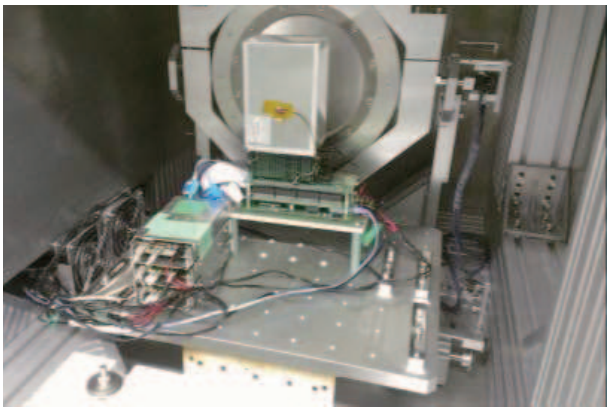

Fig. 5: Picture of the detector installed at the detector position of SOFIA from down-stream side.

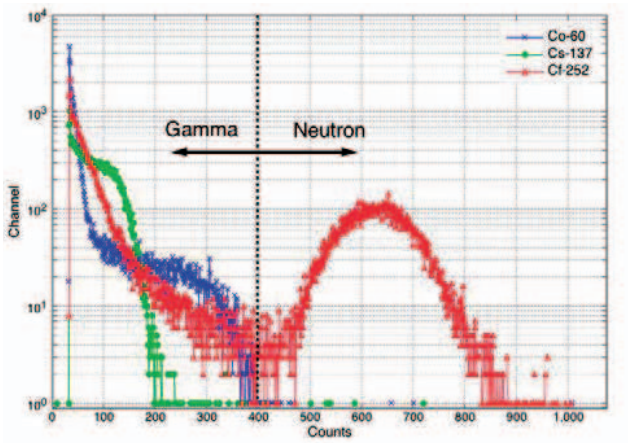

Fig. 6: Pulse height spectrum obtained with 2 mm thick Ce: LiCAF crystal and PMT, irradiated with Cf-252 neutron source and ^{60}Co, ^{137}Cs gamma-ray source.

rating a 2-dimensional detector into an array of 1-dimensional detectors. Figure 4(b) shows the side view of the detector. The position of a neutron in length direction is evaluated by a charge division method, and the spatial resolution is designed to be about 1 mm. Since the development of this detector has been almost finished last year, we tried to measure reflectivity using the new detector.

Figure 5 shows the picture of the new detector installed at the detector position of SOFIA. The detector is fully surrounded by neutron shields for background reduction. Although the detailed analysis has not been finished yet, reflectivity measurement was successfully done. The temperature of the detector, however, increased by 2.5°C due to the heat from the analog-digital convertors, even though the detector and cable duct were equipped with fans for cooling and air-exchange, respectively. This may become a problem for the measurement because the gain of MPPC strongly depends on the temperature.

1.3 New Ce:LiCAF fast single crystal neutron scintillator

Helium-3 (^{3}He) is the most widely used isotope for neutron detection. It has a high absorption cross section for thermal neutron beams and is used as a converter gas in neutron detectors. However, the worldwide shortage of ^{3}He following the drawdown in nuclear weapons production since the Cold War has some extent prevented the neutron detector development. Therefore, a ^{3}He alternative detector is strongly required. For a ^{3}He alternative detector, LiF/ZnS is one of the most commonly used scintillator for neutron detection. Its characteristics such as availability, ability to make a large size crystal, and its brightness (amount of light yield per neutron) become a first choice in various situations. However, the issues are low detection efficiency and count rate capability. The former is due to its opaqueness and the latter due to its very slow decay time (up to ∼100 μs). As the neutron intensity becomes higher, the demand for a high counting rate detector becomes stronger.

The Ce:LiCaAlF$_6$ (Ce: LiCAF) scintillator [4-6] is a strong candidate for an alternative to ^{3}He-based gaseous neutron detectors because it has a great detection efficiency for neutrons as well as fast decay time (40 ns). Since its effective atomic number (Z_{eff}) is very small, its sensitivity to gamma rays is very low. Therefore, this new scintillator has an ability to discriminate neutrons from gamma rays only with the signal pulse height. In addition, its fast decay time enables Here, we report our neutron response study applying a Ce: LiCAF scintillation detector for pulsed neutron sources, such as J-PARC.

We have tested our Ce:LiCAF scintillation neutron detector with a ^{252}Cf neutron source and a ^{60}Co gamma-ray source to evaluate neutron and gamma-ray efficiencies. A 10×10×2 mm^3 sized crystal was used for this initial test, and the crystal is coupled with a photomultiplier tube (PMT) (Hamamatsu R329) with optical grease (OKEN 6262A). As shown in Fig. 6, the pulse height spectrum of the neutron beam acquired from Ce:LiCAF coupled with PMT shows that Ce:LiCAF's α/β ratio is high enough to discriminate gamma-rays (^{60}Co: 1.33 MeV, 1.17 MeV and ^{137}Cs: 662 keV) and neutrons with pulse height. Encouraged by the experimental result with radioisotopes, we tested our Ce:LiCAF scintillation detector at SOFIA. In this experiment, we made a comparison between a Ce:LiCAF scintillator (2 mm thick) and a conventional Li-Glass scintillator (1 mm thick). The aim of this experiment was to investigate the gamma-ray sensitivities at an accelerator-based neutron source.

Figure 7 shows the pulse height spectrum of gamma-rays mixed with neutrons achieved with 0.5 mm, 1 mm, and 2 mm thick Ce:LiCAF crystals. As the crystal becomes thinner, the region of Compton edge shifts to a lower energy region. When the thickness is 0.5

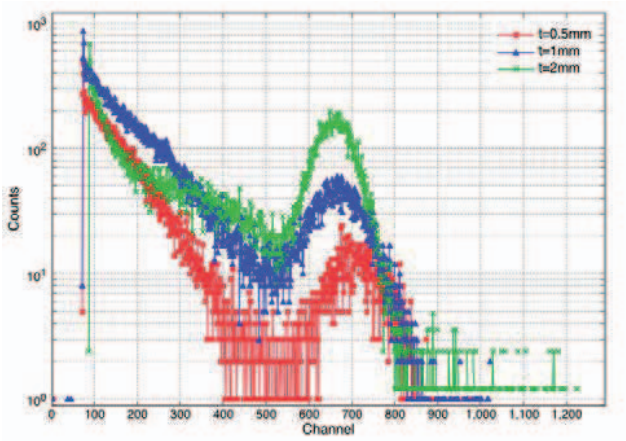

Fig. 7: Pulse height spectrum of gamma-ray and neutron mixed field. Neutron response of various thickness Ce: LiCAF crystals are shown: 2 mm, 1 mm and 0.5 mm.

mm, the pulse height region of gamma-rays and neutrons are clearly separated. However, with the 0.5 mm thick crystal, neutron detection efficiency decreased to 24% at 1.8 to 3.6 Å wavelength neutrons. In other words, the gamma-rays discrimination and the neutron detection efficiency is a trade-off. Therefore, depending on the beamline setup and the neutron instrument at a neutron facility, the thickness of the crystal should be carefully selected.

From this result, the energy deposited to the scintillator from gamma-rays at BL-16 can be estimated as 2.2 MeV from the spectrum. With Li-Glass scintillator, the peak channel of neutron is totally overlapped with the channel of Compton edge of gamma rays at BL-16. However, with the Ce: LiCAF scintillator, the gamma-ray component is not completely overlapped with the neutron peak. According to the previous study, 2 mm thick LiCAF scintillators can achieve more than 92% detection efficiency (thermal neutron). Therefore, even if we discard the gamma-ray overlapped channels, we estimate that Ce: LiCAF can still achieve about 50% detection efficiency for thermal neutrons.

2. Scientific topics

2.1 Chain-mixing at interface between polystyrene brush and free polystyrene matrix

When a polymer is placed on top of a polymer brush of same species, intermixing of polymer chains may occur at the interface between them. The fundamental knowledge of such inter-diffusion of the free polymer into polymer brush promotes deeper understanding of the adhesive property of materials with the bilayer brush/ free polymer type film as a "bonding" layer [7]. The self-consistent field (SCF) theory has been utilized to simulate such chain-mixing at the interface, in which the theory assumes uniform polymer brush chain length [8]. The coverage (σ, proportional to graft density), degrees of polymerization of the brush (N) and that of the free polymer (P) are important in such theoretical consideration [9, 10]. In general, when σ and P are sufficiently high ($N^{1/2} > 1$ if $N < P$, $N^{1/2} > (P/N)^{-1/2}$ if $N > P$), interfacial diffusion of the free chains into polymer brush hardly occurs due to the entropic penalty in the mixing, which is called "dry-brush" state.

Although the SCF theory neglects that issue, the effect of polydispersity of molecular weight in the polymer brush on interfacial mixing should be substantial. In this study, we investigated the time evolution of interfacial structure between deuterated polystyrene (dPS) layer and hydrogenated polystyrene (hPS) brush above a glass transition temperature (T_g) by neutron reflectivity (NR), and clarified the influence of the molecular weight dispersity of the brush, if any, on the interfacial thickness [11].

The h-PS brush ($N = 1423$, $\sigma = 0.22$, and $M_w/M_n = 1.83$) was prepared by surface-initiated atom transfer polymerization (SI-ATRP) on silicon wafer. The hPS brush was covered with a dPS layer ($P = 344$ and $M_w/M_n = 1.07$) via the floating method to fabricate hPS brush/ dPS bilayer [12]. The NR experiments were performed on SOFIA reflectometer installed in BL16 at MLF (J-PARC, Japan). We carried out an "anneal-quench" procedure: the bilayer film was heated at 393 K (above T_g) for a given time and then rapidly quenched to room temperature. The solidified sample was then observed by NR.

Figure 8 shows the (a) NR curves and (b) the corresponding volume fraction profiles at the interface between hPS and dPS before and after the annealing at 393 K for 30 min. In Fig. 8(a), the hPS brush/dPS bilayer film without the thermal annealing showed well-defined fringes in a q range of 0.15 - 1.0 nm^{-1} (q is the neutron momentum trasfer vector). The fringes arise due to the film thickness and sharp interface between the hPS and dPS layer. In contrast, the fringes in NR curve after the annealing at 393 K became blurred, as shown by curve (a2) in Fig. 8(a), particularly at higher q range. This is because inter-mixing between the hPS brush and bulk dPS took place during the thermal annealing. As shown in Fig. 8, the sharp interface (b1) between the hPS and dPS became much broader after the annealing (line b2). We note that any morphological changes, such as the dewetting behavior of the outer dPS layer, did not occur based on the atomic force microscopy images of the bilayer samples after the annealing.

Considering the combinations of P, N and σ values of this hPS brush and free dPS, the brush should theoretically be in a "dry brush" state. Therefore, the interfacial diffusion of the free polymer chains into polymer brush should not occur. In reality, however, the interfacial mixing of the d-PS free chain and the h-PS brush chains did happen. Such intermixing phenomena could be caused by the heterogeneity of the brush chain

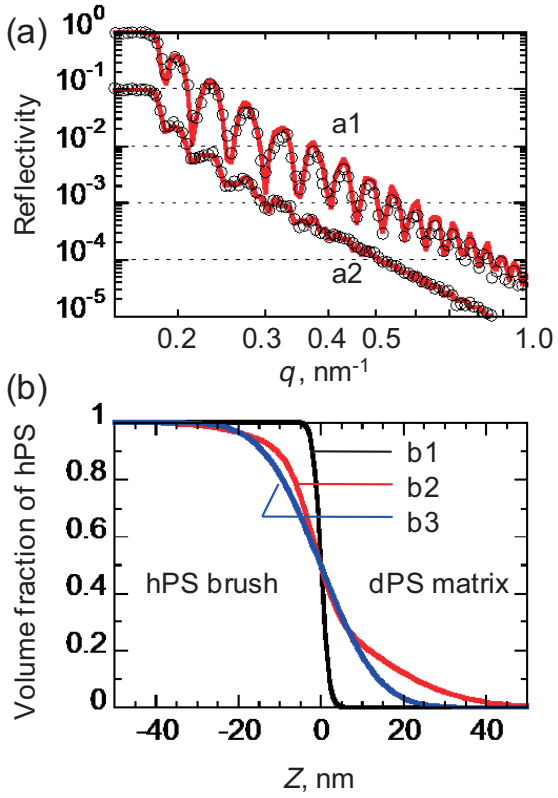

Fig. 8: (a) NR curves (open circles) of hPS brush/dPS bilayer film annealed at 393 K for (a1) 0 min and (a2) 30 min, and the corresponding fit profiles (red line) calculated by (b) volume fraction profiles of hPS as a function of depth z from the center of the interface between hPS brush and dPS layer. The three curves in part (b) represent the volume fraction profiles of (b1) before and after the annealing based on (b2) asymmetric model and (b3) symmetric model (see text for details).

length.

When the intermixing of two free polymers takes place under athermal system, the volume fraction distribution curves at the interface are usually described by symmetric error functions [13] as shown by the blue-colored line (b3) in Fig. 8(b). However, such symmetrical distribution did not give the appropriate fit to the observed NR curve. There still was a slight difference between the reflectivity curve and the simulated fit drawn by blue line in Fig. 9. On the other hand, we proposed an asymmetric distribution model of the volume fraction at the interface, as shown by line b2 in Fig. 8(b), in order to obtain the best-fit curve. The resulting reflectivity curve (red line in Fig. 9) reproduced sufficiently well the NR curve. This asymmetric gradient profile had a long "foot" extending deep into the matrix phase, indicating that the extension of the high molecular weight chains of the hPS brush into the dPS matrix was predominant to the penetration of the free dPS chains into the brush layer.

In conclusion, we demonstrated the intermixing at

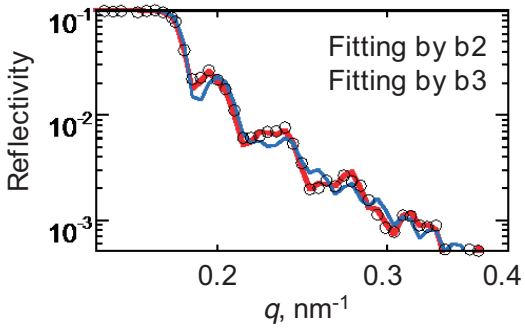

Fig. 9: NR curve (open circles) of hPS brush/ dPS bilayer film annealed at 393 K for 30 min, and the corresponding fits calculated by volume fraction profiles of hPS with asymmetric model (b2), and symmetric model (b3). Both model profiles are shown in Fig. 1(b).

the interface between the hPS brush with a broad MWD and free dPS. Although the combination of brush/free polymer examined here corresponded to the dry-brush case, sufficiently thick interface has been achieved such as the case of wet-brush condition. This large interfacial width of a polydisperse brush may improve the adhesive strength between the brush substrate and polymer matrix.

2.2 Dewetting process of deuterated polystyrene and poly(vinyl methyl ether) blend thin films via phase separation

Dewetting of polymer thin film is a key issue in the instability in many fields, including coatings, adhesives and lubrications. Especially for polymer blend thin films, much attention is also paid to phase separation because of its important role in affectng dewetting. The interplay between phase separation and dewetting has been investigated experimentally and theoretically in recent years, and two possible mechanisms (capillary fluctuations or composition fluctuations) have been proposed [14-17]. However, it is still obscure how fluctuations after phase separation affect dewetting in the in-plane directions as well as the out-of-plane directions. Therefore, for the understanding of dewetting via phase separation, studies on fluctuations in the in-plane as well as the out-of-plane directions are indispensable.

In a previous work [17], we found that composition fluctuations occurred in the depth direction (or in the out-of-plane direction) from the specular NR measurements on the dPS/PVME thin films below 100 nm. However, the composition fluctuations over the in-plane direction were not clarified during the incubation period. To observe the structure and/or composition fluctuations in the in-plane direction, we therefore performed optical microscope (OM), light scattering (LS) and off-specular neutron reflectivity (NR) measurements in deuterated polystyrene (dPS) / poly(vinyl methyl ether)

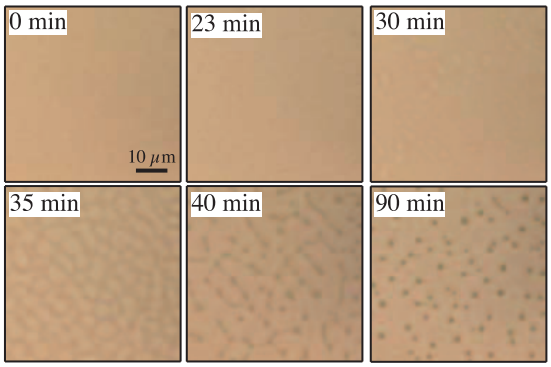

Fig. 10: Time evolution of OM images for 36nm d-PS/h-PVME thin films at 115°C.

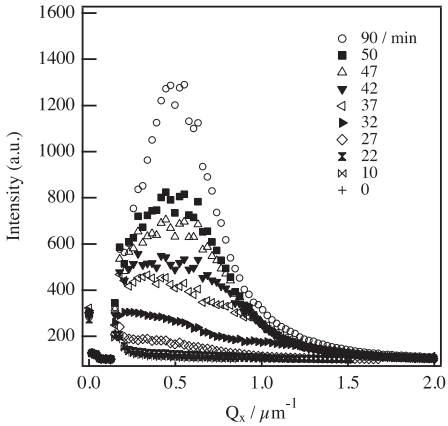

Fig. 11: Time evolution of the LS profiles for the dPS/PVME thin film 36 nm thick after temperature jump to 110°C.

(PVME) on a quartz substrate [18].

The results of the OM measurements to see the time evolution of morphology of the dPS/PVME thin film 36 nm thick in the in-plane direction after the temperature jump into the two-phase region are shown in Figure 10. In the initial stage of annealing no changes were observed in the surface morphology, and then some holes were formed in the surface (in-plane direction) at $\sim$ 27 min after the temperature jump. The result clearly shows that dewetting occurs after a certain incubation time before 27 min.

In the next step, we examined composition fluctuations over the in-plane direction using the LS and off-specular NR measurements. Figure 11 shows the time evolutions of the one dimensional scattering LS profiles, which were obtained by circular averaging of the two-dimensional scattering profiles. The scattering intensity was not observed until 20 min but began to increase slightly at $\sim$20 min in the incubation period. After the incubation period, the scattering intensity increased and the scattering peak appeared at around 40 min. This value corresponds to the correlation between the droplets in the dewetted film. In order to confirm if composition fluctuations occur during the incubation period more rigorously, we also analyzed the

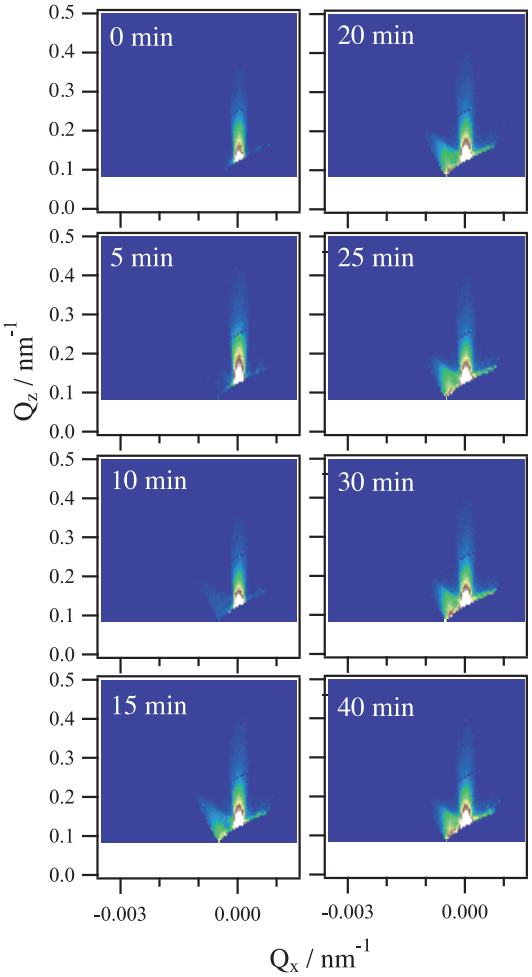

Fig. 12: Time evolution of the 2D reflectivity intensities in the Q_x-Q_z geometries for the dPS/PVME thin film 36 nm thick after temperature jump to 110°C.

off-specular NR data, which revealed a different scattering contrast from LS.

Figure 12 shows the $Q_x - Q_z$ plots of the reflectivity intensities at the various annealing times in the two-phase region. The acquisition time for the one frame was 5 min in the measurement. In the beginning of 5 min, only the specular intensity was observed at $Q_x = 0$. However, the off-specular intensities gradually increased after 10 min even in the incubation period, and the profile is tilted along the Q_x vector. The off-specular peak position $Q_{\mathrm{integ,max}}$ and the peak intensity $I_{\mathrm{integ,max}}$ are plotted in Figure 13 (a) and (b), respectively, to see the time evolution of composition fluctuations in the in-plane direction. It is noted that we calculated the off-specular intensity integrated in the Q_z region from 0.12 to 0.17 nm^{-1} as function of Q_x. The off-specular intensity $I_{\mathrm{integ}}(Q_x)$ reflects composition fluctuations along the surface direction (or the in-plane direction). At 10 min after the temperature jump $I_{\mathrm{integ}}(Q_x)$ began to increase with a clear peak and grew up with the annealing time, suggesting composition fluctuations oc-

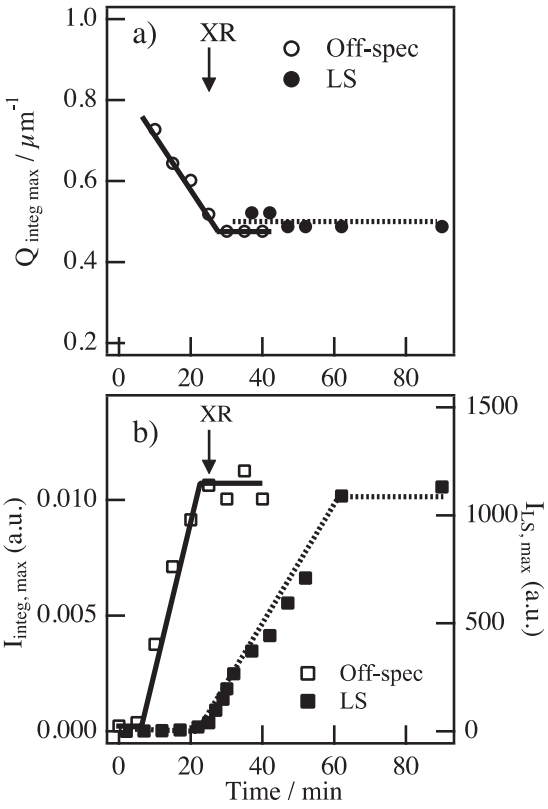

Fig. 13: Time evolution of the peak position $Q_{\text{integ, max}}$ (a) and peak intensity Iinteg, max (b) evaluated from the LS and Off-specular profiles for the dPS/PVME thin film 36 nm thick after temperature jump to 110°C.

curred in the in-plane direction even in the incubation period. During this period, the peak position shifts to the lower Q_x region (Figure 13(a)), suggesting that the in-plane composition fluctuations grow inside the films before dewetting.

Based on the previous work and the measurements of the OM, LS and off-specular NR measurements, the out-of-plane composition fluctuations occur randomly over the in-plane direction in the beginning of the incubation period. Consequently, the in-plane composition fluctuations arise after the out-of-plane fluctuations as seen in the off-specular NR data. These in-plane composition fluctuations gives rise to height fluctuations from the inside of the film, and finally induce dewetting, resulting in the droplets of the dewetted film as shown in Figure 10.

2.3 Spontaneously formed polymer brush at water/ polymer interfaces

Polymer brushes are structures in which polymer chains are grafted on a surface. It is known that polymer brushes show non-adsorption property of protein, because of its steric repulsion. Among them, especially the polymer brushes that consist of polyelectrolytes are called polyelectrolyte brushes. Polyelectrolyte brushes

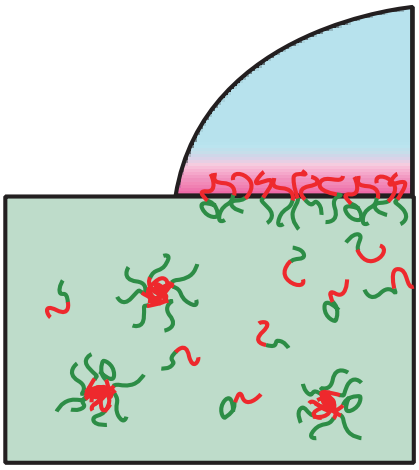

Fig. 14: Spontaneously formed polymer brush fabricated using amphiphilic block copolymers blended in an elastomer matrix.

differ from neutral polymer brushes in that they can change their conformation depending on the environment such as salt concentration or pH. We developed a new fabrication method of polymer brushes using segregation of amphiphilic diblock copolymers, and we succeeded in formation of brush structure which consists of a hydrophilic polymer at elastomer/water interface (Fig. 14). Our previous studies show that the brush density becomes higher when the system gains large mixing enthalpy of hydrophilic polymer and water [19]. We extended the same methodology to amphiphilic diblock copolymers which contain weak polyelectrolyte.

Hydride terminated polydimethylsiloxane (Mw= 62,700), a cross-link agent, Pt-catalyst and poly (dimethylsiloxane-*b*-methacrylic acid) (PDMS-*b*-PMA) (Mn=8,000-3,300, 8,000-7,000) were dissolved in tetrahydrofuran (THF), then this solution was spin-casted on wafers. PDMS was then cross-linked. Those specimens were soaked in (deuterated) water at 50 or 80°C. We have conducted neutron reflectivity studies using SOFIA to reveal the interfacial structures of spontaneously formed weal polyelectrolyte brushes and deuterated water. In Figure 15, examples of reflectivity curves and their scattering length density profiles are shown. Approximately 20 nm thick brush layer was evidently formed at the water and PDMS interface by the segregation process. Therefore, a polyelectrolyte brush can be evidently fabricated using spontaneous segregation of block copolymers. However, the growth of the brush layer as a function of time at 50°C clearly indicates that the segregation process is much slower than the previously reported segregation of poly(dimethyl siloxane-*b*-ethylene oxide) to water/PDMS interface. This slower segregation could be related to the slow diffusion and dissociation of strongly bound micelles with hydrogen bonds between mathacrylic acid. Fur-

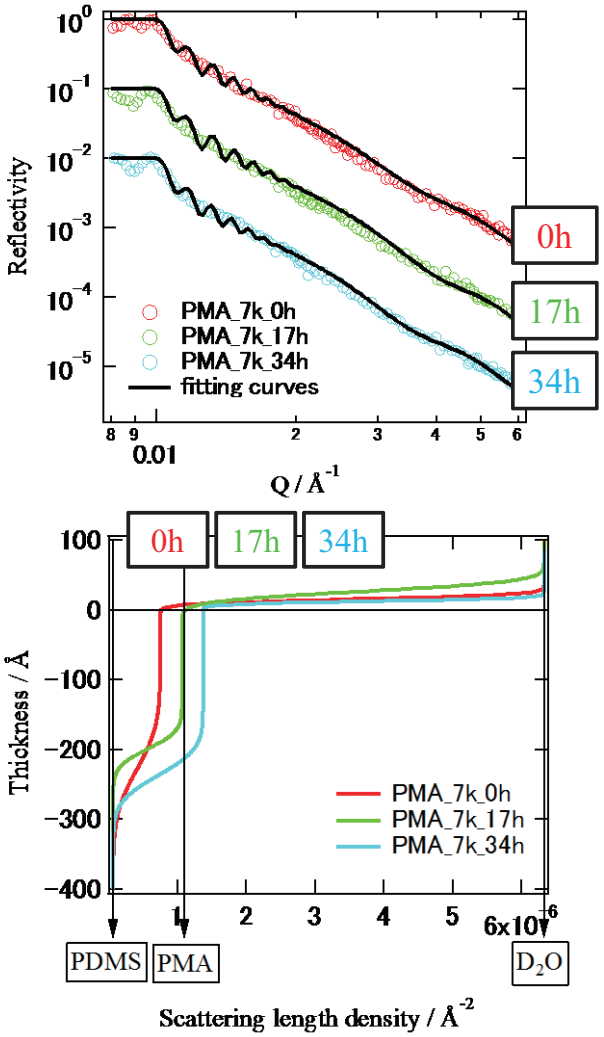

Fig. 15: Time evolution of neutron reflectivity profiles (upper panel) and scattering length density profiles (lower panel) of polymer brushes formed using poly (dimethylsiloxane-*b*-methacrylic acid) (8,000- 7,000) preanneled at 50°C in deuterated water.

ther experiments and analysis are being conducted.

2.4 Surface segregation of poly(2-methoxyethyl acrylate) in a mixture with poly(methyl methacrylate) in water

Poly(2-methoxyethyl acrylate) (PMEA) possesses excellent blood-compatibility, resulting in its practical use as a coating material for artificial organs [20]. Nevertheless, it seems that our present level of understanding of blood-compatibility is far from the goal of a universal and reasonable explanation. We believe that this is simply because the information about the aggregation structure and chain dynamics at the water interface is lacking. Unfortunately, a thin film of PMEA supported on a solid substrate can be easily broken, namely because it is easily dewetted. Previously, we have overcome this difficulty by mixing PMEA with a typical glassy polymer, poly(methyl methacrylate) (PMMA) and annealing at appropriate conditions, resulting in a successful building of a stable and flat surface in thin film, perfectly covered with PMEA [21]. Here, to give a better understanding of the blood-compatibility of PMEA, the aggregation states of the blend film at the interface were characterized by neutron reflectivity (NR).

Table 1: Parameter values used to fit the experimental reflectivity for the PMEA/dPMMA blend films contact with air and D_2O.

Medium	$(b/V)_i/10^{-4}$ nm^{-2}			t/nm	σ_i/nm				ξ/nm
	$(b/V)_1$	$(b/V)_2$	$(b/V)_3$		σ_1	σ_2	σ_3	σ_4	
air	1.10	4.63	1.15	60.0	1.3	3.3	2.9	0.7	-
D_2O	1.71	4.82	1.69	66.6	1.9	3.6	3.2	0.8	2.0

PMEA with a number-average molecular weight (M_n) of 26k and a molecular weight distribution (M_w/M_n) of 3.23, where M_w denotes a weight-average molecular weight, and deuterated PMMA (dPMMA) with M_n of 93k and M_w/M_n of 1.07 were used. Thin blend films with a thickness of approximately 60 nm were prepared onto solid quartz-made blocks by a spin-coating method from a toluene solution with a weight ratio of PMEA/dPMMA (50/50). The obtained films were dried in a vacuum oven at room temperature for 24 h, and then, were annealed for 6 h at 353 K. The temperature level was between the bulk glass transition temperature (T_g) and the phase separation temperature for this blend. The density profile of the blend films along the depth direction was examined by NR measurement with a SOFIA reflectometer at J-PARC. A Teflon®-made reservoir filled with D_2O was mounted onto the film. Prior to the measurement in D_2O, the blend film was aged in D_2O for 24 h, which was sufficient enough to reach a *quasi*-equilibrium state for the film. The reflectivity was calculated on the basis of the scattering length density (b/V) profile along the depth direction. The (b/V) values of PMEA, PMMA, dPMMA, SiO_2, and D_2O used for the calculation were 1.15 $\times$ 10^{-4}, 1.04 $\times$ 10^{-4}, 7.02 $\times$ 10^{-4}, 3.48 $\times$ 10^{-4}, and 6.38 $\times$ 10^{-4} nm^{-2}, respectively.

The open circles of Figure 16(a) show the scattering vector (q_z) dependence of NR for the PMEA/dPMMA blend film contact with air. The blend ratio expressed on the basis of the sample weight was 50/50 (wt/wt). In this case, the blend ratio expressed by sample volume was (48/52, v/v). Panel (b) of Figure 16 shows the model (b/V) profile used to obtain the best-fit reflectivity. The solid curves drawn in panel (a) of Figure 16 represent the best fits to the data obtained in air, calculated on the basis of a layer model illustrated in panel (c) of Figure 16. To simplify the fitting model, the film is divided into three layers (layer 1, 2, and 3) with Gaussian roughness at each interface, σ_i, while t denotes total thickness of the blend film, as drawn in the panel (c) of Figure 16. Table 1 summarizes the fit-

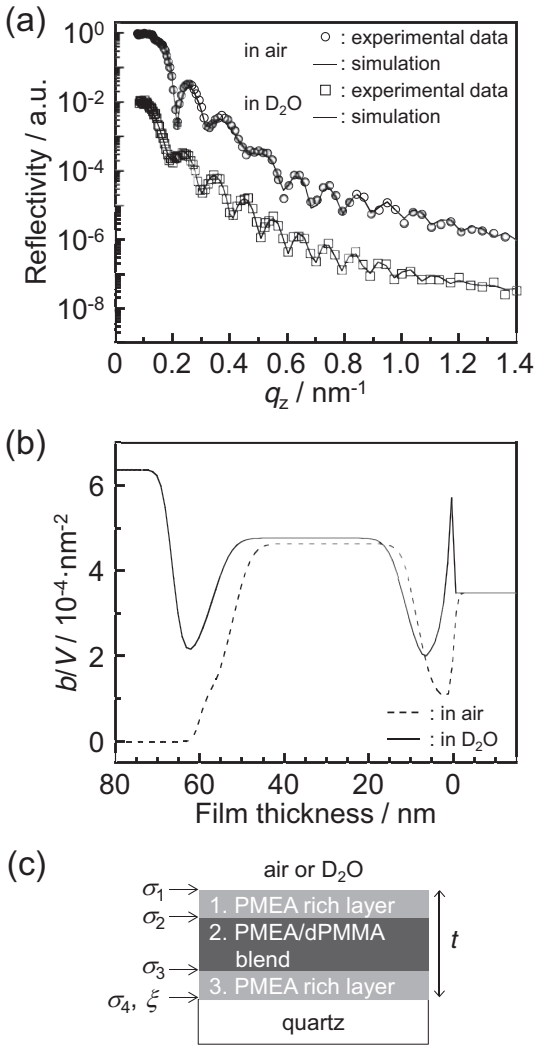

Fig. 16: (a) NR curves for the PMEA/dPMMA blend film contacted with air and D_2O, respectively. Open symbols depict the experimental data, and solid lines denote the reflectivity calculated on the basis of (b) (b/V) profiles of the blend film. For clarity, the reflectivity data in D_2O is off-set by two decades. (c) A schematic illustration of the model used for the fitting.

ting parameters.

Usually, a composition profile of a miscible polymer blend film in the surface region is explained by an exponential decay function. The obtained NR data, however, could not be well fitted with exponential decay function. Thus, the (b/V) profile was expressed by Gaussian function as follows,

$$(b/V)(z)=\sum_{i=1}^{N}\frac{(b/V)_i-(b/V)_{i+1}}{2}\left\{1+\mathrm{erf}\left(\frac{z-z_i}{\sqrt{2}\sigma_i}\right)\right\}$$

where N is the number of layers, $(b/V)_i$ is (b/V) of the ith layer at position (z_i), and erf is error function. Since the calculated NR curves were in good agreement with the experimental results under the restriction that the integrated composition through the film is the same as the blend ratio, the model (b/V) profiles in Figure 16(b) well reflect the real composition along the direction normal to the interface.

Assuming the incompressibility of chains, the average (b/V) value for the PMEA/dPMMA film with the blend ratio of 48/52 (v/v) was 4.20×10^{-4} nm^{-2}. However, the obtained $(b/V)_1$, $(b/V)_2$, and $(b/V)_3$ of the PMEA/dPMMA blend film in air were 1.10×10^{-4}, 4.63×10^{-4} and 1.15×10^{-4} nm^{-2}, respectively. While the $(b/V)_1$ and $(b/V)_3$ values contacting with air and substrate, respectively, were below the calculated (b/V) value, the $(b/V)_2$ for the internal region (layer 2) of the film was greater than that value, indicating that PMEA, the component with the lower (b/V) value, enriched at both of air and substrate interfaces. In our previous study, it was revealed that volume fraction of PMEA component at the air interface region of the blend film was approximately 100% under vacuum by angular dependent X-ray photoelectron spectroscopy [21]. And also, the surface free energy of PMEA was lower than that of PMMA. Considering the lower surface energy as well as the lower degree of polymerization of PMEA compared to those of PMEA, namely, the enthalpic and entropic advantages of PMEA, the surface segregation of PMEA in air is quite reasonable. On the other hand, based on our previous results, the $(b/V)_1$ value should be the same as the (b/V) value of PMEA (1.15×10^{-4} nm^{-2}). However, the obtained $(b/V)_1$ value (1.10×10^{-4} nm^{-2}) was slightly smaller than that value. This can be explained by considering adsorption of H_2O molecules to the film in air. Since PMEA is one of hygroscopic polymers and our NR measurement was carried out in an ambient atmosphere, absorption and diffusion of water molecules in the surface region of the film possibly occurred. If that is the case, the (b/V) value in such the region decreased due to a smaller (b/V) value of water (-0.56×10^{-4} nm^{-2}).

The open squares of Figure 16(a) show the q_z dependence of NR for the PMEA/dPMMA blend film in contact with D_2O. The decay length (ξ) was defined as the distance at which the (b/V) at the substrate interface decreased by a factor of 1/e. The layers 1 and 3 show the PMEA-rich layers which were constructed due to segregation of PMEA component in the blend film discussed below. The fitting parameters are also shown in Table 1. While the $(b/V)_1$ and $(b/V)_3$ values were below the calculated (b/V) value on the basis of the composition, the $(b/V)_2$ value was greater than that value. This can be explained in terms of the segregation of the PMEA component with the low (b/V) value at the D_2O and substrate interfaces. Actually, the interfacial free energy of PMEA in contact with water (8.7 mJ/m^{-2}) was lower than that of PMMA (21.9 mJ/

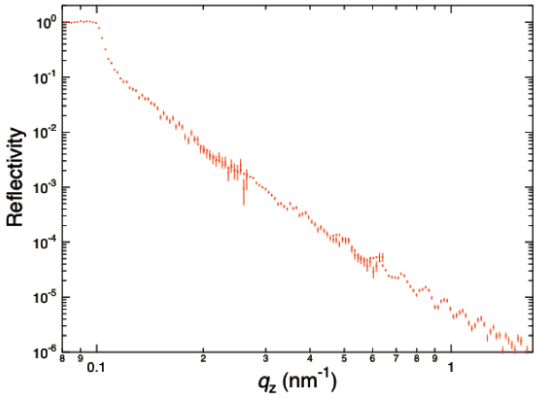

Fig. 17: Specular neutron reflectivity profile as a function of q_z for the spin-coated thin film of h-PS blended with d-PS (M_n=23×10^3), of which average (b/V) was matched with that of a silicon substrate.

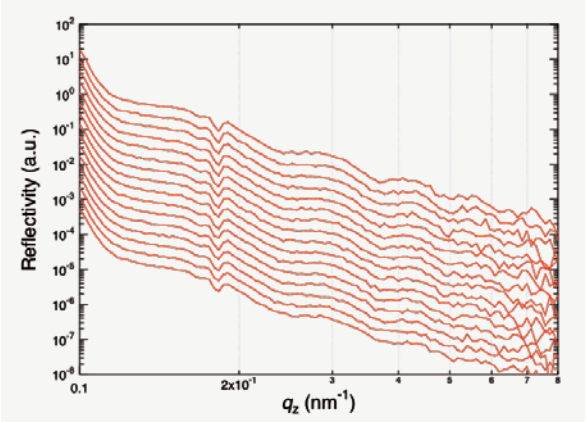

Fig. 18: Time evolution of specular neutron reflectivity profile for the contrast-matched thin film of h-PS blended with d-PS (M_n=60×103) during annealing at 150°C in a vacuum. The profiles are arranged from the top to the bottom with increasing the annealing time.

m^{-2}) evaluated by contact angle measurement using an air bubble. Thus, the segregation of PMEA to the D_2O interface is quite reasonable. On the other hand, all of the $(b/V)_i$ values obtained in D_2O were greater than those corresponding values obtained in air. These results indicate that D_2O molecules with a high (b/V) value penetrated the whole layers of the PMEA/dPMMA blend film. The $\sigma 1$ value at the D_2O interface for the PMEA/dPMMA blend film was greater than that obtained at the air interface. This means that the D_2O interface was more diffuse than the air interface due to partial dissolution of PMEA chains into the D_2O phase. Also, the t value of 60.0 nm for the PMEA/dPMMA blend film in air increased to 66.6 nm in D_2O.

2.5 De-wetting suppression of a polymer thin film by blending a high molecular weight component

Polymers are nowadays utilized as a form of thin film in a variety of practical applications such as coating, paint, adhesion, and so on. The polymer thin films become unstable with decreasing their thickness due to the enhancement of interfacial interaction, and often encounter de-wetting from a substrate. So far, many attempts have been made to stabilize the polymer thin films. One of the ways to prevent de-wetting of a polymer thin film is blending a small amount of a high molecular-weight homologue. In this study, the depth distribution of the component will be investigated for the thin films of polystyrene (PS) binary blends changing molecular weight for one of the components, to understand the mechanism of de-wetting suppression by blending high molecular-weight homologue.

The samples used are a poly(styrene-h_8) (h-PS) with number-averaged molecular weight, M_n, of 10×10^3, and poly(styrene-d_8)s (d-PS) with M_n of 23×10^3 and 60×10^3. The weight fraction of d-PS in the binary h-PS/d-PS blend films was 0.14 to match the average scattering length density, (b/V), of PS blend with that of the silicon substrate. The thin film specimens were prepared by spin-coating 2 wt% solution of PS blend in toluene at 3,500 rpm on silicon substrates. The Si wafers were cleaned by a mixture of concentrated sulfuric acid and 30% hydrogen peroxide in the volume ratio of 7:3. The thickness of the thin films thus prepared was evaluated to be about 35 nm by X-ray reflectivity measurement.

Figure 17 shows specular neutron reflectivity profile for the thin film of h-PS blended with d-PS (M_n=23×10^3), of which average (b/V) matched with that of a silicon substrate. The fringes are still distinguished in the profile, though they are very weak. This could be attributed to the non-uniform distribution of the component produced even in the as-prepared thin film, or the subtle difference between (b/V) calculated from the bulk density and the actual one. Figure 18 exhibits time evolution of specular neutron reflectivity profile for the contrast-matched thin film of h-PS blended with d-PS (M_n=60×10^3) during annealing at 150°C in a vacuum with a high-temperature cell. The data were collected in an event mode using a double-frame of neutrons. The fringes are more clearly observed than the blend thin film with d-PS (M_n=23×10^3), implying that d-PS with a higher molecular weight is less uniformly distributed even in the as-prepared film. Also, the fringes slightly shifted toward high-q_z and decayed with increasing the annealing time. The data analysis is now progressing to obtain time evolution of the component distribution in the thin film.

3. Conclusion

At BL16 in J-PARC/MLF, we constructed a horizontal type neutron reflectometer called SOFIA. Thanks to the high flux beam and instrumental upgrades, the specular reflectivity can be measured down

to 10^{-7} within one hour for a 3-inch substrate at 300 W. Also, time resolved measurement with the slice of one minute using wide wavelength band, and off-specular reflectivity measurement with a position sensitive detector were possible. This year, we started the measurement for free-liquid interfaces thanks to the relaxation of the regulation for liquid treatment. The optical mirror to change the incident angle and Langmuir trough to make a monolayer on the sample surface were successfully installed and the liquid measurement is now open for users.

For the further upgrade, we are developing a new scintillation counter. This new detector is planned to be installed next year. Besides, we are also evaluating a new Li-glass scintillator. Although the scintillator has problems for practical use, its features are quite remarkable: high detection efficiency, high count rate, and low gamma-ray noise. Moreover, we plan to make new sample environments for time-slicing measurements after rising temperature and sample-liquid contact. For this purpose, the environment should be controlled remotely from the outside of the shielding, and the response should be as quick as the time bin of the time-slicing measurement. One of the possible ways to heat a sample quickly is through laser heating, which can rise the temperature up to a few hundred degrees centigrade within ten seconds. For sample-liquid contact measurement, a liquid reservoir with a solenoid valve can realize the remote control.

References

[1] K. Mitamura *et al.*, *J. Phys. Conf. Ser.* **272**, 012017 (2011).
[2] N. L. Yamada *et al.*, *Euro. Phys. J. Plus* **126**, 108 (2011).
[3] K. Mitamura *et al.*, *Polymer J.* **45**, 100 (2013).
[4] A. Yoshikawa *et al.*, *IEEE Transactions on Nuclear Science* **56**, 3796 (2009) .
[5] J. Iwanowska *et al., Nucl. Instr. and Meth. A* **652**, 319 (2011) .
[6] T. Yanagida *et al., Opt. Mater.* **33**, 1243 (2011).
[7] M. Kobayashi and A. Takahara, *Polym. Chem.* **4** (2013) in-press.
[8] S. T. Milner *et al. Macromolecules* **22**, 853 (1989).
[9] L. Leibler and A. Mourran, *Mater. Res. Soc. Bull* **22**, 33 (1997).
[10] P. G. Ferreira *et al. Macromolecules* **31**, 3994 (1998).
[11] H. Arita *et al., Polym. J.* **45**, 117 (2013).
[12] D. Kawaguchi *et al., Macromolecules* **36**, 1235 (2003).
[13] G. Reiter and U. Steiner, *J. Phys. II* **1**, 659 (1991).
[14] Y. Liao *et al., Macromol. Rapid Comm.* **6**, 351 (2006).
[15] H. Wang and R. J. Composto, *Phys. Rev. Lett.* **92**, 185704 (2004).
[16] H. Wang and R. J. Composto, *Europhys. Rev. Lett.* **50**, 622 (2000).
[17] H. Ogawa *et al., Polymer* **49**, 2553 (2008).
[18] H. Ogawa *et al., Macromolecules* accepted.
[19] M. Inutsuka, *et al., Macro Lett.* **2**, 265 (2013).
[20] M. Tanaka *et al., Biomaterials* **21**, 1471 (2000).
[21] K. Tanaka *et al., Phys. Chem. Chem. Phys.* **13**, 4928 (2011).

BL23: Polarisation Analysis Neutron Chopper Spectrometer

K.Ohoyama[a], T.Yokoo[b,c], S.Itoh[b,c], J.Suzuki[b], T.J.Sato[e], K.Iwasa[d], K.Tomiyasu[d], M.Matsuura[a,f], H.Hiraka[a,b], M.Fujita[a], H.Kimura[e], H.Kira[f], Y.Sakaguchi[f], T.Ino[b,c], T.Oku[g], K.Kaneko[g], J.Suzuki[f], H.M.Shimizu[i,b], T. Arima[j], M. Takeda[g], M.Hino[k], and H.Nojiri[a]

[a]*Institute for Materials Research, Tohoku University, Sendai 980-8577, Japan*
[b]*Neutron Science Division, High Energy Accelerator Research Organization, 1-1 Oho, Tsukuba, Ibaraki 305-0801, Japan*
[c]*J-PARC Center, Tokai, 319-1195, Japan*
[d]*Graduate School of Science, Tohoku University, Sendai 980-8578, Japan*
[e]*Institute of Multidisciplinary Research for Advanced Materials, Tohoku University, Sendai, 980-8577, Japan*
[f]*CROSS, Tokai, 319-1106, Japan*
[g]*Japan Atomic Energy Agency, Tokai, Ibaraki 319-1195, Japan*
[h]*Neutron Science Laboratory, The Institute for Solid State Physics, University of Tokyo, Tokai, 319-1195, Japan*
[i]*Graduate School of Science, Nagoya University, Nagoya 464-8602,Japan*
[j]*Department of Advanced Materials Science, Graduate School of Frontier Sciences, University of Tokyo, Kashiwa, 277-8561, Japan*
[k]*KUR, Kyoto University, Kumatori, 590-0494, Japan*

This project is aiming at constructing a neutron polarisation analysis spectrometer based on a collaboration between KEK and Tohoku University. The polarisation analysys technique is quite important, because it makes it possible to investigate complicated spin correlations and spin-lattice couplings in novel magnets, in particular, multipolar orderings, high-T_C superconductivity, multiferroics systems and so on. For instance, clarifying electromagnons in multiferroics, which may be excited by electric field due to coupling between polarisation and magnetosation, is an important scientific theme; how does the neutron scattering see magnons coupled with electric fields (i.e. light)? For such spin-lattice coupling properties, polarisation analysis is the most powerful and direct probe to observe crossover terms of magnetic and lattice response. Though many ingenious spectrometers/ diffractometers in MLF/J-PARC have begun their operations, the full polarisation analysis ability is still not sufficient, particularly, for spectroscopy. The instrument of this project, named POLANO (ポラーノ in Japanese) will be the first full polarisation analysis spectrometer in J-PARC. The proposal for this project was accepted by the final board of J-PAPC Center in September-, 2011; the construction at BL23 has been authorized at last. Most of the activities of this project have been financially supported by funds of KEK, S-type project, the Neutron Scattering Program Advisory Committee (2009S09) since 2009. Fortunately, the POLANO project has been fully founded by a supplementary budget by the government in 2012FY. Accoeding to the budget, the construction will start in 2013 FY and will be completed by the end of 2014FY. The first neutron beam will be accepted by the early 2015FY.

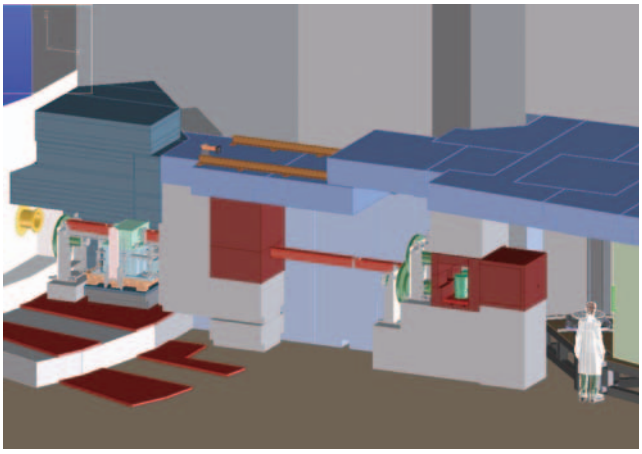

Fig. 1: Image picture of POLANO (BL23).

POLANO is a compact chopper spectrometer with polarisation analysis ability. Fig. 1 is a schematic rendering view of the spectrometer, drawn by Mr. J. Suzuki of KEK through S-type project. The flight pass are L_1=17.5 m, L_2=2.0 m, and L_3=1.85 m, respectively. Since a space for the polarisation devices is needed between the chopper and the sample position, L_3 becomes longer than the conventional chopper spectrometers. The energy resolution of the chopper spectrometer is determined by the following standard equation.

$$\left(\frac{\Delta\epsilon}{E_i}\right)^2 = \left(2\frac{\Delta t_{ch}}{t_{ch}}\right)^2 \left(1+\frac{L_1}{L_2}\left(1-\frac{\epsilon}{E_i}\right)^{\frac{3}{2}}\right)^2 + \left(2\frac{\Delta t_m}{t_{ch}}\right)^2 \left(1+\frac{L_3}{L_2}\left(1-\frac{\epsilon}{E_i}\right)^{\frac{3}{2}}\right)^2 \quad (1)$$

, where t_{ch}, tm and E_i are pulse width at the moderator, and chopper opening time, and incident energy respectively. For the H_2 decoupled moderator in MLF, Δt_m (μsec) is estimated as Δt_m (μsec) =2.5 E(eV)$^{-1/2}$. Since $L_1 \gg L_2$ and $L_3 \sim L_2$, the resolution is almost determined by the first term of the eq.(1), meaning that the resolution is not sensitive to L_3. Fig. 2 shows the effect of L_3 and L_2 to energy resolution under intensity optimised condition: $\Delta t_{ch} = \Delta t_m$. The contour lines and the values indicate the energy resolution, $\Delta\epsilon/E_i$, at ϵ =0 meV. As shown in Fig. 2, the length of L_3 does not seriously affect the energy resolution under the present condition in comparison with the effect of L_2 as expected. Under the present condition, $\Delta\epsilon/E_i \sim 0.04$ at ϵ =0 meV for E_i =100 meV is feasible for L_2 =2.0 m.

Fig. 3 indicates Q resolution defined as $\Delta Q/k_i$ for several scattering angles. $\Delta Q/k_i$ less than 1% is achieved under the present condition, which is satisfactory good to distinguish excitations in main scientific targets, for example, the so-called "hour glass structure" in High -T_C cuprates.

To minimise the background and beam decay by air scattering, a fan shape vacuum chamber, which is the same type as those in BL01, BL12, and BL14 will be installed. However, in the POLONO, only the equatorial plane will be occupied with PSDs (60 cm length, 3/4 inch diameter, and 10 atm) in the first stage, though large solid angle of detectors is of course important for high efficiency experiments. Investigations of spinlattice couplings will be an important target of POLANO, which gives characteristic responses in the high-Q region. Thus, we have decided to give a priority to installing PSDs to wide scattering angle positions up to 135° ; consequently, we should installing PSDs in the equatorial plane preferentially. For a 60 cm PSD with L_2 =2 m, the elevation angle will be ±8.5°. Detector banks for elevation directions will be installed after the completion of the equatorial plane in the second phase.

One of the main scientific targets is magnetic excitations in $\epsilon \geq 100$ meV region. Thus, the ^{3}He spin filter technique is most suitable as a polariser. For developments of ^{3}He spin filters, the strong support of KEK, which has high capabilities for neutron instrumentations and generation of polarised neutrons, is indispensable to achieve this project. A continuous polarising spin exchange optical pumping (SEOP) system will be installed because it can maintain stable polarisation of the incident neutron beam. The SEOP system is being developed under a collaboration among JAEA, KEK and Tohoku Univ. (the Quantum Beam Fundamentals Development Program of MEXT, Japan). On the powder diffractometer HERMES of IMR, Tohoku Univ. [1], we successfully performed polarisation diffraction experiments with a ^{3}He spin filter polarised in the KEK filling station by Dr. Ino. The results indicate that stable and satisfactory high neutron polarisation for

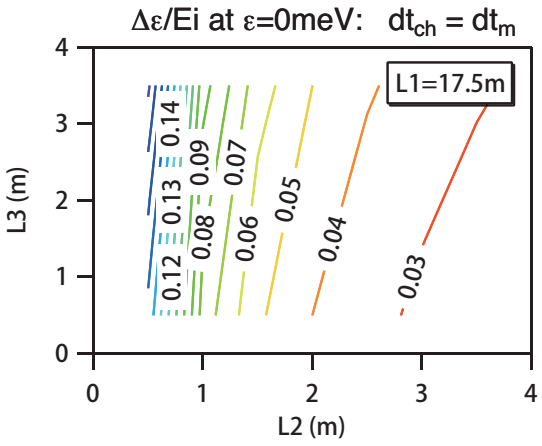

Fig. 2: Effect of L_3 to energy resolution $\Delta\epsilon/E_i$ for E_i=100 meV under the optimised condition ($\Delta t_{ch} = \Delta t_m$).

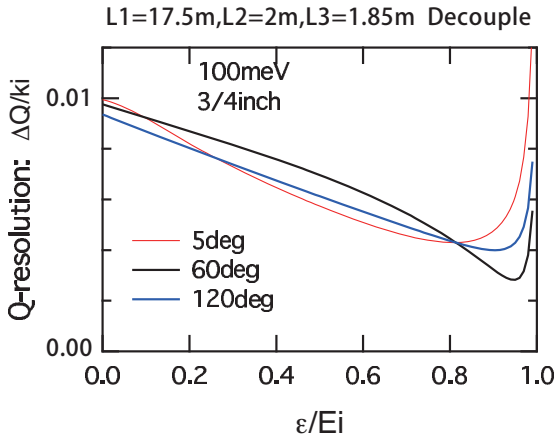

Fig. 3: Q-resolution at ϵ=0 meV for E_i=100 meV at 2θ=5°, 60°, and 120° under the optimised condition.

diffraction experiments can be achieved even by the non-optical pumping mode. The results have been already published elsewhere[2]. Note that under the collaboration, the development of larger GE180 glass cells with a diameter of 10 cm for SEOP systems is in progress in Tohoku Univ.

A focusing suppermirror guide tube system will be installed to POLANO to obtain enough flux at the sample position. To optimise the layout of the suppermirrors, the flux at the sample position under several conditions was estimated by McStas. Fig. 4 shows the final result after the optimised positions of all the sets of guide tubes. The black solid line indicates the flux without guide tubes, the dotted line indicates the flux at the sample position of BL01 provided by Dr. Kajimoto. When the flux is optimised at around 60 meV, the flux at the sample is satisfactory high in a wide energy region below 150 meV; at 100 meV, the unpolarised beam flux is 3.8×10^5 (n/sec/cm^2/meV/1 MW), which is 70% of that of BL01 at 100 meV. When the

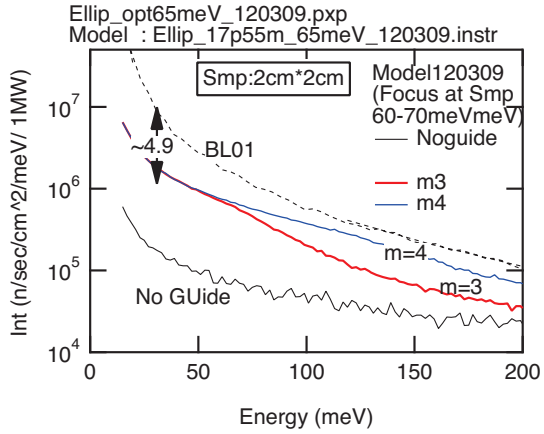

Fig. 4: Energy dependence of white and unpolarised beams at th example position.

conditions of a ^{3}He filter are optimised by Cussens quality factor [3], the neutron transmission of a ^{3}He cell is ~ 0.35, indicating that the flux of the polarised beam by the optimised ^{3}He cell is $\sim 1.3\times10^5$ (n/sec/cm^2/ meV/1MW), which is 1/4 $\sim$ 1/5 of the unpolarised beam of BL01 at 100 meV.

Anlyser devices are of course the key instrument. In the first phase, a fan shape suppermirror bender system will be installed because it is the most practical choice at the moment. Naturally, we will focus on the energy region of $E_i \leq 25$ meV, in which a lot of important scientific targets exist. For an optimization calculation, the gap, d , between neibour suppermirrors, is 1 mm and m-value is expected to be m=4. The distance between the sample position and the entrance of the suppermirror is 450 mm, which is determined from the diameter of a supperconducting magnet of J-PARC. This condition gives a size of a suppermirror piece as 296 mm length and 224 mm height. Important parameters of the suppermirrors are summarized in Table-I. Note that the effective sample diameter is 12.1 mm because of limitation of the acceptable divergency at the suppermirror; only neutrons with divergency smaller than the critical angle can reflect at the mirrors and transmit the analyser device. To cover a scattering range of 20°, the gross area of all the required pieces is 8.0 m^2. Since it is impossible to cover the whole scattering angle of 135° by a fixed fan shape bender suppermirror analyser, a rotation mechanism will be installed in the vacuum chamber to set the analyser at a particular scattering angle.

To create an international collaboration about polarization devices, we are in talks with PSI, which has extensive experience in fan shape suppermiror analysers for HYSPEC in SNS, USA. With the support of the S-type project, Yokoo (KEK) and Ohoyama (IMR) visited PSI in September 2012, and April 2013 to discuss with Dr. Uwe, Dr. Kenzelmann, and Dr. Hautle

Table 1: Required parameters of fan type curved supermirror analysers, based on the estimation by Stewert et al.[4].

	Parameter
m	m=4
Crytical Angle	0.77° (20 meV)
gap of mirrors	1 mm
Curvature radius	11.0 m
Length of a mirror	296 mm
Height	224 mm
Sample Diameter	12.1 mm

Fig. 5: Shiled of BL23, acceptance inspection at Yotsuba Kiko on March-2013.

the establishing of collaboration about the suppermirror analyser, and the Dynamic Nuclear Polarisation (DNP) filter as a future polariser. It should be emphasized that universities which have no international collaborations with neutron facilities in the world can find an opportunity for collaborations through the S-type project based on the activities of KEK, which is a center of worldwide collaborations in quantum beam science. The collaboration with PSI for the POLANO project is also based on a cooperation agreement between KEK and PSI. The authors believe this is one of the important roles of KEK's S-type project.

In 2012FY, the project progressed with the finical support of the S-type project. In particular, main parts of the radiation shields have been already constructed. Fig. 6 shows prepared shields for POLANO, which was constructed by Fuji Service Ltd. Full of Shields will be completed in 2013 FY, and will be installed in the au-

Fig. 6: Kickoff Meeting on 25-April-2013 at KEK, Tokai Campus.

tumn of 2013 to BL23. Suppermirror guide tubes were also prepared by the support of S-type project, which will be installed in the shutter and biological shielding of BL23. As an ambitious challenge, we are developing a correlation chopper [5] in the S-type project under a collaboration with Metal Technology Co. Ltd. Another important activity of the S-type project is the development of DNP in KEK. DNP devices are suitable for high energy polariser; since the project aims at polarisation analysis in the over 100 meV region, high energy polarisers are indispensable for the final stage. Moreover, an important advantage of DNP is that DNP can be used near supperconducting magnets. In 2012FY, some microwave instruments have been prepared to polarise targets of DNP.

To start the construction, the kickoff meeting was held on April 25th ,2013, at KEK 1st Building, Tokai with the support of the S-type project. Members of the POLANO project and many key persons in J-PARC attended the meeting, and discussed to create joint recognition of the project and their respective roles.

The nickname "POLANO" is short for POLarisation Analysis Neutron chopper spectrOmeter, but it originally came from the title of a fairy story "Polano squire" written by Kenji Miyazawa, who was a famous fairy story writer born in Tohoku district in 1896. Since Miyazawa and his works are a symbol of the mentality of Tohoku district, we believe POLANO is a suitable name for this project.

References

[1] K. Ohoyama *et al.*, Jpn. J. Appl. Phys. 37 (1998) 3319.
[2] K. Ohoyama, *et al.*, NIMA 860 (2012) 75.
[3] L.D Cussena, *et al.*, NIMA 440 (2000) 409.
[4] Stewert *et al.*, J. Appl. Cryst. 42 (2009) 69.
[5] S. Rosenkranz and R. Osborn, J. Phys. 71 (2008) 705.

S-010: Development of an Advanced Special Neutron Powder Diffractometer under Extreme Environment for Materials (III)

T.Fukunaga[1], K.Mori[1], Y.Onodera[1]
T.Kamiyama[2], M.Yonemura[2], M.Nagao[2], Y.Ishikawa[2], S.Torii[2], R.Tomiyasu[2],
H.Asano[2], T.Sakuma[3], T.Ishigaki[4], A.Hoshikawa[4], K.Aizawa[5], S.Harjo[5],
K.Kino[6], Y.Idemoto[7], N.Kitamura[7], H.Arai[8], and Y.Uchimoto[9]

[1]1Research Reactor Institute, Kyoto University, Kumatori, Sennan-gun, Osaka 590-0494, Japan
[2]Institute of Materials Structure Science, High Energy Accelerator Research Organization, Tsukuba, Ibaraki 301-8501, Japan
[3]College of Science, Ibaragi University, Mito, Ibaragi 310-8512, Japan
[4]Frontier Research Center for Applied Atomic Sciences, Ibaragi University, Mito, Ibaragi 310-8512, Japan
[5]J-PARC Center, Japan Atomic Energy Agency, Tokai-mura, Naka-gun, Ibaraki 319-1195, Japan
[6]Graduate School of Engineering, Hokkaido University, Sapporo, Hokkaido, 060-8628, Japan
[7]Faculty of Science & Technology, Tokyo University of Science, Noda, Chiba, 278-8510, Japan
[8]RISING Battery Project, Kyoto University Office of Society-Academia Collaboration for Innovation, Uji, Kyoto, 611-0011, Japan
[9]Graduate School of Human and Environmental Studies, Kyoto University, Yoshida, Kyoto, 606-8501, Japan

The progress of technological innovation in rechargeable batteries is attracting much attention for its potential to overcome the issues of greenhouse gas emissions and to solve the limitation of fossil energy resources. Despite the impressive growth of the utilization of nickel-metal hydride and lithium ion batteries, the advancement and innovation in the technology as well as the scientific understanding underling the battery technology is too slow.

When a lithium ion battery starts to supply electric power to a system, the lithium-ions transfer between the positive and negative electrodes. The structural change of the two electrodes after the transformation of the lithium ions through the interfaces between each electrode and the electrolyte solution is very important not only from a scientific viewpoint but also from a technological one. The information about the structural changes of the two electrodes and the location of the lithium ions will provide guidelines for improvement of the present lithium ion battery and invention of an out-of-the-box battery.

In order to clarify the structure of the positive and negative electrodes and the interface between the electrode and electrolyte solution at an atomic level, a new neutron powder diffractometer, SPICA, has been designed and constructed as one of the state-of-the-art measurement apparatuses. It is well known that the neutron is a more powerful investigation tool to get information about the location and movement of light elements like hydrogen and lithium atoms than the X-ray. Therefore, the advantages of the neutron diffraction would allow to acquire more knowledge of the location and movement of the lithium ions or the change of the atomic configuration in the positive and negative electrodes and the electrolyte solution.

The SPICA diffractometer is installed at the BL09 beam line with the decoupled-poisoned moderator and the flight path from the moderator to the sample position is L_1=52 m to achieve high resolution. The sceneries of the assembling work of the main units of the SPICA diffractometer and the installation operation of the T0 chopper are shown in photo 1(a), (b) and (c), (d), respectively.

Moreover, photo 2(a) and (b) show the fabricated

(a) (b)

(c) (d)

Photo. 1: The construction of the SPICA diffractometer (a),(b) and the installation of the T0 chopper (c),(d).

(a) (b)

Photo. 2: The SPICA diffractometer viewed from the side (a) and above (b).

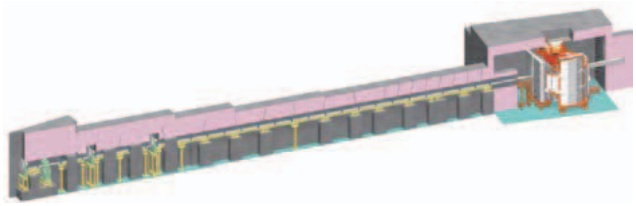

Fig. 1: Total image of the SPICA diffractometer

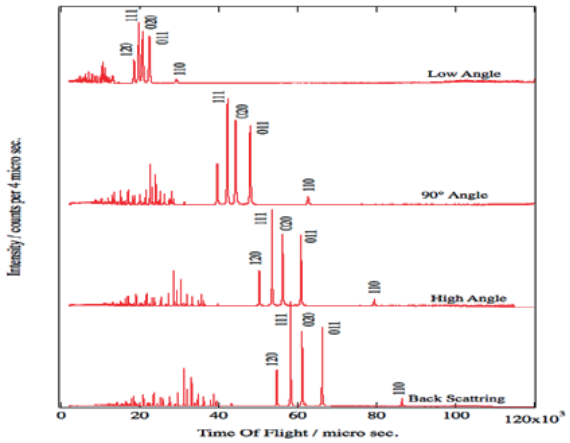

Fig. 2: Diffraction profiles of the diamond powder at the low angle, 90° angle, high angle and back scattering.

the SPICA diffractometer viewed from the side and above, respectively. A high-performance focusing system with elliptic supermirrors was adopted to suppress the diffusion of neutrons and to keep high neutron intensity at the sample position. Figure 1 indicates a full picture of the SPICA diffractometer with the elliptic supermirror guide line, the T0 chopper and three disk choppers.

As shown in Fig. 2, the diffraction of diamond powder was measured in order to check up the counter systems (low angle, 90° angle, high angle and back scattering) and their performance. All diffraction profiles indicate good signal-to-noise ratio, that is, low background. The best resolution was recognized to be less than 0.09% as shown in Fig. 3. The good performance, low background and high resolution, of the SPICA diffractometer will allow us to analyze the detailed structure of the battery element materials and their change during the discharge and charge cycle in an in-situ measurement.

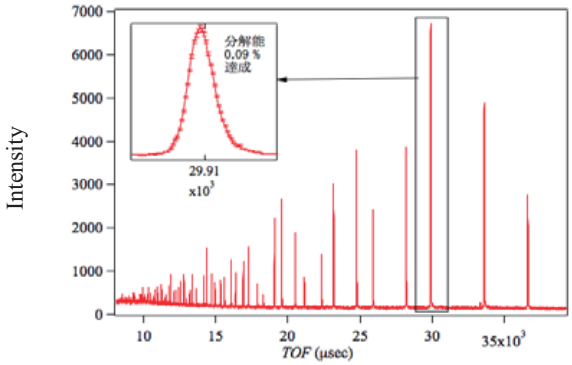

Fig. 3: Best resolution less than 0.09% can be achieved in the back scattering of the SPICA diffractometer.

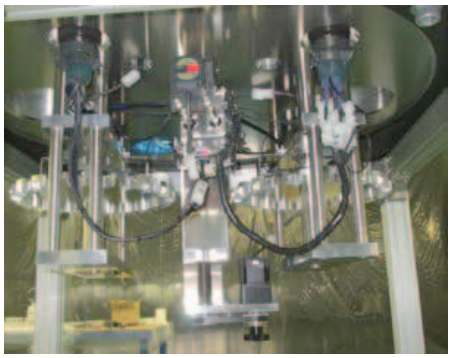

Photo. 3: The automatic sample changer for the ex-situ measurement.

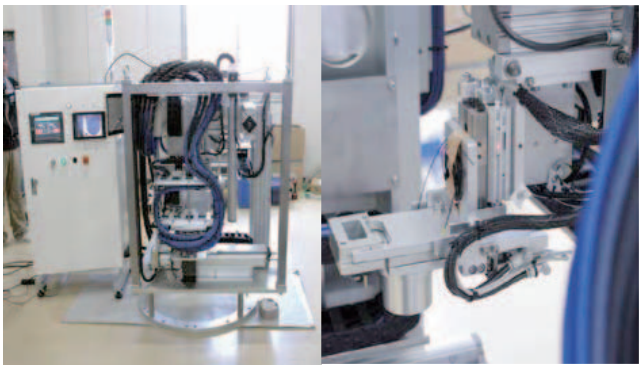

(a) (b)

Photo. 4: The automatic sample changer for the in-situ measurement. ((a): total image, (b): sample delivery system)

Various kinds of apparatuses have been establishing for ex-situ and in-situ measurements of battery element materials under a wide variety of special environments. Photo 3 shows the automatic sample changer that can load 40 samples. Using the equipment, 40 samples can be measured in ex-situ condition automatically and in continuity.

Photo 4 shows the automatic sample changer, which can load 10 samples with different discharge and charge conditions, for the in-situ measurement. This is the ever-more-sophisticated equipment, which will allow us to easily carry out the in-situ experiment using not only a commercial-release LIB cell but also an out-of-the-box battery cell during discharge and charge cycle.

The commissioning of the SPICA diffractometer is continuing. Simultaneously, various kinds of test measurements using conventional samples have been carried out by the NEDO project researchers.

Acknowledgement

We would like to acknowledge Mr. Koji Muroya and Mr. Seiji Sugai for their technical support in constructing the SPICA diffractometer. This work was supported mainly by the RISING project, the Research and Development Initiative for Scientific Innovation of New Generation Batteries, of NEDO, the New Energy and Industrial Technology Development Organization.

Neutron Transmission Imaging

Y.Kiyanagi, T.Kamiyama, H.Sato, T.Sato, T.Sakurai, S.Muto*, S.Satoh*, J.Haba*, H.M.Shimizu**, K.Hirota**, Y.Yamagata***, T.Tanimori****, T.Nagae****, S.Tasaki*****, and K.Iwase******

Hokkaido University
Kita 13, Nishi 8, Kita-ku, Sapporo, Hokkaido, 060-8628, Japan
**High Energy Accelerator Research Organization (KEK), 1-1 Oho, Tsukuba, Ibaraki, 305-0801, Japan*
***Nagoya University, Fro-cho, Chikusa-ku, Nagoya, 464-8601, Japan*
****RIKEN 2-1 Hirosawa, Wako, Saitama 351-0198, Japan*
*****Graduate School of Science, Kyoto University Oiwake-cho, Kita Shirakawa, Sakyo-ku, Kyoto, 606-8502, Japan*
******Graduate School of Engineering, Kyoto University Yoshida Honmachi, Sakyo-ku, Kyoto, 606-8501, Japan*
*******Ibaraki University 4-12-1Narusawa-cho, Hitachi, Ibaraki, 316-8511, Japan*

1. Introduction

Neutron transmission imaging has been recognized to be useful not only just for taking transmission imaging but also for material analysis using pulsed neutron transmission. Now, a diffractometer with imaging function, IMAT, is under construction at the ISIS 2nd target station, and an imaging instrument called ODIN has been approved as one of the day-one instruments at ESS. At the J-PARC neutron source in Japan an imaging beam line is now being constructed as the first pulsed neutron imaging instrument among the spallation neutron sources in the world. Furthermore, the PLANET instrument has been equipped with a transmission imaging function and the SPICA will also equip the transmission detector.

The pulsed neutron transmission provides data for spectroscopic analysis since it can render images depending on the time-of-flight or the wavelength. We are developing the transmission imaging using large pulsed neutron sources as well as small accelerator based sources. For this purpose we are working on the detector developments and the accelerator based small neutron sources. Furthermore, test experiments at the existing facilities have been performed.

An experiment of resonance neutron absorption to measure the element distribution of a new decoupler material for the moderator container of the J-PARC was performed and the low content of indium distribution was clearly observed[1]. Furthermore, a region of martensitic phase of a quenched iron rod is clearly observed through the Bragg edge analysis[1]. For these measurements we used the MCP detector developed at UC Berkley[2]. The detector showed its usefulness when dealing with the high spatial resolution for pulsed neutron imaging. Therefore, we have been developing a MCP detector[1, 3] and also μPIC type[4] since it has relatively good spatial resolution. Furthermore, we have studied a high counting rate type detector, namely, a pixel type detector[5], and check the performance of a newly developed electronics.

The pulsed neutron imaging is at a development stage. We have improved the Bragg edge analysis code RITS to analyze the martensitic phase. Furthermore, as one of the new applications for hydrogen dynamics study, while researching its feasibility, we obtained the cold neutron transmission cross sections of the hydrogen storage materials in order to study the difference in hydrogen dynamics in the material.

Compact accelerator-driven neutron sources have been recognized to be useful to support the activity at the high power neutron sources and also to expand the opportunities for the users since they are easy to access and operate. The neutron moderator systems have been studied to establish the optimal design[1, 3]. New neutron sources are now operating at Kyoto University and RIKEN. There was significant progress in the work on this S-type project, which has been aimed at designing compact accelerator-driven neutron sources and also at commissioning of those neutron sources. Here, we reported new results on the development of the MCP, the μPIC and the pixel type detector[5], as well as on the progress of the pulsed neutron imaging and the activities of the new compact neutron sources.

2. Detector development

The detector is one of the most important devices for pulsed neutron imaging. High counting rate is required to measure the spontaneous high intensity neutron flux, and high spatial resolution and relatively large active area are also necessary. The MCP detector developed at UC Berkley is one of the most useful detectors[2], since it has very high spatial resolution, about 55 μm. However, this detector cannot accept full neutrons emitted from the J-PARC and the active area is limited to only about 25 mm. Its high spatial resolution is a very attractive feature, so we have continued

our own MCP detector[3]. μPIC is one of the promising detectors with relatively high spatial resolution of 100-200 μm[4]. However, the maximum counting rate is not so high. Therefore, we need to improve the data transfer performance to get higher counting rate. The spatial resolution of the pixel type detector is not good, only about 2-3 mm, but its counting rate is very high. So, this type of detector is very useful for conducting measurements at J-PARC. At present we do not have detectors which satisfy all our requirements regarding the spatial resolution, the counting rate and the spatial resolution. Therefore, we have to develop various kinds of detectors to apply each one of them to the suitable measurements.

2.1 The MCP detector

In the previous measurement we successfully obtained pulse-by-pulse neutron images. We performed a test experiment on the revised MCP detector using the pulsed neutron source at Hokkaido University. In this new detector we added standard MCP to obtain high and uniform gain and replaced the phosphor (P43) screen with P46 since the decay of P43 is not fast enough for the time-of-flight (tof) measurement. Fig. 1 shows the MCP detector set for the test experiment at the Hokkaido University neutron source (HUNS). We used a high speed camera to record the tof data. Fig. 2 shows the distributions of luminescent spots at different tof, and Fig. 3 shows the tof spectrum obtained by this data. The spectrum clearly showed its characteristic feature. Therefore, the system of the MCP detector coupled with a high speed camera worked well. However, we discovered occasional timing mismatch. For the future work we will re-adjust the system and perform an experiment to check the efficiency and the spatial resolution.

2.2 The μPIC detector

We aimed to compactify and speed up the μ-PIC neutron TOF imager. For that purpose, we introduced a compact electronic circuit, which was originally developed for Phase-2 of the 'Sub-MeV gamma-ray Imaging Loaded-on-balloon Experiment' project. In this system 12 LSI amp-tips for 128ch signal processing and a FPGA for data analysis have been combined on one board. Only 4 boards and a VME memory are necessary to operate the 10 cm square neutron μ-PIC. As shown in Fig. 4, the size has become very compact compared with the present one. Furthermore, we tested the data processing speed as shown in Fig. 5. The speed is 3 or 4 times faster than the present one. So far, the data taking speed has been about 200kcps due to the data transfer speed of 1 MB. Therefore, 70% of the measurement time was devoted to data transfer. By using this new system we can get more than 50Mwords/s of the data transfer rate and a neutron counting rate approaching to 1Mcps is achieved. This

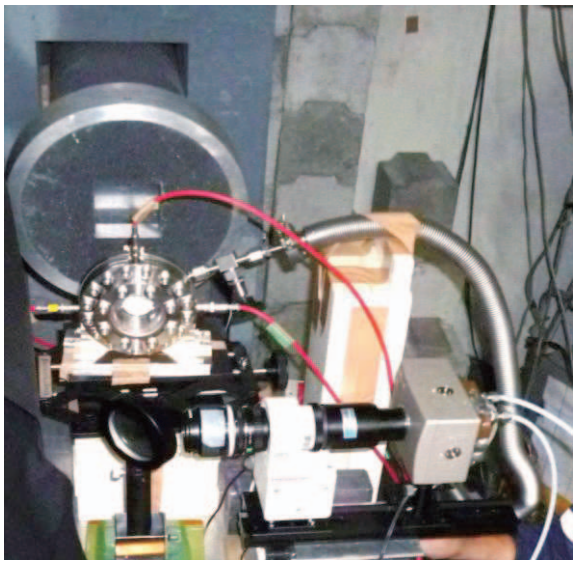

Fig. 1: Experimental setup of the MCP detector system.

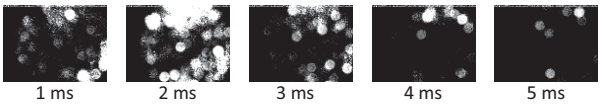

Fig. 2: Distributions of luminescent spots at different time of flight.

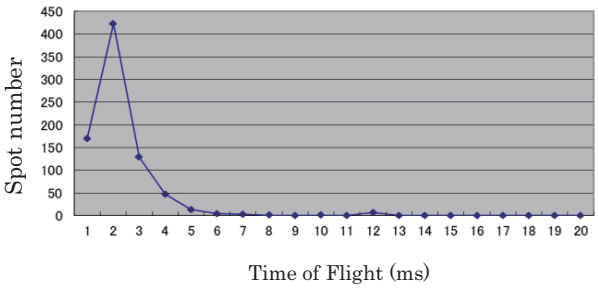

Fig. 3: Time of flight spectrum.

improved the performance by nearly four times. Spatial resolution of less than 100 μm has been also realized (see the lower figure of Fig. 5).

Furthermore, the clock frequency of the FPGA data transfer was increased to 100 MHz, and the data transfer software was improved. We performed a test experiment of the high speed data transfer by using X-ray tube and μPIC for X-ray. The result indicated about twice higher rate as shown in Fig. 6, and suggested 2Mcps counting rate of the neutrons. A test experiment using a real neutron source such as J-PARC is required to check the performance. However, the time of the data transfer from VME to a CPU occupies almost 50% of the measuring time due to the low speed of the bus of the VME. Therefore, we will build a system that transfers the data directly to the CPU through the GIGA Ethernet using the TCP-IP from the board without passing through the VME. It is

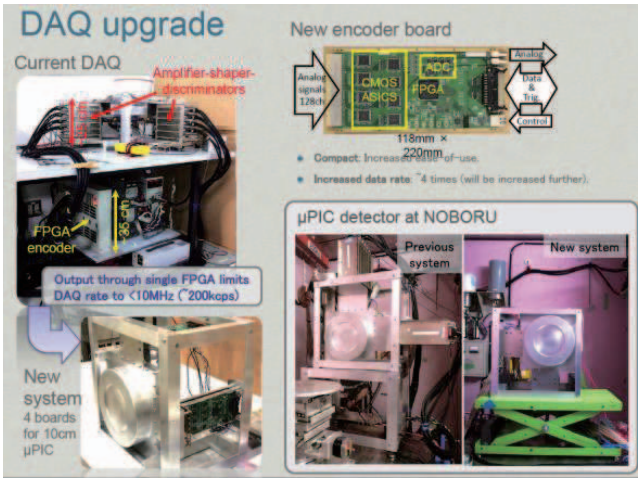

Fig. 4: New system. All electric circuits shown in the upper right photo were assembled on four boards shown in the upper left photo. Previous and new detector systems are shown in the lower right photo.

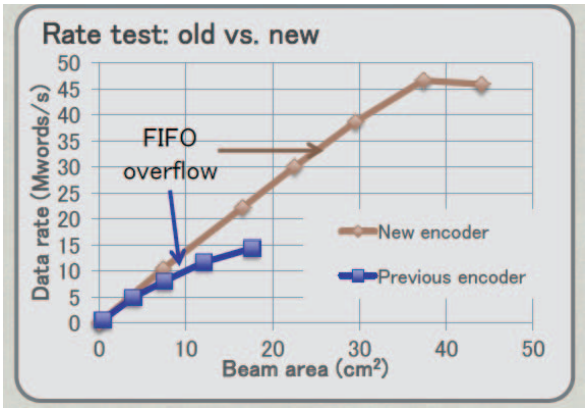

Spatial resolution (µm) at gain of ~275	Previous	New
Gamma cuts	121 ± 1	127 ± 2
Z-consistency	116 ± 1	119 ± 2
TOT shape cut	102 ± 1	96 ± 3

Preliminary!

Fig. 5: Data transfer rate comparison between the previous and the new systems, and preliminary spatial resolutions of the new system using various processing methods.

expected to continuously record the neutron event in a rate of more than Mcps, and it will be useful for the measurement in regions of less than 1 msec TOF in which the material identification using the resonance absorption.

2.3 Pixel type detector

The advantage of the pixel type detector is its high

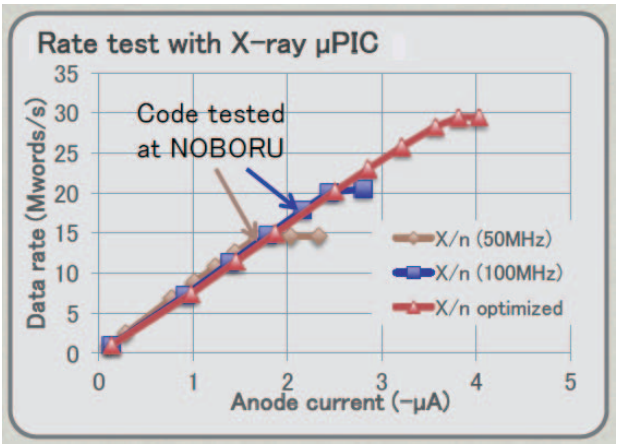

Fig. 6: Data transfer rate after the improvement of FPGA.

counting rate. To improve this performance, we have developed a new electronic device, the LiTA12 detector system. The structure of the system is shown in Fig. 7. The pixel type detector consists of 16×16 Li glass scintillators with an area size of 2.1 mm^2 and 1 mm thickness set in an interval of 3.04 mm. The experiment was performed at BL16 at J-PARC/MLF. First, we checked the counting rate. We used a collimator to adjust the neutron beam intensity. Fig. 8 shows the time of flight data (upper) and the 16×16 image (lower) at 16 mm×32 mm slit size and 16 mm×32 mm slit size. The data at the larger area gave lower counting rate of about 3.7Mcps than the smaller slit size data of 6.4Mcps. This is due to the counting loss at the high counting area of the tof spectra where the tof spectra showed sudden decrease of the counts. This data indicates that the system can work well at least up to 6.4Mcps per detector. We also studied the effect of the gap using a 2 mm^2 neutron beam and it indicated effect of about 0.5 mm gap. Finally, the detector efficiency was studied by comparing with ^{3}He detector with a pressure of about 6 atm. This showed the efficiency to be about 43%, which corresponds to the effective area of this detector, about 48%. Therefore, at ^{6}Li-glass area the efficiency is the same as the ^{3}He detector. Fig. 9 shows a transmission image of a character 'K', in which 'K' is clearly indicated.

3. Progress in the pulsed neutron imaging

3.1 Matensitic phase imaging

We measured a quenched iron rod, indicating the quenched area clearly through pulsed neutron imaging[1), 6)]. However, we recognized that the procedure used for analysis was not appropriate since in the analysis we obtained simultaneously parameters on neutron pulse function data and the lattice spacing. The pulse function is common between ferritic phase and martensitic phase, but the present procedure has been expected to produce larger lattice spacing. Fig. 10 shows

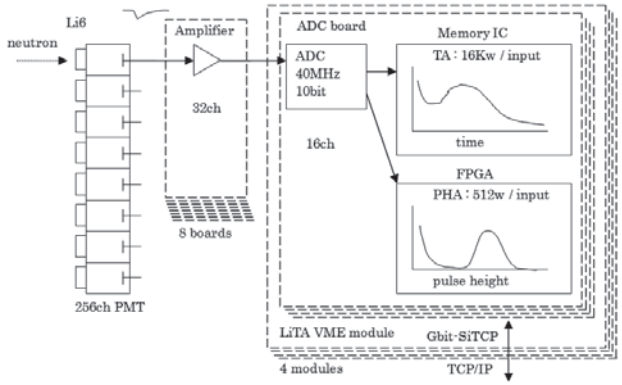

Fig. 7: Structure of the LiTA12 detector system.

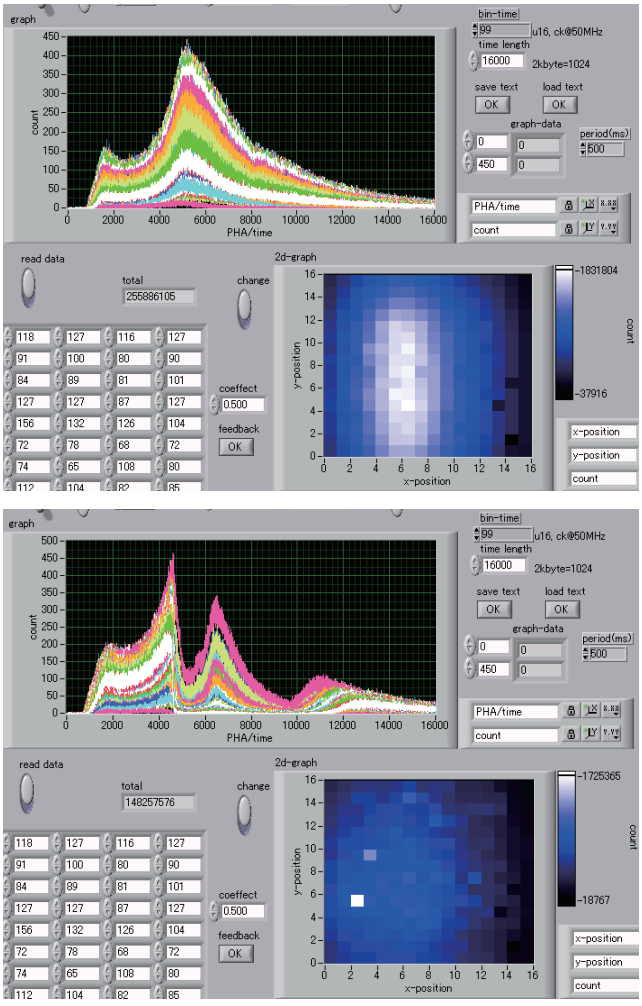

Fig. 8: Time of flight spectra at 16 mm × 32 mm (upper) and 32 mm × 32 mm (lower) slit sizes.

Bragg edges at the ferritic phase (around the center of the rod) and the martensitic phase (quenched area). It is recognized that the slope of the edge became gentle in the martensitic area. This implies that the lattice spacing has distribution, so it is necessary to take into

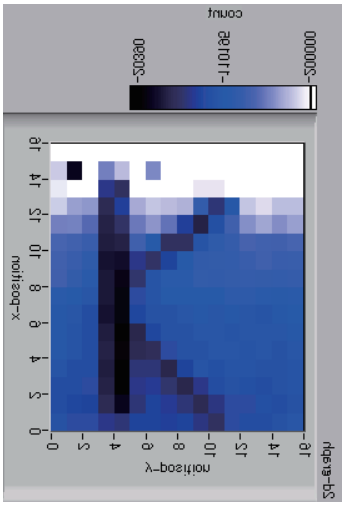

Fig. 9: Example of transmission image of the character 'K'.

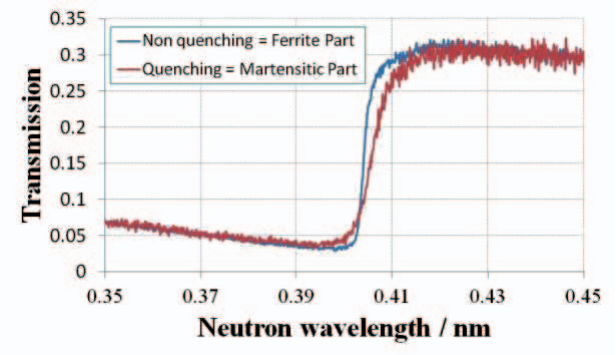

Fig. 10: Bragg edges at ferrite part and martensite part.

account that distribution. Therefore, we introduced the next procedure, namely, first to obtain the pulse function data in the ferritic area, and next by using this pulse data to obtain distribution information of the lattice spacing. Fig. 11 shows the mapping of the dispersion of the lattice spacing distribution. It is clearly recognized that the area of the quenched region overlaps the area with the larger dispersion. The value of the lattice spacing in the quenched region obtained

3.2 Hydrogen dynamics imaging

One of the important characteristics of the neutron is its high sensitivity to hydrogen. The distribution of hydrogenous material has been imaged in the traditional imaging of the neutrons. In the pulsed neutron imaging we use the special feature of the neutron cross section. The hydrogen cross section does not change significantly depending on the neutron wavelength. However, the gradient of the cross section at the long wavelength region is dependent on the freedom of the hydrogen motion. For example, the gradient of the ice cross section is gentler than that of the water[7), 8)]. In the case of metal hydride, sometimes a wavy structure appears and each peak corresponds to the vibration

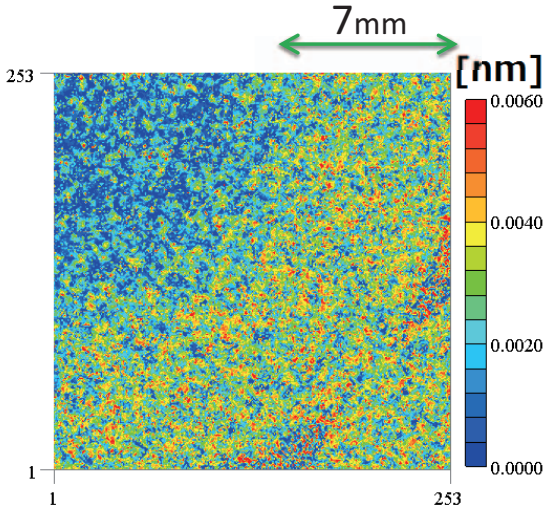

Fig. 11: Dispersion of the lattice spacing.

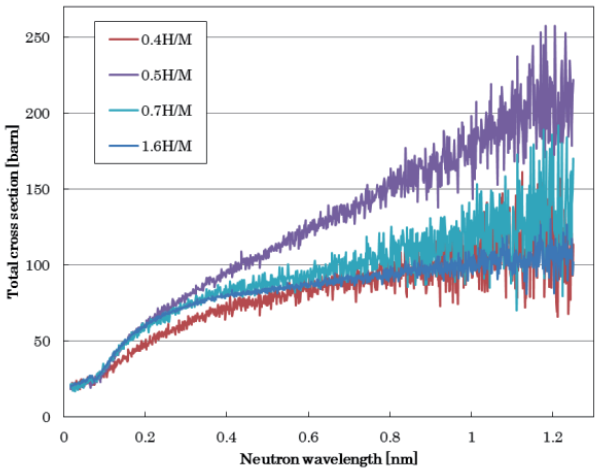

Fig. 12: Transmission cross sections of hydrogen storage material at various hydrogen concentrations.

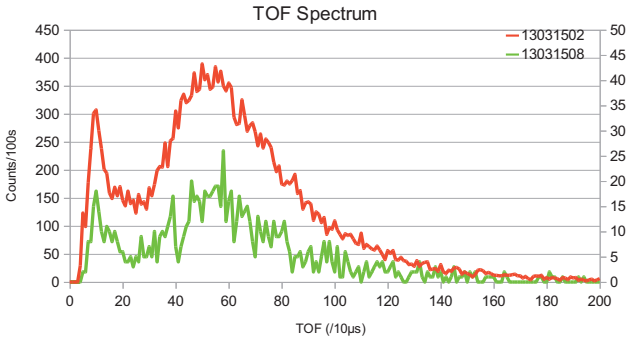

Fig. 13: Typical TOF spectrum of KUANS.

mode of the hydrogen atoms. Those are characteristics applicable to the pulsed neutron imaging.

To study the performance of a hydrogen storage material it will be important to clarify the position dependence of the hydrogen status in the material. As a beginning of this study, we measured the total cross section of the hydrogen at various hydrogen contents. The sample used was $Ti_{0.45}Cr_{0.25}Mo_{0.30}$ and the hydrogen contents were 0.4, 0.5, 0.7 and 1.6 H/Metal atom. The experiments were performed at HUNS. Fig. 12 shows the obtained transmission cross section at each hydrogen-content. This result indicates that the gradient of the cross section depends on the hydrogen content, which suggests a difference in the dynamics of the hydrogen. The steepest gradient appeared at the 0.5 content, not at the highest content. This implies that the hydrogen occupied all allowable sites of the crystal structure and the movement was restricted. The results indicated that this method could be used to study the hydrogen storage status over a wide area of the system depending on the position.

4. Compact Accelerator driven neutron source project

To construct compact accelerator-driven neutron sources a collaboration network called JCANS (Japan Compact Accelerator-driven Neutron Source) has been organized under this S-type project. This network supported the design study of the target-moderator-reflector systems of RANS (RIKEN Accelerator-driven Neutron Source) and KUANS (Kyoto University Accelerator-driven Neutron Source), and their test experiments. Here, we introduce the present status of these two neutron sources.

4.1 Preliminary neutron experiments using KUANS

KUANS (Kyoto University Accelerator-driven Neutron Source) is a proton accelerator based neutron source, in which neutrons are generated by the nuclear reaction of 3.5 MeV-protons with a Be thin film. The generated neutrons are moderated with a polyethylene block and thermalized neutrons are emitted to the experimental area. Since the proton beam is pulsed, the emitted neutrons are also pulsed and the Time of Flight method is used to analyze the neutrons. Fig. 13 shows the typical TOF spectrum measured with Li-scintillator detector at the 1.24 m-position from the moderator. The two spectra in the figure correspond to the incident proton current of 55 μA (13031502) and 18 μA (13031508), respectively. The thermalized neutrons form a clear peak at around 500 ms. Since the neutron intensity at this position is 3490 n/cm^2 s, the neutron flux at the surface of the moderator is estimated to be 5.4×10^5 n/cm^2 s.

Fig. 14 shows the test sample (a handy torch with an electric generator and a Cd-plate) for the neutron radiography (NRG) test experiment. The RPMT-Li scintillator system is used in the experiment and measuring time is about 700 sec. The results are shown in Fig. 15, where four images refer to different wavelength ranges (A:less than 0.063 nm, B:0.063∼0.157 nm,

Fig. 14: Sample for NRG experiment.

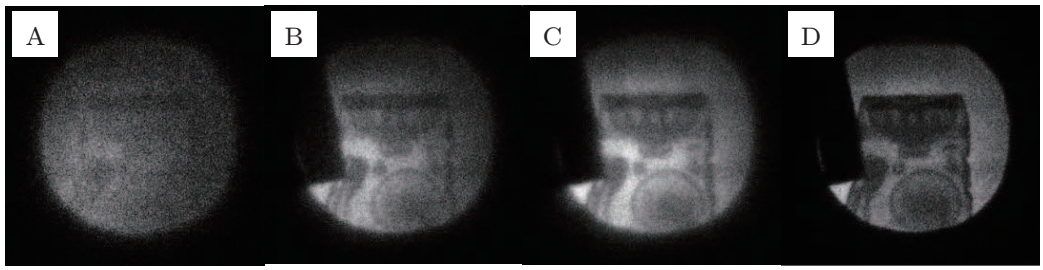

Fig. 15: Results of TOF-NRG at KUANS.

C:0.157∼0.313 nm, and D:0.313∼6.26 nm, respectively). Since absorption cross section of Cd decreases rapidly as the wavelength of neutron decreases, there appears a little image of Cd-plate in A. The contrast of the image becomes higher as A→B→C→D, because cross sections increase with the neutron wavelength.

It is evident that a small neutron source such as KUANS could be used for some research in the neutron field.

4.2 Operation of RANS

RANS consists of a 7 MeV, 0.1 mA average proton beam accelerator with beryllium target, polyethylene thermal neutron moderator, beam lines and detector system. Figure 16 shows the photograph of RANS. The proton accelerator is located at the right-hand side and the target-moderator box at right-middle. The neutron beam is coming from right to left in this picture. The estimated neutron yields are 10^{12} n/sec at RANS. This year we will install the polyethylene block for the thermal neutron moderator and the extracted thermal neutron beam.

Fig. 17 shows the neutron TOF spectrum at RANS. RPMT, the 2D neutron detector, is set at about 4 m downstream from the moderator. The thermal neutron peak is shown around 1.5 m sec.

Fig. 18 shows the neutron radiography image at RANS. The ^{6}LiF/ZnS(Ag) of 0.4 mm thickness neutron convertor and cooled CCD system is used for this measurement. The average proton beam

current is 5 μA and the exposure time is 5 min. This image has acceptable quality for our industrial applications.

Fig. 16: Photograph of RANS.

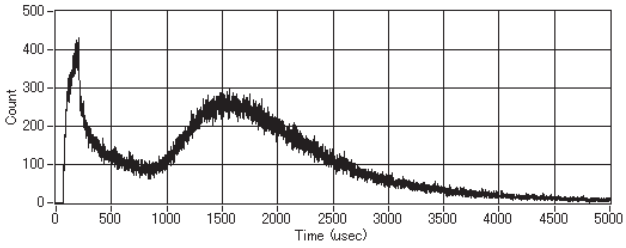

Fg. 17: Neutron time of spectrum at RANS.

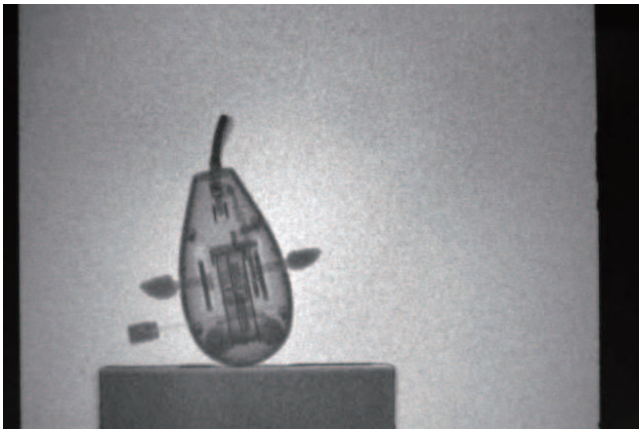

Fig. 18: Radiography image of a bath toy.

5. Summary

For neutron imaging, especially for the pulsed neutron imaging, the detector development is one of the key issues. We have been working on developing various detectors since there is no existing detector that fulfils all requirements. Improvement has been observed in the detector development under the collaboration among laboratories and universities. We presented two new applications, and further approach to looking for new applications is required to expand the field in which the imaging technique is useful. Two neutron

sources have come into operation. This is a great advance in the neutron society. The work done in collaboration and based on JCANS has been very useful for this progress. The effective use of J-PARC and the accelerator based compact sources are very important to promote the industrial application and the test experiments for the future development.

Reference

[1] Y. Kiyanagi, *et al.*, p.55, KENS Report XVII (2011).
[2] A. S. Tremsin, W. B. Feller, R. G. Downing, Nucl. Instr. Meth. A 539/1-2, p.278 (2005).
[3] H. Hasemi, et. al., p.50, KENS Report XVIII (2012).
[4] Toru Tanimori, Hidetoshi Kubo, Kentaro Miuchi, Tsutomu Nagayoshi, Yoko Okada, Reiko Orito, Atsushi Takada and Atsushi Takeda:Time projection chamber based on micropattern detector for neutron, Nucl. Instr. Meth. A 529, 236 (2004).
[5] K. Mizukami, S. Sato, H. Sagehashi, S. Ohnuma, M. Ooi, H. Iwasa, F. Hiraga, T. Kamiyama and Y. Kiyanagi, Nucl. Instr. Meth. A 529, 310 (2004).
[6] Y Kiyanagi, H Sato, T Kamiyama and T Shinohara, Journal of Physics, Conference Series 340, 012010 (2012).
[7] K. Heinloth, *Zeitschrift fuer Physik* **163**, 218 (1961).
[8] K. N. Zaitsev *et al.*, *Soviet Journal of Atomic Energy*, **70**, 238 (1991).

KENS REPORT XIX 2012

PUBLICATION LIST

List of Publications

A compact SEOP ^{3}He neutron spin filter with AFP NMR
T. Ino, Y. Arimoto, H. M. Shimizu, Y. Sakaguchi, K. Sakai, H. Kira, T. Shinohara, T. Oku, J. Suzuki, K. Kakurai, and L.-J. Chang
Journal of Physics: Conference Series **340** (2012) 012006.

A highly stable DC power supply for precision magnetic field measurements and other purposes
T. Ino
Review of Scientific Instruments **83** (2012) 045101.

Aggregation of 1-dodecyl-3-methylimidazolium nitrate in water and benzene studied by SANS and ^{1}H NMR
T. Takamuku, T. Shimomura, K. Sadakane, M. Koga, and H. Seto
Physical Chemistry Chemical Physics **14** (2012) 11070-11080.

Anomalous Spin Diffusion on Two-Dimensional Percolating Network in Dilute Antiferromagnet $Rb_2Mn_{0.6}Mg_{0.4}F_4$
S. Itoh and M. A. Adams
Journal of the Physical Society of Japan **81** (2012) 074704.

Application of matrix decomposition algorithms for singular matrices to the Pawley method in Z-Rietveld
R. Oishi, M. Yonemura, and T. Morishima
Journal of Applied Crystallography **45** (2012) 299-308.

Demonstration of focusing by a neutron accelerator
Y. Arimoto, P. Gertenbort, S. Imajo, Y. Iwashita, M. Kitaguchi, Y. Seki, H. M. Shimizu, and T. Yoshioka
Physical Review A **86** (2012) 023843.

Demonstration of optical thickness measurement using multilayer cold neutron interferometer
Y. Seki, J. Uda, H. Funahashi, M. Kitaguchi, M. Hino, Y. Otake, K. Taketani, and H. M. Shimizu
Journal of Physics: Conference Series **340** (2012) 012039.

Development of a non-adiabatic two-coil spin flipper for a polarised thermal neutron diffractometer with a ^{3}He spin filter
K. Ohoyama, K. Tsutsumi, T. Ino, H. Hiraka, Y. Yamaguchi, H. Kira, T. Oku, Y. Sakaguchi, Y. Arimoto, W. Zhang, H. Kimura, K. Iwasa, M. Takeda, J. Suzuki, K. Yamada, and K. Kakurai
Nuclear Instruments and Methods in Physics Research A **680** (2012) 75-81.

Development of advanced materials for spallation neutron sources and radiation damage simulation based on multi-scale models
M. Kawai, H. Kurishita, H. Kokawa, S. Watanabe, N. Sakaguchi, K. Kikuchi, S. Saito, T. Yoshiie, H. Iwase, T. Ito, S. Hashimoto, Y. Kaneko, M. Futakawa, S. Ishino and J. G. Team
Journal of Nuclear Materials **431** (2012) 16-25.

Development of Longitudinal-Gradient Magnet for Time Focusing of Ultra-Cold Neutron With Anisotropic Inter-Pole
Y. Arimoto, Y. Iwashita, T. Yoshioka, M. Kitaguchi, S. Imajo, H. M. Shimizu, K. Asahi, T. Ino, Y. Kamiya, K. Mishima, S. Muto, K. Sakai, T. Shima, K. Taketani, S. Yamashita, and A. Yoshimi
IEEE Transactions on Applied Superconductivity **22** (2012) 4500704.

Development of polarized Xe gas target for neutron experiment at J-PARC
K. Sakai, T. Oku, T. Shinohara, H. Kira, M. Ooi, F. Maekawa, K. Kakurai, T. Ino, Y. Arimoto, H. M. Shimizu, Y. Sakaguchi, J. Suzuki, K. Ohoyama, and L. J. Chang
Journal of Physics: Conference Series **340** (2012) 012037.

Development of simple neutron counters
S. Satoh and K. Hirota
Proc. Radiation Detectors and Their Uses (2012) 109-116.

Development of Two-Dimensional Scintillation Detectors for Neutron Spin Echo Spectrometers in J-PARC/MLF
T. Nakamura, M. Katagiri, T. Hosoya, K. Toh, M. Kitaguchi, M. Hino, T. Ebisawa, K. Sakasai, and K. Soyama
IEEE Nuclear Science Symposium and Medical Imaging Conference Record (2012) 222-225.

Direct synthesis of oxygen-deficient Li_2MnO_{3-x} for high capacity lithium battery electrodes
K. Kubota, T. Kaneko, M. Hirayama, M. Yonemura, Y. Imanari, K. Nakane, and R. Kanno
Journal of Power Sources **216** (2012) 249-255.

Effect of non-Newtonian gravity on the amplitude of neutron reflection from bulk materials
K. Taketani
Journal of Physics: Conference Series **340** (2012) 012050.

Electronic excitations around the substituted atom in $La_2Cu_{1-y}Ni_yO_4$ as seen via resonant inelastic x-ray scattering
K. Ishii, K. Tsutsui, K. Ikeuchi, I. Jarrige, J. Mizuki, H. Hiraka, K. Yamada, T. Tohyama, S. Maekawa, Y. Endoh, H. Ishii, and Y. Q. Cai
Physical Review B **85** (2012) 104509.

Fermi chopper developed at KEK
S. Itoh, K. Ueno, and T. Yokoo
Nuclear Instruments and Methods in Physics Research A **661** (2012) 58-63.

Formation of a Multiscale Aggregate Structure through Spontaneous Blebbing of an Interface
Y. Sumino, H. Kitahata, Y. Shinohara, N. L. Yamada, and H. Seto
Langmuir **28** (2012) 3378-3384.

Formation of NaCl-Type Monodeuteride LaD by the Disproportionation Reaction of LaD_2
A. Machida, M. Honda, T. Hattori, A. Sano-Furukawa, T. Watanuki, Y. Katayama, K. Aoki, K. Komatsu, H. Arima, H. Ohshita, K. Ikeda, K. Suzuya, T. Otomo, M. Tsubota, K. Doi, T. Ichikawa, Y. Kojima, and D. Y. Kim
Physical Review Letters **108** (2012) 205501.

Gelation effect on the synthesis of high-aspect-ratio gold nanorods
Y. Takenaka, H. Kitahata, N. L. Yamada, H. Seto, and M. Hara
Journal of Nanoscience and Nanotechnology **12** (2012) 714-718.

High-Temperature-Operating Dielectrics of Perovskite Oxides
Y. Ohshima, Y. Noguchi, T. Oguchi, Y. Kitanaka, M. Miyayama, S. Torii, and T. Kamiyama
ECS Transactions **45** (2012) 195-207.

Hydrogen bonding of water in 3-methylpyridine studied by O 1s X-ray emission and absorption spectroscopy
H. Arai, Y. Horikawa, K. Sadakane, T. Tokushima, Y. Harada, Y. Senba, H. Ohashi, Y. Takata, and S. Shin
Physical Chemistry Chemical Physics **14** (2012) 1576-1580.

Kinetic Process of Formation and Reconstruction of Small Unilamellar Vesicles Consisting of Long- and Short-Chain Lipids
N. L. Yamada
Langmuir **28** (2012) 17381-17388.

Large area window on vacuum chamber surface for neutron scattering instruments
S. Itoh, T. Yokoo, K. Ueno, J. Suzuki, T. Teraoku, and M. Tsuchiya
Nuclear Instruments and Methods in Physics Research A **670** (2012) 1-5.

Layered Hydride CaNiGeH with a ZrCuSiAs-type Structure: Crystal Structure, Chemical Bonding, and Magnetism Induced by Mn Doping
X. Liu, S. Matsuishi, S. Fujitsu, T. Ishigaki, T. Kamiyama, and H. Hosono
Journal of the American Chemical Society **134** (2012) 11687-11694.

Magnetic Dipole Moment of the Doubly-Closed-Shell Plus One Proton Nucleus ^{49}Sc
T. Ohtsubo, N. J. Stone, J . R. Stone, I. S. Towner, C. R. Bingham, C. Gaulard, U. Koster, S. Muto, J. Nikolov, K. Nishimura, G. S. Simpson, G. Soti, M. Veskovic, W. B. Walters, and F. Wauters
Physical Review Letters **109** (2012) 032504.

Magnetic excitations in MnP
S. Yano, J. Akimitsu, S. Itoh, T. Yokoo, S. Satoh, D. Kawana, and Y. Endo
Journal of Physics: Conference Series **391** (2012) 012113.

Magnetic excitations in possible spin-Peierls system TiOBr
T. Yokoo, S. Itoh, F. Trouw, A. Llobet-Megias, and J. Akimitsu
Journal of Physics: Conference Series **400** (2012) 032123.

Modified cross-correlation for efficient white-beam inelastic neutron scattering spectroscopy
K. Tomiyasu, M. Matsuura, H. Kimura, K. Iwasa, K. Ohoyama, T. Yokoo, S. Itoh, E. Kudoh, T. Sato and M. Fujita
Nuclear Instruments and Methods in Physics Research A **677** (2012) 89-93.

Neutron scattering studies of Ti-Cr-V bcc alloy with the residual hydrogen and deuterium
K. Mori, K. Iwase, M. Sugiyama, M. Kofu, O. Yamamuro, Y. Onodera, T. Otomo, and T. Fukunaga
Journal of Physics: Conference Series **340** (2012) 012103.

Ni-substitution effects on the spin dynamics and superconductivity in $La_{1.85}Sr_{0.15}CuO_4$
M. Matsuura, M. Fujita, H. Hiraka, M. Kofu, H. Kimura, S. Wakimoto, T. G. Perring, C. D. Frost, and K. Yamada
Physical Review B **86** (2012) 134529.

Present status of neutron fundamental physics at J-PARC
Y. Arimoto, H. Funahashi, N. Higashi, M. Hino, K. Hirota, S. Imajo, T. Ino, Y. Iwashita, R. Katayama, M. Kitaguchi, K. Mishima, S. Muto, H. Oide, H. Otono, Y. Seki, T. Shima, H. M. Shimizu, K. Taketani, T. Yamada, S. Yamashita, and T. Yoshioka
Progress of Theoretical and Experimental Physics (2012) 02B007(1-11).

Quantum Renormalization Effect in One-Dimensional Heisenberg Antiferromagnets
S. Itoh, T. Yokoo, S. Yano, D. Kawana, H. Tanaka, and Y. Endo
Journal of the Physical Society of Japan **81** (2012) 084706.

Rapid Bravais-lattice determination algorithm for lattice parameters containing large observation errors
R. Oishi
Acta Crystallographica Section A **68** (2012) 525-535.

Reverse Monte Carlo modeling of Li_2S-P_2S_5 superionic conductors
Y. Onodera, K. Mori, T. Otomo, A. C. Hannon, M. Sugiyama, and T. Fukunaga
Journal of Physics: Conference Series **340** (2012) 012058.

Stability of neutron beam monitor for High Intensity Total Diffractometer at J-PARC
H. Ohshita, T. Otomo, S. Uno, K. Ikeda, T. Uchida, N. Kaneko, T. Koike, M. Shoji, K. Suzuya, T. Seya, and M. Tsubota
Nuclear Instruments and Methods in Physics Research A **672** (2012) 75-81.

Structural and Magnetic Phase Determination of $(1-x)BiFeO_{3-x}BaTiO_3$ Solid Solution
R. Kiyanagi, T. Yamazaki, Y. Sakamoto, H. Kimura, Y. Noda, K. Ohyama, S. Torii, M. Yonemura, J. Zhang, and T. Kamiyama
Journal of the Physical Society of Japan **81** (2012) 024603.

Structural Evidence for High Ionic Conductivity of $Li_7P_3S_{11}$ Metastable Crystal
Y. Onodera, K. Mori, T. Otomo, M. Sugiyama, and T. Fukunaga
Journal of the Physical Society of Japan **81** (2012) 044802.

Structure Determination of Hydrogen-bonding Network of Water in Hydrophobic Nanospace by Neutron and X-ray Diffractions
T. Iiyama, F. Fujisaki, R. Futamura, A. Hamasaki, S. Ozeki, A. Hoshikawa, and T. Ishigaki
Chemistry Letters **41** (2012) 1267-1269.

Study on Ce:LiCAF scintillator for ^{3}He alternative detector
T. Fujiwara, H. Takahashi, T. Yanagida, K. Kamada, K. Fukuda, N. Kawaguchi, N. L. Yamada, M. Furusaka, K. Watanabe, Y. Fujimoto, and M. Uesaka
Neutron News **23** (2012) 31-34.

Surface Correlation in A Nano-confined DNA Film
N. Biswas, S. Chakraborty, A. Datta, M. Sarkar, M. K. Mukhopadhyay, M. K. Bera, and H. Seto
AIP Conference Proceedings **1447** (2012) 189-190.

Synthesis, crystal structure, and electrode characteristics of $LiMnPO_4(OH)$ cathode for lithium batteries
Y. Yang, M. Hirayama, M. Yonemura, and R. Kanno
Journal of Solid State Chemistry **187** (2012) 124-129.

T0 chopper developed at KEK
S. Itoh, K. Ueno, R. Ohkubo, H. Sagehashi, Y. Funahashi, and T. Yokoo
Nuclear Instruments and Methods in Physics Research A **661** (2012) 86-92.

The Effect of Tetraphenylphosphonium Chloride on Phase Behavior and Nanoscale Structures in a Mixture of D_2O and 3-Methylpyridine
K. Sadakane, Y. Horikawa, M. Nagao, and H. Seto
Chemistry Letters **41** (2012) 1075-1077.

Two-Dimensional Antiferromagnetic Fractons in $Rb_2Mn_{0.598}Mg_{0.402}F_4$
S. Itoh, T. Nakayama, and M. A. Adams
Journal of Physics: Conference Series **400** (2012) 032030.

Variable Permanent Magnet Multipoles
Y. Iwashita, M. Yamada, S. Ushijima, Y. Fuwa, Y. Nasu, H. Tongu, M. Masuzawa, and H. M. Shimizu
IEEE Transactions on Applied Superconductivity **22** (2012) 4000905.

Zwitterionic lipid (DPPC)-protein (BSA) complexes at the air-water interface
S. Kundu, H. Matsuoka, and H. Seto
Colloids and Surfaces B **93** (2012) 215-218.

Structural Analysis of Hydrogen Storage Materials by High Intensity Neutron Total Diffractometer NOVA (高強度中性子全散乱装置NOVAによる水素貯蔵材料の構造解析)
K. Ikeda, T. Otomo, K. Suzuya, M. Misawa, H. Ohshita, M. Tsubota, N. Kaneko, T. Seya, T. Fukunaga, K. Itoh, Y. Kameda, T. Yamaguchi, K. Yoshida, K. Maruyama, S. Shamoto, K. Kodama, Y. Kawakita, and F. Fujisaki
Journal of the Hydrogen Energy Systems Society of Japan (水素エネルギーシステム) **37** (2012) 328-335.

The Materials and Life Science Experimental Facility of J-PARC (J-PARCの物質・生命科学実験施設)
K. Ikeda, T. Oku, J. Suzuki, M. Takeda, A. Hoshikawa, and Y. Miyake
Engineering Materials (Kogyo Zairyo) **60** (2012) 28-31.

Development of a High-efficient Inelastic Neutron Scattering Method with Multiple Incident Energies on a Chopper Spectrometer (受賞記事：チョッパー分光器における複数入射エネルギー同時測定法による高効率非弾性中性子散乱測定法の開発)
R. Kajimoto, M. Nakamura, Y. Inamura, T. Nakatani, W. Kambara, T. Yokoo, and F. Mizuno
日本中性子科学会誌　波紋 **22** (2012) 145-150.

Neutron diffractometer in J-PARC (J-PARCの中性子散乱測定装置)
Y. Kameda
The Japan Association of Solution Chemistry News Letter (溶液化学研究会ニュース) **65** (2012)

KENS REPORT XVIII
Edited by T. Otomo

KENS REPORT XIX
High Energy Accelerator Research Organization